https://ntrs.nasa.gov/search.jsp?R=19820019434 2020-03-21T07:19:16+00:00Z

N82-27310

NASA CR-165553
R81AEG288

165553

National Aeronautics and
Space Administration

CORE COMPRESSOR EXIT STAGE STUDY

VI - Final Report

by

D.C. Wisler

GENERAL ELECTRIC COMPANY

December 1981

Prepared for

National Aeronautics and Space Administration

Contract No. NAS3-20070

NASA-Lewis Research Center

1. Report No.	2. Government Accession No.	3. Recipient's Catalog No.
NASA CR-165553		

4. Title and Subtitle	5. Report Date
Core Compressor Exit Stage Study Volume VI - Final Report	December 1981
	6. Performing Organization Code
7. Author(s)	8. Performing Organization Report No.
D.C. Wisler	R81AEG288
	10. Work Unit No.
9. Performing Organization Name and Address	
General Electric Company Aircraft Engine Business Group Cincinnati, Ohio 45215	11. Contract or Grant No. NAS3-20070
	13. Type of Report and Period Covered
12. Sponsoring Agency Name and Address	Final Report, October 1976 - December 1981
National Aeronautics and Space Administration Washington, D.C. 20546	14. Sponsoring Agency Code

15. Supplementary Notes

Project Manager, Dr. Wojciech Rostafinski, Fluid Mechanics and Acoustics Division, NASA-Lewis Research Center, Cleveland, Ohio 44135

16. Abstract

The objective of the Core Compressor Exit Stage Study Program is to develop rear stage blading designs that have lower losses in their endwall boundary layer regions.

A baseline Stage A was designed as a low-speed model of Stage 7 of the 10-stage AMAC compressor whose preliminary design was identified in a previous study. Candidate rotors and stators were designed which have the potential of reducing endwall losses relative to the baseline. Candidate Rotor B uses a type of meanline in the tip region that unloads the leading edge and loads the trailing edge relative to the baseline Rotor A designs. Candidate Rotor C incorporates a more skewed (hub strong) radial distribution of total pressure and a smoother distribution of static pressure on the rotor tip than those of Rotor B. Candidate Stator B embodies twist gradients in the endwall region. Candidate Stator C embodies airfoil sections near the endwalls that have reduced trailing edge loading relative to Stator A.

Tests of the baseline and candidate bladings were conducted in the General Electric Low Speed Research Compressor using four identical stages to produce a true multistage environment. Single-stage tests were also conducted. The test data were analyzed and performance comparisons were made. Several of the candidate configurations showed a performance improvement relative to the baseline.

This report summarizes the results obtained in the test program and examines the effects of blade shape and vector diagram type on compressor performance. It also compares multistage and single-stage performance results.

17. Key Words (Suggested by Author(s))	18. Distribution Statement
Compressor Core Compressor Design Report	Unclassified - Unlimited

19. Security Classif. (of this report)	20. Security Classif. (of this page)	21. No. of Pages	22. Price*
Unclassified	Unclassified	95	

* For sale by the National Technical Information Service, Springfield, Virginia 22161

TABLE OF CONTENTS

TABLE OF CONTENTS (Concluded)

LIST OF ILLUSTRATIONS

LIST OF ILLUSTRATIONS (Continued)

LIST OF ILLUSTRATIONS (Continued)

LIST OF ILLUSTRATIONS (Continued)

LIST OF ILLUSTRATIONS (Concluded)

LIST OF TABLES

1.0 SUMMARY

The objectives of the Core Compressor Exit Stage Study Program were (1) to develop improved airfoil shapes for reducing endwall losses by a goal of 15% compared to current technology levels and (2) to determine whether single-stage test results can be used to predict multistage compressor performance. The General Electric Low Speed Research Compressor was the principal tool used in this program. Tests were conducted in both multistage and single-stage configurations.

Airfoil shapes and vector diagrams were developed which gave an improvement in compressor performance relative to the baseline Rotor A/Stator A blading. The following test results were obtained. All data are given relative to the baseline performance.

- Rotor B used airfoil sections in the tip region that unloaded the leading edge and loaded the trailing edge relative to the baseline Rotor A. Running with Stator A, Rotor B showed a 0.24 point improvement in efficiency at the design point.

- Stator B used a vector diagram that incorporated high stator exit swirl angles and hence lower axial velocities in the endwall regions relative to the baseline. This required blade sections which were twisted closed locally in the endwall regions. Running with Rotor A, Stator B showed a significant improvement in the pressure-flow characteristic near stall and a 0.41 point improvement in design point efficiency.

- Rotor B running with Stator B showed the same significant improvement in the pressure-flow characteristic near stall and a 0.30-point improvement in design point efficiency. The range of the high efficiency region first obtained with Rotor A/Stator B has also been maintained.

- Rotor C used a vector diagram that had a hub-strong total pressure profile and used airfoil sections in the tip region designed to compensate for the effects of secondary flow and tip leakage. Running with Stator B, Rotor C produced a 0.48 point improvement in efficiency at the design point.

- Stator C embodied airfoil sections near the endwalls that had reduced trailing edge loading and increased leading edge loading relative to the baseline. There was a slight loss in design point efficiency and a 0.30 point loss in peak efficiency for Stator C running with Rotor A.

Meeting the goal of achieving a 15% reduction in endwall loss was only partially successful. The most improvement in efficiency obtained was 0.48 point which amounts to about a 10% reduction in endwall losses, assuming the endwall loss is one-half of the total loss.

The use of single-stage test results to evaluate multistage compressor performance meets with some difficulty. Significant differences were found in pressure-flow characteristics when single-stage results were compared to multistage results. The downstream stages pulling on the first stage appears to have a stabilizing effect on the first stage. In addition, because the inlet guide vanes do not load-up like stators do when a compressor is throttled, the inlet conditions to a single stage are different from those to an embedded stage during throttling of the compressor.

2.0 INTRODUCTION

Preliminary design studies of advanced turbofan core compressors (Reference 1) have indicated that such compressors must have very high efficiencies, as well as the advantages of compactness, light weight, and low cost, in order for advanced overall engine/aircraft systems to have an improved economic payoff. Assessments of loss mechanisms, such as those of Reference 2, suggest that approximately half of the total loss in the rear stages of a multistage compressor is associated with the endwall boundary layers. Since only a relatively small amount of past research has been dedicated to the problem of finding improved airfoil shapes for operation in the endwall boundary layer regions of multistage compressors, it is believed that substantial improvements in that area are likely. Accordingly, a goal of a 15% reduction in the endwall boundary layer losses of rear stages, compared to current technology levels, has been set. The Core Compressor Exit Stage Study Program was directed at achieving this goal. Blading concepts that offer promise of reducing endwall losses have been evaluated in a multistage environment. This report summarizes the results obtained in the program and then addresses three major issues. First, do some novel types of airfoil sections or blade setting procedures give lower losses than others? Second, do some types of vector diagrams give lower endwall losses than others? Third, how does the performance of a given stage tested in the multistage environment compare with the performance of the same stage tested as an isolated stage or as a front stage?

3.0 PROGRAM DESCRIPTION AND OVERALL RESULTS

The Core Compressor Exit Stage Study Program had the primary objective of developing rear stage blade designs that have improved efficiency by virtue of having lower losses in their endwall boundary layer regions. The program was conducted in the following manner: First, an advanced technology, high-speed core compressor was selected as a representative compressor for modeling purposes. Next, a low-speed aerodynamic scale model of one of the rear stages of the high-speed compressor was designed as a baseline stage and tested in the General Electric Low Speed Research Compressor. Candidate bladings, which had the potential of reducing endwall loss and hence improving performance, were also designed and tested. Then performances of the various blading designs were evaluated and compared. Performance improvements were documented.

In this section, the technical approach used to design and evaluate the baseline and candidate bladings to achieve the goals of the program is discussed and the overall performance results are presented.

3.1 LOW SPEED MODELING AND TESTING CONCEPT

The low speed modeling and testing concept is based on aerodynamic similarity. Fundamental fluid dynamic principles and reasoning are used to obtain normalized airfoil surface velocity distributions, vector diagrams, reactions, aspect ratios, solidities, and Reynolds numbers for the low speed blading that are the same as those for the high-speed compressor. This low speed model is then tested in General Electric's Low Speed Research Compressor (LSRC) facility where the principal advantages of large size (1.5 m diameter) and low tip speed (60 m/sec) enable very detailed data to be obtained and precise identification of aerodynamic losses to be made without risk of instrumentation blockage effects. It is very difficult to determine these losses in a high speed core compressor where blade heights of the rear stages may be quite small. With the rotor chord lengths of about 9 cm that result from use of a radius ratio of 0.85 and an aspect ratio of 1.2, the blade chord Reynolds number is about 360,000. This is approximately half that existing in high-speed compressors operating at subsonic altitude cruise conditions and is close enough to provide a proper simulation.

The details of the low-speed modeling concept are presented in Volume I (Reference 3).

3.2 LOW SPEED RESEARCH COMPRESSOR

The General Electric Low Speed Research Compressor (LSRC) facility was used for this test program. The LSRC configuration, shown schematically in Figure 1, consisted of four identical compressor stages having a constant casing diameter of 1.524 m (60 in.) and a radius ratio of 0.85.

A photograph of the LSRC is shown in Figure 2. A detailed cross section of one stage is shown in Figure 3. The airfoils are 11.43 cm (4.5 in.) in span and approximately 9 cm (3.5 in.) in chord - large enough that blade edge and surface contburs can be closely controlled during manufacture. The blade and vane contruction resulted in hydraulically smooth surfaces at the Reynolds numbers necessary to simulate high-speed compressor performance. Single-stage configurations were also tested.

The nominal rotor tip-clearance-to-blade-height was 1.36% and the stator seal-clearance-to-blade-height was 0.78%. Circumferential groove casing treatment was applied over the tip of only the first rotor to assure that Stage 1 would not be the stall limiting blading.

A detailed description of the LSRC facility, the instrumentation, and the data reduction/analysis methods is presented in Volume II (Reference 4) Sections 4.1, 4.3, and 4.5, respectively.

3.3 TEST STAGES

The baseline Stage A was a low speed model of Stage 7 of the 10-stage, 23:1 pressure ratio, AMAC study compressor whose preliminary design study was conducted under Contract NAS3-19444 (Reference 1). The low speed modeling was accomplished by modifying the camber line of the low speed airfoil sections so that the dimensionless suction surface velocity distributions of the low speed sections were similar to those of Stage 7 of the AMAC compressor. The baseline Rotor A consisted of airfoil sections having modified circular arc meanlines and circular arc thickness distributions. The baseline Stator A consisted of airfoil sections having a 65-series thickness distribution on modified circle arc meanlines. An IGV was designed to give the required preswirl to the fluid entering the first rotor in order to achieve a multistage environment in as few stages as practical. Standard General Electric IGV design practices were employed. The details of the baseline Stage A design and the IGV design are presented in the Design Report (Reference 3).

Rotor B was designed to the same set of vector diagrams as Rotor A, but used a type of meanline in the tip region that unloaded the leading edge and loaded the trailing edge relative to Rotor A. Low-speed test results had indicated that very small rotor wakes are present in the tip region of rotors similar in design to Rotor A. This region should therefore be able to take higher trailing edge loading without undue risk of separation. The modification to the tip region was blended into the pitchline so that Rotor A and Rotor B were identical from the pitchline to the hub. A photograph of Rotor B and a comparison of Rotor A and Rotor B tip sections are shown in Figure 4. The details of the design are presented in Volume I (Reference 3), and additional results are presented in Volumes III and IV (References 5 and 6).

Stator B embodied blade sections twisted closed locally in the endwall regions similar to those used in a highly loaded NASA single stage that had rather good performance for its loading level. Different vector diagrams

were calculated to account for the high values of swirl angle near the endwalls. The appearance of Stator B is quite different from that of Stator A because of the twist gradients and because the vane was stacked at 30 percent chord from the leading edge in order to reduce the leading edge lean angle. Photographs of Stator B are shown in Figure 5. The details of the design are presented in Volume I (Reference 3).

Rotor C was designed to produce a radially nonconstant distribution of total pressure of ±24% of stage exit pitchline dynamic head, as compared to the ±9% distribution of Rotors A and B. This produces a higher axial velocity in the hub region relative to Rotor A. The airfoil shape in the Rotor C tip region was designed to compensate for the effects of secondary flow and tip leakage by producng a smoother suction surface velocity distribution when these effects were present. A comparison of the Rotor B and C airfoil tip sections is shown in Figure 6. The design details for Rotor C are presented in Volume V (Reference 7).

Stator C embodied airfoil sections near the endwalls that had reduced trailing edge loading and increased leading edge loading relative to Stator A. A photograph of Stator C and a comparison of the Stator A and Stator C airfoil sections are presented in Figure 7. The airfoils were designed to the same vector diagram as Stator A. The design details are presented in Volume I (Reference 3).

3.4 TEST PLAN

The overall test program was divided into four parts as outlined in Table 1. The first part involved extensive testing of the baseline blading, Stage A, which consisted of Rotor A/Stator A in both four-stage and single-stage configurations. The test results can be found in Volume II (Reference 4) of this series. The second part involved a series of short screening tests to select the best rotor design and the best stator design based on tests in four-stage configurations. These test results can be found in Volume III (Reference 5). The third part involved extensive testing of the best rotor and best stator designs which consisted of Rotor B/Stator B in both four-stage and single-stage compressor configurations. These test results can be found in Volume IV (Reference 6). The final part of the test program consisted of extensive testing of the Rotor C design in a four-stage configuration with Stator B; these test results can be found in Volume V (Reference 7).

Eight types of data were taken at various times during the test program: stall determination data, preview data, standard data, casing treatment data, Reynolds number data, blade surface pressure data, blade element data, and detailed wall boundary layer data. A description of each of these types of data is presented below.

Stall determination data yield the stalling throttle setting by observing the sudden decrease in the static pressure rise across the compressor at stall and listening for the onset of rotating stall. Preview data provide stage

characteristics and efficiency measurements based on casing static pressure rise, measured airflow, and measured torque. Standard data provide compressor performance based on mass-averaged total pressure rise from Rotor 1 inlet to Stator 4 exit, measured airflow, and measured torque. Casing treatment data provide a means of assuring that the first stage was not the stall limiting stage. Reynolds number data are used to establish performance trends versus Reynolds number as an aid in extrapolating the test data to the somewhat higher Reynolds number levels of engines. Blade surface pressure data provide a means of determining regions of favorable leading edge loading (incidence), rates of diffusion, and regions of separated flow on the airfoil. Blade element data give blade element performance and stage vector diagram quantities based on total pressure, static pressure, and flow angle measured in a matrix of circumferential and radial locations. Sufficient data are obtained to define the wake. Measurements are taken at the rotor inlet, rotor exit, and stator exit of the test stage. Detailed wall boundary layer data consist of total pressure, static pressure, and flow angle measurements as close as 1% of blade height to either endwall. Evaluation and comparison of all these data from the various configurations have provided a means of assessing the effectiveness of the particular design approaches employed for reducing losses in the endwall region.

3.5 OVERALL PERFORMANCE RESULTS

Overall performance comparisons for the various blading configurations tested in the Core Compressor Exit Stage Study Program are presented in this section and tabulated in Table 2. The overall performance was determined from preview data and standard data. Test data are presented as graphs of pressure coefficient, work coefficient, and torque efficiency plotted as a function of flow coefficient. The tests were conducted at an average rotor tip-clearance-to-blade-height ratio of 1.36% and an average stator seal-clearance-to-blade-height ratio of 0.78%. The test Reynolds number was 3.6×10^5. As discussed previously, casing treatment was applied over the tip of the first rotor only to assure that Stage 1 would not be the stall limiting blading.

3.5.1 Baseline Rotor A/Stator A

The overall performance of the four-stage Rotor A/Stator A configuration is presented in Figure 8 and tabulated in Table 2. The design intent pressure coefficient of 0.556 has been achieved at the design intent flow coefficient of 0.407. At the design pressure rise, the measured efficiency of 0.900 was equal to the design target. Peak efficiency of 0.9045 occurs at a flow coefficient of 0.388, and peak pressure rise occurs at a flow coefficient of 0.364. At values of flow coefficient less than 0.364, the pressure flow characteristic rolls over and flattens out until a crisp rotating stall occurs. Additional performance details are presented in Volume II (Reference 4).

3.5.2 Rotor B/Stator A

The performance of Rotor B, which has a tip section that unloads the leading edge and loads the trailing edge relative to Rotor A, is compared to the performance of the baseline Rotor A in Figure 9 and in Table 2. Rotor B and Rotor A are both running with Stator A. The important feature of this performance comparison is the 0.24 point improvement in efficiency obtained at the design point and at higher flows with Rotor B. Additional performance results are presented in Volume III (Reference 5).

3.5.3 Rotor A/Stator B

The performance of Stator B, which embodies twist gradients in the endwall regions, is compared to the performance of the baseline Stator A in Figure 10 and Table 2. Stator B and Stator A are both running with Rotor A. Two important features of this performance comparison are (1) an improvement in efficiency at every flow tested using Stator B with a 0.41 point improvement obtained at the design point and (2) a significant improvement in the pressure-flow characteristic obtained near stall using Stator B. The 3.2% improvement in peak pressure coefficient and the 5.4% improvement in flow range from the design point to the peak pressure rise point result, in part, from more favorable airfoil pressure distributions, especially near the hub.

Consideration of stage matching was reviewed. During the design of Stator B, reported in Reference 3, a stage matching analysis was conducted to see if a new rotor might be needed to match the Stator B vector diagrams. However, upon comparing the rotor inlet relative air angles that would be produced by Stator B with the Rotor A design air angles (Reference 3, Figure 10), it was concluded that Rotor A was well matched with Stator B. Differences in air angles were negligible except in the endwalls where, near the casing, the Rotor A relative air angles were less than those required for Stator B, varying from zero degrees less at 10% immersion to 3° less at zero percent immersion. The differences at the hub were less than 1.5°. New rotor blading could not be justified for these small localized differences in rotor air angles seen near the endwalls. Rotor endwall diffusion factors were calculated to be 10% to 15% higher.

The 6% increase in stalling flow coefficient for Stator B is not thought to be too significant, especially in view of the 5.4% improvement in flow range from design to peak pressure rise, since rear stages of this type often do not operate beyond the peak pressure rise point in a high-speed compressor. Also, there is a very slight increase in pumping for the Rotor A/Stator B configuration. Additional performance results can be found in Volume III (Reference 5).

3.5.4 Rotor B/Stator B

Since the Rotor B design and the Stator B design both showed a performance improvement when compared with the baseline, a four-stage configuration

consisting of Rotor B/Stator B was tested. The performance of this configuration is compared to the performance of the baseline Rotor A/Stator A configuration in Figure 11 and Table 2. The performance of the Rotor B/Stator B configuration generally follows that of the Rotor A/Stator B configuration but with slightly higher efficiencies at flow rates larger than design flow and slightly lower efficiencies at flow rates smaller than design. When compared with the baseline, Rotor B/Stator B shows (1) a 0.30 point improvement at the design point and (2) a significant improvement in the pressure-flow characteristics near stall. Apparently the efficiency gains achieved individually by Rotor B (0.24 point) and Stator B (0.41 point) are not additive. Possibly the higher trailing edge loading inherent in the Rotor B tip section causes more loss when run in the higher rotor endwall loading environment of the Stator B-type vector diagrams than when run with the more conventional Stator A-type vector diagrams. The 2.8% improvement in peak pressure coefficient and the 5.4% improvement in flow range from the design point to the peak pressure point result from a more favorable pressure distribution on the stator, especially near the hub. The 5.4% improvement in flow range from design to peak pressure rise obtained with the Rotor A/Stator B configuration has been maintained. Rotor B/Stator B was selected as the "Best Stage" because, in addition to the improvements shown at low speed, an added efficiency improvement might be expected at higher Mach numbers due to the reduction in peak suction surface velocity on the tip section. Comprehensive test data are presented in Volume IV (Reference 6).

3.5.5 Rotor C/Stator B

The overall performance of Rotor C is compared with that of Rotor B in Figure 12 and Table 2. The pressure-flow characteristics are nearly identical, but Rotor C stalls at 2% lower airflow. This could be because the first rotor tip is governing and the Rotor C tip is more closed. A 0.18 point improvement in efficiency is apparent with Rotor C relative to Rotor B at flow coefficients larger than the design point. (Note: Relative to Stage A, a 0.48 point improvement in efficiency was obtained with Rotor C/Stator B.) A small improvement in overall peak efficiency and an increase in the range of the high efficiency region is obtained with Rotor C. An additional 0.14 point in efficiency should be credited to Rotor C compared to Rotor B to adjustment for tip clearance. Rotor C actually ran with a slightly larger rotor tip-clearance-to-blade-height of 1.53% compared to 1.43% for Rotor B. Comprehensive test data are presented in Volume V (Reference 7).

3.5.6 Rotor A/Stator C

The performance of Stator C, which has reduced trailing edge loading and increased leading edge loading near the endwalls, is compared to that of Stator A in Figure 13 and Table 2. Stator C and Stator A are both running with Rotor A. There is a 0.3 point loss in peak efficiency using Stator C. The slight loss in efficiency for Stator C at the design point is within experimental accuracy. Stator C shows no obvious advantages over Stators A or B. The test data are presented in Volume III (Reference 5).

4.0 EFFECT OF BLADE SHAPE

In this section, the effect of blade profile shape on compressor performance is examined. Three different airfoil profile shapes, Rotor B tip, Rotor C Tip, and Stator C hub and tip described in Section 3.3, were tested. Generally speaking, the airfoil profiles were modified in the endwall region relative to the Stage A baseline, and these modifications were faired to the original baseline shape in the midstream portion of the annulus (30% to 70% immersion).

4.1 OVERALL PERFORMANCE

Rotor B and Rotor C both produced modest improvements in compressor efficiency, as shown in Figures 9 and 12, with relatively little difference in the shape of the pressure-flow characteristic. In both cases, modifications to the rotor tip section were made. For Rotor B, in which the leading edge was unloaded and the trailing edge was loaded relative to the baseline, as shown in Figure 4, there was a back-to-back test using the same Stator A and the same vector diagram type. Consequently, the performance improvement of 0.24 point in efficiency at the design point could be attributed to the airfoil profile modification. At lower flow coefficients between 0.37 and 0.39, the efficiency with Rotor B is lower than that with Rotor A. For Rotor C, in which both a modification to the airfoil profile (as shown in Figure 6) and a vector diagram change were made, the cause of the performance improvement of 0.18 point in efficiency relative to Rotor B at design point was not clear.

Although the 0.41 point improvement in operating line efficiency and the substantial improvement in pressure-flow characteristics near stall using Stator B is classified as resulting from a vector diagram change, an interesting comparison is shown in Figure 14. The pressure-flow characteristics are plotted for Stage 1 of the four-stage configuration and for the average of Stages 2, 3, and 4 of the four-stage configuration consisting of Rotor A/Stator A and Rotor A/Stator B. Since both configurations are operating with the same Stage A type inlet guide vane, the first rotor sees the same A-type vector diagram conditions at the inlet in both cases, and the first stator of either type sees Stage A-type inlet conditions. The Stator B end-bends permit a higher pressure coefficient to be obtained near stall. In Stage 1, Stator B runs with low incidence angles and low loadings in the endwalls, and the strengthening seen in the Stage 1 characteristic is thus due to these factors and not due to the change in vector diagram. In the rear stages, however, the repeating stage environment is established, and the rear stages are not unloaded in the endwalls. The data in Figure 14 show a significant improvement in the pressure-flow characteristic near stall for the rear block average. Consequently, although some of the performance improvement obtained using Stator B could be due to the use of the Stage A-type inlet guide vane with Stator B, a larger part appears to result from the vector diagram change.

The blading modifications for Stator C, which produced an increased leading edge loading and a reduced trailing edge loading, resulted in a modest efficiency penalty of -0.05 point at the design point and -0.30 point at peak efficiency compared to Stator A when both were run with Rotor A.

In order to understand the reasons for the performance changes obtained, the details of the flow field were examined more closely as discussed in the next section.

4.2 BLADE ELEMENT PERFORMANCE

Variations of loss coefficients, deviation angles, D-factors, incidence angles, and total pressures were plotted for all configurations tested. These are shown at design throttle setting in Figures 15 through 19 and in the Appendix Figures A1 through A5. Attention was paid to trends in the endwall regions to see what effect different blade shapes had on loss coefficients, etc.

The radial variation of rotor and stator loss coefficient are shown in Figure 15. It is clear from the figure that rotor loss coefficients for all three configurations are nearly the same. Apparently the changes in loss coefficient resulting from the changes in blade shape were not large enough to be measured. On the other hand, the stator losses are larger in the endwall regions for the Rotor A/Stator A configuration than for the others. In fact the hub region of Stator A clearly has higher losses than those of Stator B. However, this most likely results from a vector diagram change that will be discussed in Section 5.2. Note that the Stator B loss coefficient is lower with Rotor C than with Rotor B, so maybe the higher efficiency of Rotor C is due more to vector diagrams than to the different rotor tip airfoil shape.

The deviation angles, diffusion factors, and incidence angles presented in Figures 16 through 18 show that Rotor C is operating with slightly higher deviation angles and diffusion factors in the tip region and slightly higher incidence angles in the midspan region. But there are no clear indications of the causes for improved performance in the rotors. In Figure 18, the lower incidence angles of Stator B running with Rotor C may explain part of the performance improvement for that configuration.

The radial variation of normalized total pressure at the compressor discharge is shown in Figure 19 for the various blading types that maintain a constant total pressure. Rotor C will be treated later. As expected, there is no meaningful difference in the pressure profiles due to the blade shapes tested.

Since the gains in efficiency were modest, being from 0.1 to 0.4 point, it is not surprising that any effect of changes in blade shape on the radial variation of these blade element parameters was lost in the data scatter. Consequently, one could not identify the precise causes for the performance

improvement. The detailed comparisons are presented for completeness in the Appendix, Figures A1 through A5.

4.3 BLADE AND VANE SURFACE STATIC PRESSURE

Comparisons of measured static pressure distributions on the airfoil surfaces for the various different blading shapes show that in each case the intended pressure distribution was either achieved or nearly achieved. In this section only those comparisons near the endwalls will be made, since this is where the blading modifications are most apparent.

In Figure 20, a comparison of rotor surface static pressures is made for Rotors A and B at 5% immersion. Both rotors are running with Stator A. The design intent of unloading the leading edge region and loading the trailing edge region relative to Rotor A has been achieved. Although Rotor B appears to be running at slightly lower incidence angles, there is no clear indication of the cause of the performance improvement achieved by Rotor B. The pressure distributions for Rotor A and B near the hub, shown in Figure 21, are the same. This is an expected result since both rotors have the same hub airfoil section.

The pressure distribution in the tip region of Rotor C, shown in comparison with that of Rotor B in Figure 22, exhibits some of the "smoothing" on the suction surface that was intended by the special airfoil sections, particularly right at the leading edge. The data show that the forward third of the blade has more loading and the aft portion has less loading than Rotor B, but there is no evidence to indicate flow separation or other detrimental conditions for either airfoil.

The pressure distributions obtained in the endwalls for Stator C are compared with those for Stator A in Figures 23 and 24. Clearly, Stator C has a larger airfoil loading near the leading edge and a smaller loading near the trailing edge, as was intended. However there is no indication of an increase in flow separation in Stator C that would explain its poorer efficiency.

In summary, the effects of changes in blade shape on surface static pressure distributions are readily apparent in the data, although there is no clear indication in these data of the causes for improved or reduced efficiency of the various designs. The changes in efficiency for the various designs are small, and the correlation between these changes and the changes in surface static pressure distribution are not straightforward for this blading.

5.0 EFFECT OF VECTOR DIAGRAM TYPE

In this section, the effect of vector diagram type on compressor performance is examined. Three types of vector diagrams were tested. The Rotor A/Stator A type, described in Reference 3, had a radial variation of total pressure which was somewhat higher-than-average near the hub and somewhat lower-than-average near the tip producing a ±9% radial variation in stage exit dynamic head. The Stator B type of vector diagram, also described in Reference 3, incorporated higher stator exit swirl angles and lower axial velocities in the endwall regions and higher axial velocities in the pitch-line region relative to the Stage A type. This reduced the amount of flow passing through the endwall region. The Rotor C vector diagram type, described in Reference 7, produced a significantly higher total pressure from pitchline-to-hub and lower total pressures from pitchline-to-tip than the Rotor A type, but with the same overall average. The radially nonconstant distribution of total pressure for Rotor C was designed to be ±24% of stage exit dynamic head compared to ±9% for Stages A and B. The higher hub total pressure increased the dynamic head entering all blade rows and helped reduce loading in the hub region. Rotor C was tested with Stator B.

5.1 OVERALL PERFORMANCE

The Stator B-type vector diagram produced a significant improvement in the pressure-flow characteristic near stall and a modest improvement in efficiency across the whole flow range compared to the Stator A type as described in Section 3.5.3, Figure 10. Although the Rotor C-type of vector diagram and the several changes in blade shape produced similar modest improvements in efficiency as shown in Figures 9 through 12, only the Stator B-type vector diagrams produced this substantial improvement in the pressure-flow characteristic. Evidence presented in the following sections indicates that this improvement resulted from reduced separation and healthier flow in the hub region.

The Rotor C-type vector diagram also produced a modest improvement in compressor efficiency compared to the B-type as discussed in Section 3.5.5, Figure 12. However, the reason for this improvement was not so readily apparent.

5.2 BLADE ELEMENT PERFORMANCE

The radial variation of normalized total pressure including casing and hub static pressure at the compressor discharge for various throttle settings is presented in Figure 25 for the three different types of vector diagrams tested. The pressure distributions for the A-type and the B-type are very similar for the design point throttle and the peak efficiency throttle. However at the peak pressure rise throttle, the hub region begins to collapse for the A-type vector diagram while the hub remains stronger for the B-type. For

the C-type vector diagram, the strengthened hub profile is evident at all throttles shown. Rotor C was not tested with an A-type stator, consequently the effect of the strong hub with a more conventional radial distribution of swirl is not known.

Presentations of radial pressure variations for the A- and B-type vector diagrams at Stage 2 are shown in Figure 26. The difference between the total pressures at the stator inlet and exit planes represents the loss. The relatively higher losses at both endwall regions is seen in the figure. However, the significant increase in loss from 50% immersion to the hub for the A-type vector diagram near stall is clearly evident in Figure 26b. It should be noted that the data in Figure 26b is for a throttle setting somewhat more closed than that in Figure 26d since Stage A could be throttled to lower flows than Rotor B/Stator B. This does not change the main message that Stator A hub flow becomes worse than Stator B hub flow near stall.

Comparisons of the radial pressure variations for the B- and C-type vector diagrams are shown in Figure 27. The significant hub strong tilt in pressure distribution is apparent although no change in the loss coefficients in the hub region is obtained as a result. A decrease in stator incidence angle was observed, and this may be responsible for the small efficiency improvement obtained with Rotor C/Stator B.

The radial variation of stator loss coefficient in Figure 15 also shows the A-type vector diagram to have more loss than the B-type in the stator hub region.

The loss coefficient, diffusion factors and deviations angles were plotted as functions of incidence angle for all of the types of vector diagrams tested. Particular attention was paid to examining trends in the endwall regions to see what effect different types of vector diagrams had on loss coefficients, etc. The most revealing of these trends is shown in Figure 28 where loss coefficient is plotted as a function of incidence angle. It is seen in this figure that Stator A is operating at much larger values of incidence angles and loss coefficients near the hub than the other stators are, especially near stall. Figures 15 through 18 have already shown that at the design point, Stage 3 radial profiles of incidence angle and diffusion factor were not greatly different between Stages A and B, indicating that the stages are equally well matched, but hub loss coefficients are higher in Stator A.

However, except for this result, the detailed comparisons of this type did not reveal noticeable trends or differences that would allow one to identify the causes of the performance improvement. The gains in efficiency were small, being on the order of 0.1 to 0.4 point, and any effect this had in the radial variation of loss coefficient, diffusion factor, or deviation angle was lost in the data scatter. These detailed comparisons are presented for completeness in the Appendix, Figures A1 through A5.

5.3 BLADE AND VANE SURFACE STATIC PRESSURE

Comparisons of static pressure measurements on vane surfaces at the endwalls for the Stator B and Stage A-type vector diagrams are presented in Figures 29 and 30. It is easily seen in Figure 29 that the Stator B hub is operating with less leading edge loading and more favorable incidence angle than the Stator A hub. In addition, from 70% chord to the trailing edge, Stator B is operating with substantially less evidence of flow separation on the suction surface than Stator A. This helps to show where the improvement in performance occurred using the B-type vector diagram.

Interestingly, the comparison of surface pressures at the tip in Figure 30 show no significant difference with a change in vector diagram type. This is further evidence that it is the change in the hub region which produces the performance improvement.

Comparisons of the static pressure measurements on blade surfaces at the hub for the Rotor C-type vector diagram are presented in Figure 31. Rotor C has a bit more loading near the leading edge than Rotor B, but otherwise the distributions are nearly the same. The stator pressure distributions were also the same. Consequently, the cause of any performance improvement is not evident in the surface pressure distributions.

Complete sets of surface pressure distributions are given in the Data Reports (References 4 through 7) for all immersions and throttles tested. The reader is referred to these reports for additional results.

6.0 SINGLE-STAGE VERSUS MULTISTAGE TEST RESULTS

In this section, the question of how the performance of a given stage, tested in the multistage environment, compares with the performance of the same stage tested as an isolated single stage or as a front stage is addressed. To provide answers to this question, tests were conducted in both multistage and single-buildups using Rotor A/Stator A and Rotor B/Stator B blading. The detailed results of the test are found in References 4 and 6, and the main results are summarized here.

6.1 OVERALL PERFORMANCE

Overall performance comparisons of the single-stage and multistage configurations are presented in Figure 32 and Table 2 for the Rotor A/Stator A and Rotor B/Stator B blading. For both blading designs, the single-stage configuration pumps more flow than the four-stage average, and the single-stage configuration achieves a higher peak pressure coefficient, as seen in Figure 32a and b and Table 2. However, the peak efficiency of the single-stage configuration is lower than that of the four-stage configuration.

It is suprising that the single-stage efficiency should be as much as two points lower than the four-stage efficiency. As discussed in Volume IV (Reference 6), much of this difference is probably due to inaccuracies in measurement/evaluation of the tare torque of the four-stage configuration relative to that of the single-stage configuration. This does not affect the relative efficiency comparisons of all four-stage configurations nor does it affect the relative efficiency comparisons of the single-stage configurations.

The individual characteristics of the single-stage and four-stage configurations are compared in Figure 33a and b. The single-stage characteristic is not quite so steep as the first stage characteristic of the four-stage configuration. Compared to the Stage 3 characteristic of the four-stage configuration, the single-stage characteristic has about the same slope but is operating at about 2.5% higher flow and about 4% higher pressure coefficients. The significant differences in the characteristics occur at lower flow coefficients. Both the single stage and the first stage of the multistage configuration achieve higher peak pressures than those of the other stages. This difference is probably due in large measure to better inlet conditions at the first rotor inlet. During throttling, the first rotor inlet is not subjected to the thickened wakes, increased deviation angles, and separated flow that the downstream stages feel. Perhaps even more striking is the higher pressure achieved by the first stage of the four-stage configuration compared to the single-stage configuration. This could result from the casing treatment or from the stabilizing influence of the downstream stages pulling on the first stage of a multistage configuration.

6.2 BLADE ELEMENT PERFORMANCE

The detailed data reported in Volumes II and IV (References 4 and 6, respectively) were examined to determine whether the single-stage configuration had different detailed blade element performance than the multistage configuration. Examples of the comparisons made are shown in Figures 34 through 36 and in the Appendix, Figures A6 through A10. The data shown in Figure 34 are representative. At the design point, there is little if any difference in the rotor loss coefficient when the data for the four-stage configuration's first stage is compared with that for the single-stage configuration and the four-stage configuration's third stage. Only locally at the rotor hub is there a suggestion that the single-stage configuration has slightly higher losses. The results for the stator are similar.

As the throttle is closed from the design point toward stall, it is clear from the data in Figure 35 that the third stage of the four-stage configuration is running at much higher incidence angles than the single-stage or the first stage configuration.

A comparison of the radial variation of normalized total pressure at the compressor discharge is presented in Figure 36 for the single-stage and the four-stage configurations. Pressures for the four-stage configuration have been divided by four in order to make comparisons with the single-stage results. At both throttles presented, the single-stage data exhibits a reduction in total pressure rise at both the tip region (0%-20% immersion) and the hub region (20%-100% immersion) compared to the multistage results. At the peak pressure rise throttle, the higher pressure rise achieved by the single-stage configuration is evident in the figure.

6.3 BLADE AND VANE SURFACE STATIC PRESSURE

A comparison of blade surface static pressures for the four-stage and single-stage configurations is presented in Figure 37 for Rotor A/Stator A for the design point throttle and the peak pressure rise throttle. For these comparisons, the zero level of static pressure was taken as the maximum static pressure measured on the pressure surface, and the difference, ΔP, between this zero level and pressures at other locations on the airfoil was plotted. The data taken near the hub of the rotor for the single-stage configuration (Figures 37d, e, f) show evidence of flow separation in the change in slope and in the flattening of the suction-surface pressure distribution. This begins at about 80% chord in Figure 37c, 70% chord in Figures 37d and e, and 50% chord in Figure 37f. Neither of the other two configurations exhibits such a pronounced effect. Apparently, the downstream stages in the multistage configurations have a stabilizing effect on the first rotor hub.

At the rotor tip (Figures 37a and b) the loading for both the single-stage configuration and the four-stage configuration with the first stage as the test stage is higher than that of the embedded stage.

A comparison of the vane surface static pressures for the multistage and single-stage configurations is presented in Figure 38. The data indicate that the stator is operating about the same for all configurations at the design point. However, at the peak pressure throttle, the stator of both the single-stage and first-stage configurations is running with noticeably less flow separation in the hub (inner diameter region).

7.0 EFFECTS OF TIP CLEARANCE, CASING TREATMENT AND REYNOLDS NUMBER

7.1 EFFECT OF ROTOR TIP CLEARANCE

Overall performance of the Rotor B/Stator B four-stage configuration was obtained at an increased tip-clearance-to-blade-height ratio of 2.80%. The results are presented in Figure 39 and Table 2. Peak efficiency is 0.8898, peak pressure coefficient is 0.572, and stalling flow coefficient is 0.372. The increase in tip clearance costs 1.49 points in peak efficiency, 10.8% loss in stalling flow coefficient, and 9.7% loss in peak pressure rise relative to the nominal clearance.

Comparisons showing the effects of increased rotor tip clearance on blade element performance are presented in Figure 40. Increasing the clearance from 1.4% tip-clearance-to-blade-height ratio to 2.8% produces increases in stator incidence angles, rotor diffusion factors, and rotor loss coefficients from 0% to as much as 20% immersion. Stator incidence angles are increased by several degrees and rotor loss coefficients are nearly 1.8 times larger when tip clearances are doubled.

A comparison showing the effects of increased rotor tip clearance on the static pressure on the blade surface is presented in Figure 41. There is a substantial decrease in blade loading over the first 40% of chord, a rearward shift of peak suction surface velocity, and a reduced pressure on the pressure surface relative to the nominal clearance case. The unloading of the tip region when the compressor is throttled to lower flow coefficients is also shown in the figure. Additional comparisons are shown in the Appendix, Figures A11 and A12.

7.2 EFFECTS OF CASING TREATMENT

Tests in which preview data were taken were conducted using Stage A blading for three different casing treatment window geometries in order to aid in determining the stall-limiting stage and to select the casing geometry to be used throughout the test series. The results are shown in Figure 42.

Although four identical stages were tested, the repeating stage environment was not established until Stage 2 or Stage 3. It is thus very desirable that Stage 1 not be the stall-limiting blading. In order to make this assessment, circumferential groove casing treatment was applied over the Stage 1 rotor tip exclusively. The 8.2% improvement in stall margin, shown in Figure 42 for this configuration, indicates that the first-stage rotor was indeed stall-limiting without casing treatment. This stall margin improvement was obtained with no measurable change in the rest of the pressure flow characteristic or in the efficiency curve. Circumferential groove casing treatment was then applied over all four rotor tips. The slight additional improvement in stall margin shown in Figure 42 indicates that Stage 1 is probably no longer

stall-limiting when casing treatment is used. However, there was a loss in efficiency and a slight loss in pressure rise with treatment over all four rotor tips. Based on these test results, it was decided to conduct all four-stage tests in the program with circumferential groove casing treatment over Rotor 1 tip only and smooth windows over the rest of the rotors.

7.3 EFFECTS OF INCREASED TIP CLEARANCE AND CASING TREATMENT

Overall performance was obtained with both increased tip clearance and casing treatment of all four stages. The results, presented in Figure 43 and Table 2, show a peak efficiency of 0.8915, a peak pressure coefficient of 0.563, and a stalling flow coefficient of 0.3708. This gives a loss of 1.32 points in peak efficiency, a loss of 10.7% in stalling flow coefficient, and a loss of 11.1% in peak pressure rise relative to the nominal Rotor B/Stator B configuration. Apparently, casing treatment at open clearances gave a small performance improvement at the design point but hurt performance near stall.

Comparisons showing the effects of increased rotor tip clearance and casing treatment on vector diagram quantities are shown in Figure 44. The addition of casing treatment at increased clearance produces a significant increase of 13° in absolute air angle and stator incidence angle relative to the nominal clearance case. Near the tip, the flow is nearly tangential with air angles of about 83°. Increases in D-factor and loss coefficient were also observed. Generally, the effects are observed from 0% to 20% immersion.

The addition of casing treatment at increased tip clearance does not significantly alter the blade surface static pressure distributions shown in Figure 41.

7.4 EFFECTS OF REYNOLDS NUMBER

The essentially incompressible flow in the test compressor allows stage performance to be presented as stage characteristics that are independent of speed, although there are small variations in performance due to Reynolds number. In order to determine these performance variations, a series of preview data points was taken at seven different rotative speeds covering a range of Reynolds numbers from 0.94×10^5 to 4.00×10^5. The results presented in Figures 45 and 46 serve as an aid in extrapolating the test data to the somewhat higher Reynolds number levels employed in engines.

The program was not structured to provide comparisons of the relative sensitivity of the various stages to tip clearance, casing treatment, or Reynolds number.

8.0 CONCLUSIONS

Airfoil shapes and vector diagrams were developed which gave improvements in compressor performance relative to the baseline Rotor A/Stator A design. Rotor B used airfoil sections in the tip region that unloaded the leading edge and loaded the trailing edge relative to the baseline Rotor A. Rotor C used a vector diagram that had a hub-strong total pressure profile and used airfoil sections in the tip region designed to compensate for the effects of secondary flow and tip leakage. Stator B used a vector diagram that incorporated high stator exit swirl angles (lower axial velocities) in the endwall regions relative to the baseline. This required blade sections twisted closed locally in the endwall regions. Stator C used airfoil sections near the endwalls that had reduced trailing edge loading and increased leading edge loading relative to the baseline. The principal test results are listed below (all data are given relative to the baseline preformance).

- Rotor B running with Stator A showed a 0.24 point improvement in efficiency at the design point.
- Rotor C running with Stator B produced a 0.48 point improvement in efficiency at the design point.
- Stator B running with Rotor A gave a significant improvement in the pressure flow characteristic near stall and a 0.41 point improvement in efficiency at the design point.
- Rotor B running with Stator B showed the same significant improvement in pressure-flow characteristic near stall and a 0.30 point improvement in efficiency at the design point.
- Stator C running with Rotor A gave a slight loss in efficiency at the design point and a 0.30 point loss in efficiency at peak efficiency.

Achieving the goal of a 15% reduction in endwall loss was only partially successful. The most improvement in efficiency obtained was 0.48 point which amounts to about a 10% reduction in endwall loss, assuming the endwall loss is one-half of the total loss.

From a designer's standpoint, the use of a B-type vector diagram, which incorporated high stator exit swirls and required airfoil sections twisted closed locally in the endwall regions, appears to have the highest overall performance potential.

9.0 LIST OF SYMBOLS AND ACRONYMS

Symbols	Definition
A	Annulus area of the compressor
Alpha	Absolute air angle
AMAC	Advanced multistage axial flow compressor
Beta	Relative air angle
c	Stator shroud seal clearance
C	Absolute velocity
CU	Absolute tangential velocity
CZ	Axial velocity
CAFD	Circumferential average flow determination
ΔCAM	Change in Camber
CASC	Cascade analysis by streamline curvature
F_c	Compressibility correction factor
h	Annulus height
ID	Inside diameter
IGV	Inlet guide vane
LSRC	Low speed reseach compressor
OD	Outside diameter
P	Pressure
P_s	Blade surface static pressure $\equiv P_{surface} - (P_B+P_{ref})$
P_{S_1}	Upstream static pressure
P_{T_1}	Total Pressure
QU	Normalizing quantity = $1/2\ \rho_{ref}\ U_t^2$

Symbols	Definition
R	Radius
Re	Reynolds number
T	Measured torque corrected for windage/bearing friction
U_t	Wheel speed at tip
V	Air velocity
W	Relative velocity
WU	Relative tangential velocity
ϵ	Rotor tip clearance
η	Torque efficiency
ρ	Density
$\bar{\rho}$	Average density across annulus
ϕ	Flow coefficient
ψ	Work coefficient
ψ'	Pressure coefficient
$\bar{\omega}$	Loss coefficient

Subscript

B	Barometer
C	Casing
H	Hub
ref	Reference
S	Static properties
T	Total properties
t	Tip

Symbols	Definition
1	Upstream conditions
2	Downstream conditions
β_1^*	Inlet metal angle
β_2^*	Exit metal angle

10.0 FIGURES

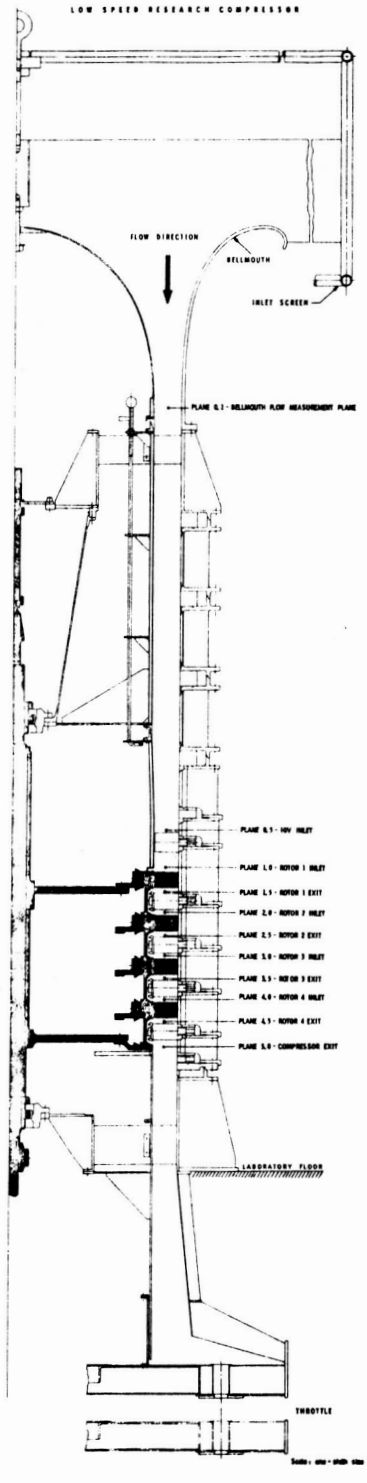

Figure 1. Four-Stage Compressor Configuration Tested in the NASA-GE Core Compressor Exit Stage Study.

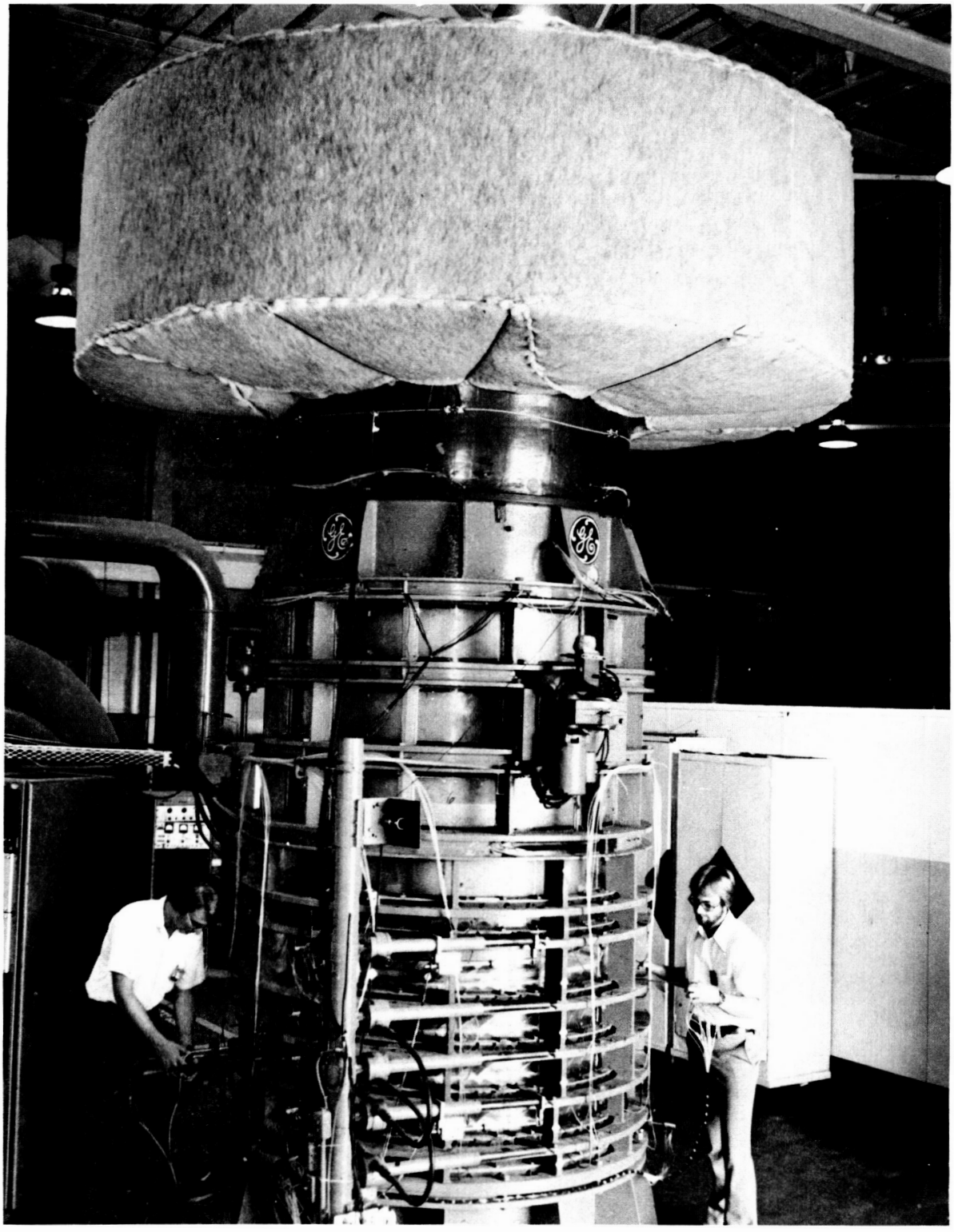

Figure 2. Photograph of the Low Speed Research Compressor.

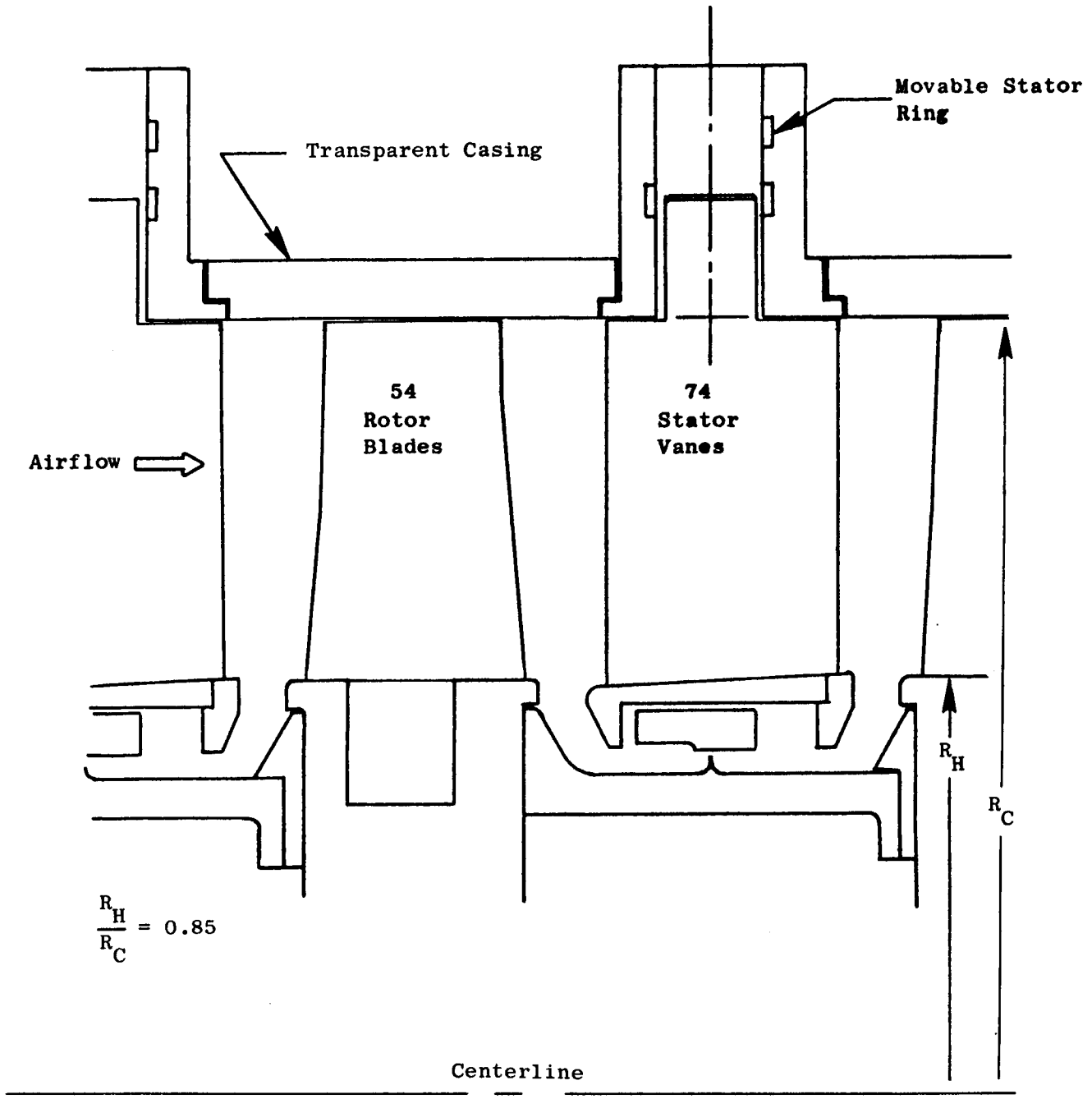

Figure 3. Cross Section of 0.85 Radius Ratio Compressor Stage.

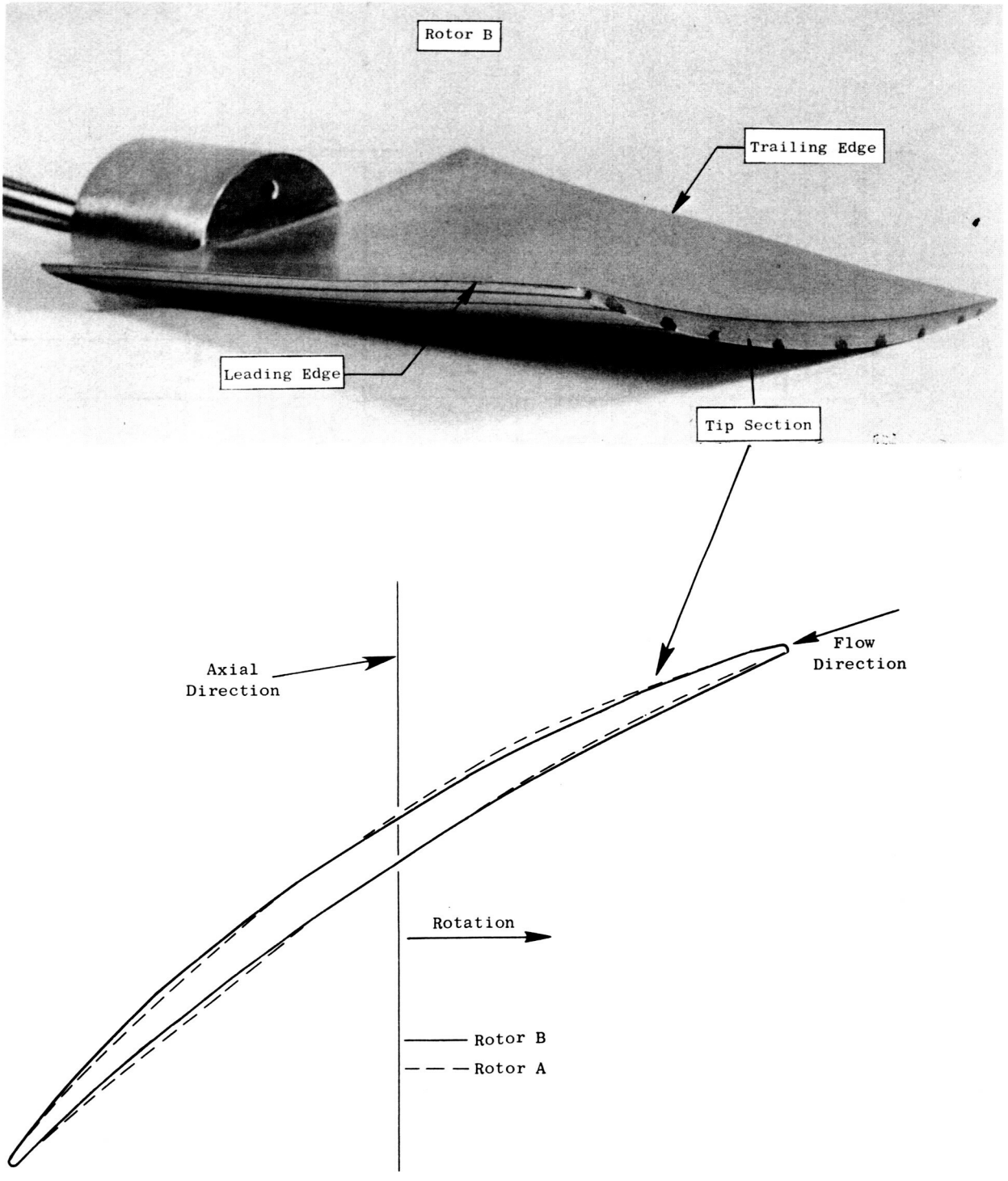

Figure 4. Comparison of the Rotor B and Rotor A Tip Sections.

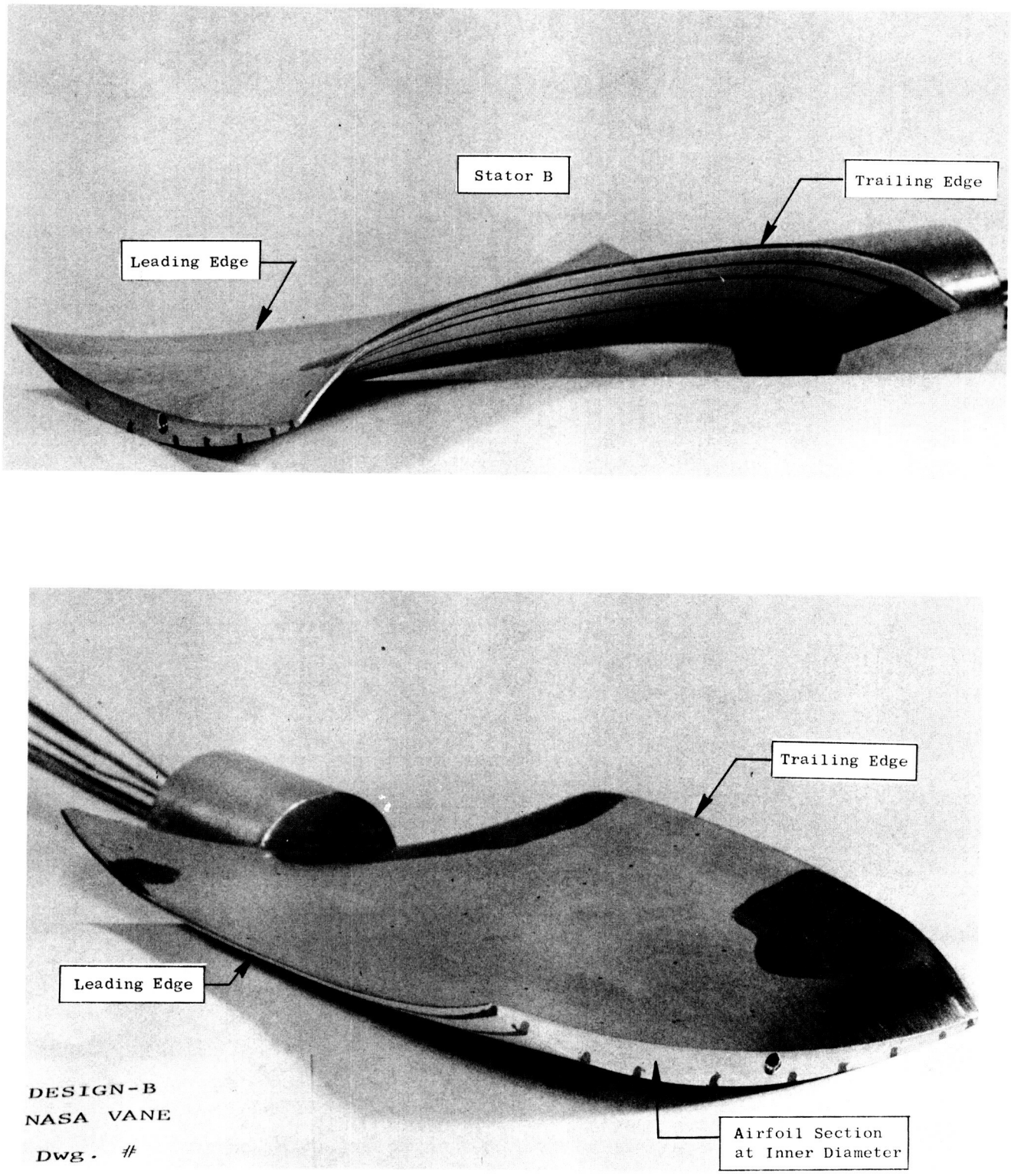

Figure 5. Photographs of Stator B.

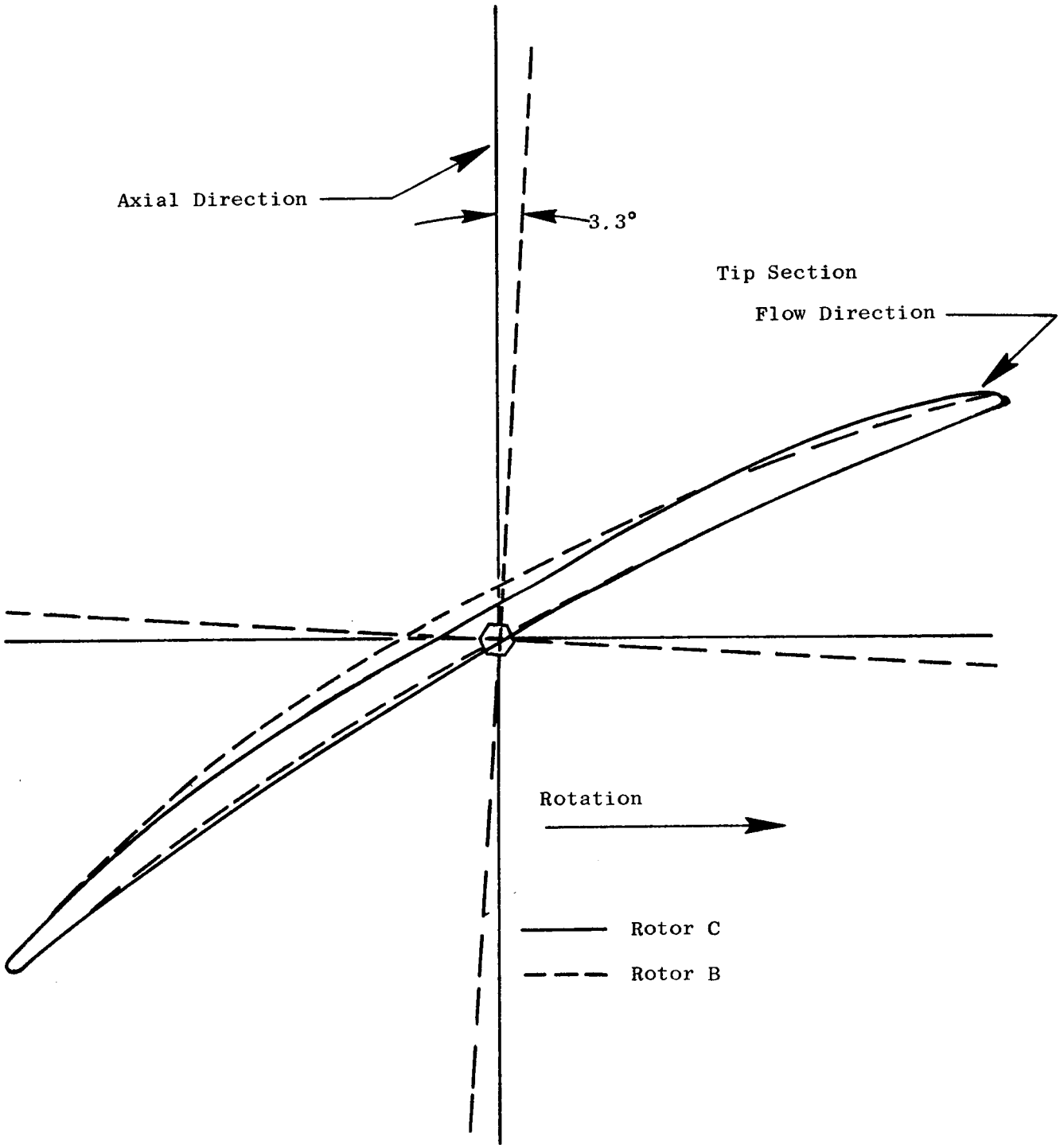

Figure 6. Comparison of Rotor C and Rotor B Tip Sections.

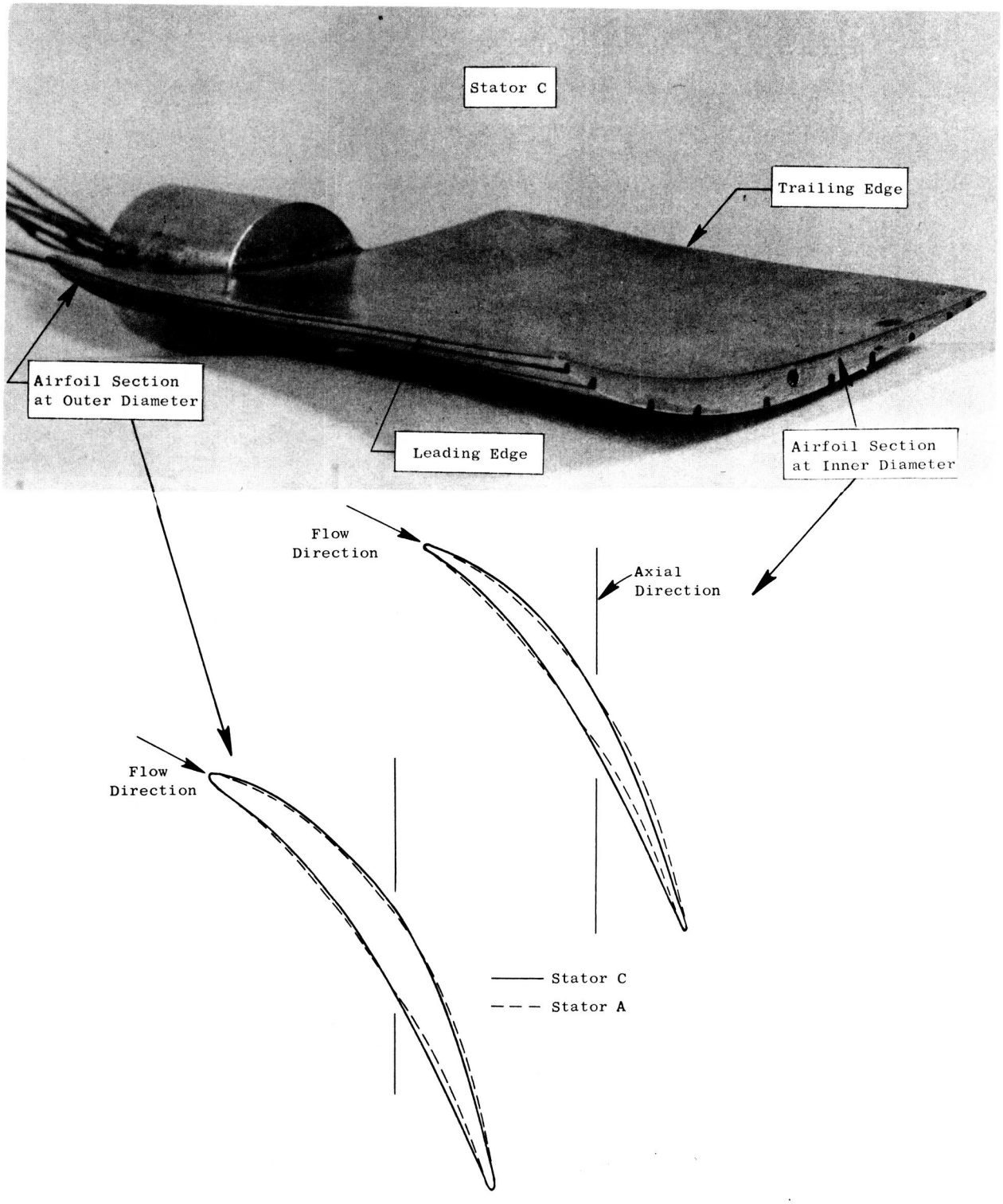

Figure 7. Comparison of the Stator C and Stator A Airfoil Sections.

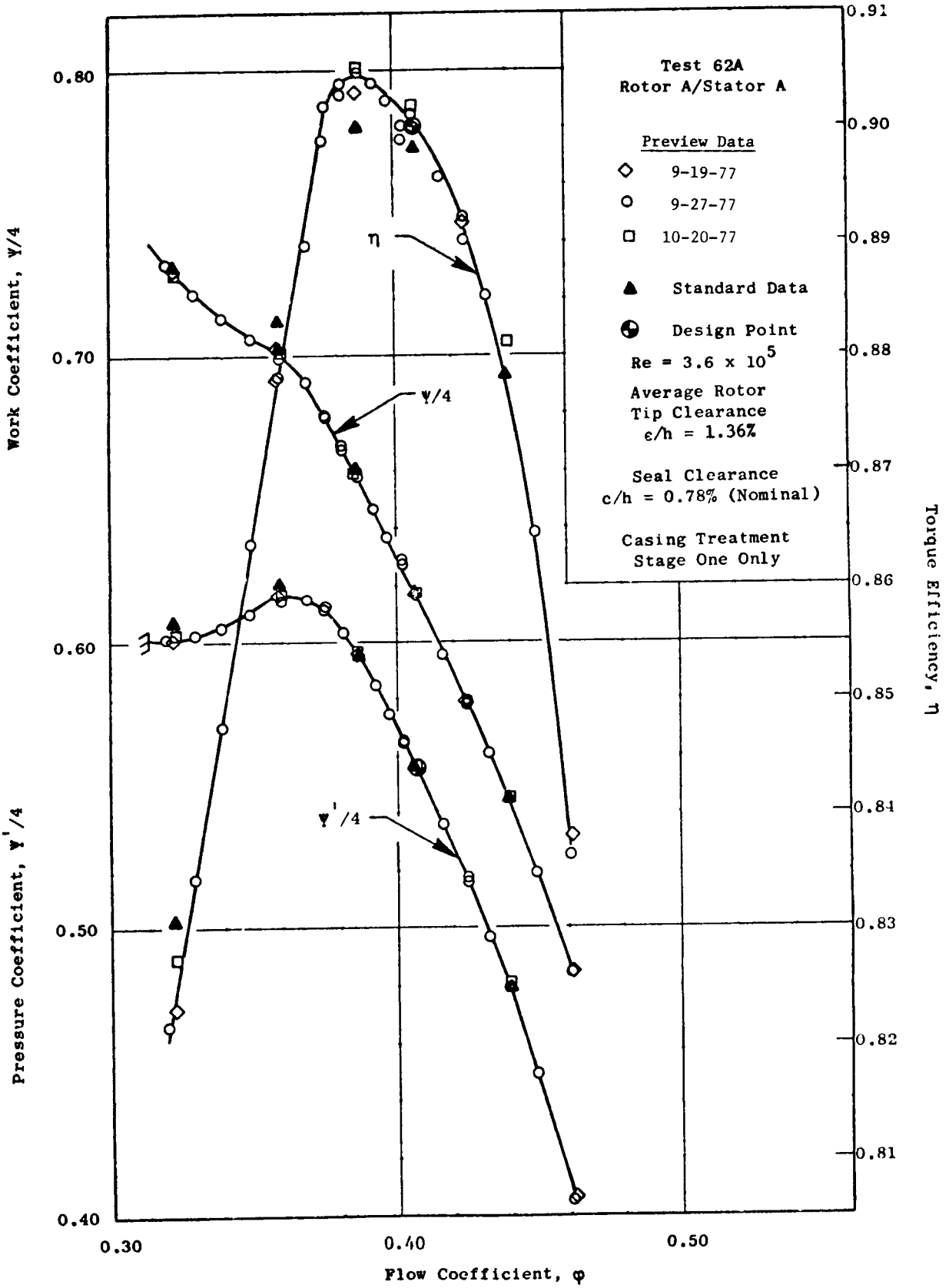

Figure 8. Overall Performance for the Four-Stage Baseline Configuration Using Rotor A/Stator A.

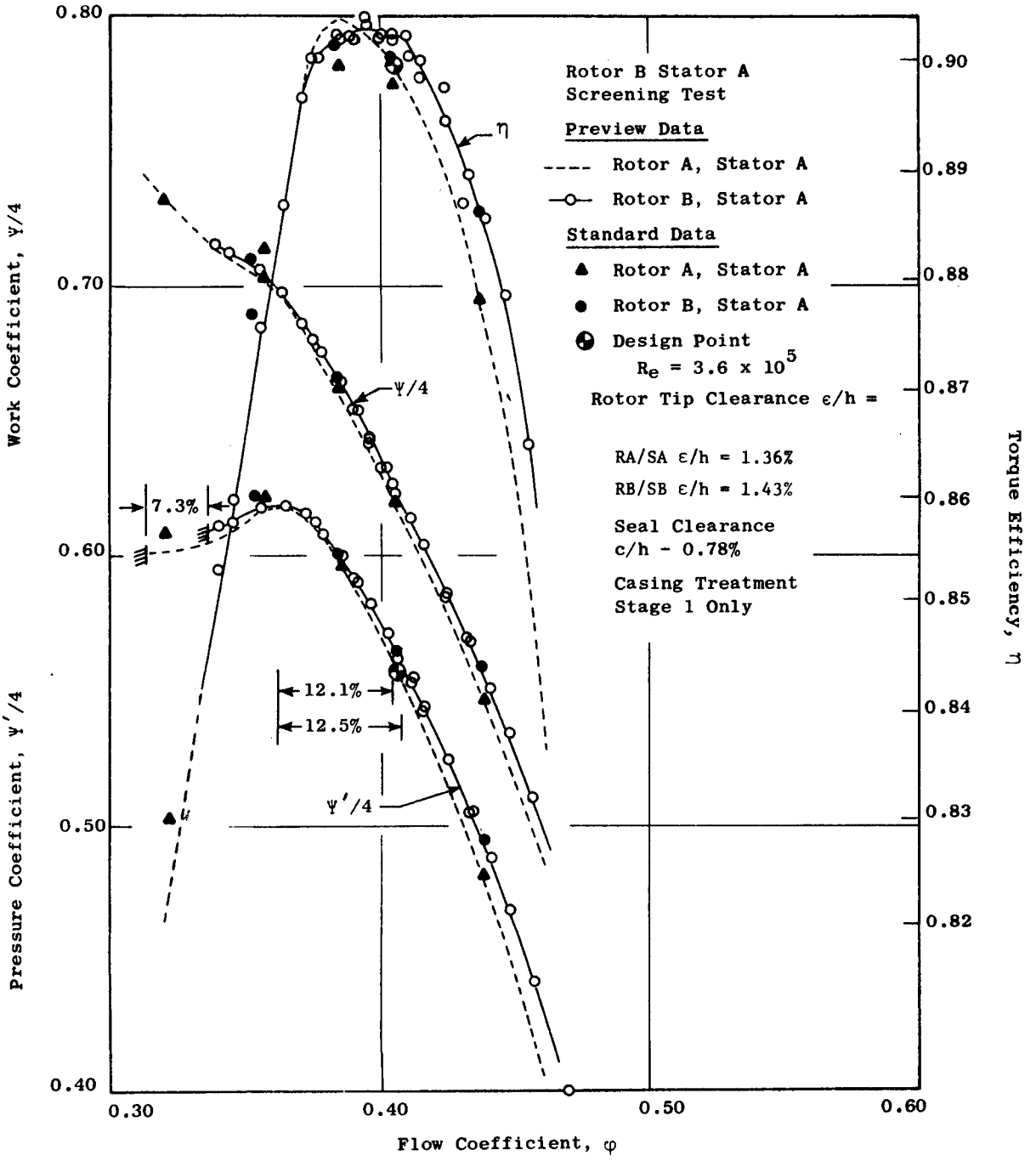

Figure 9. Comparison of the Overall Performance of Rotor B and Rotor A, Both Are Four-Stage Configurations Running with Stator A.

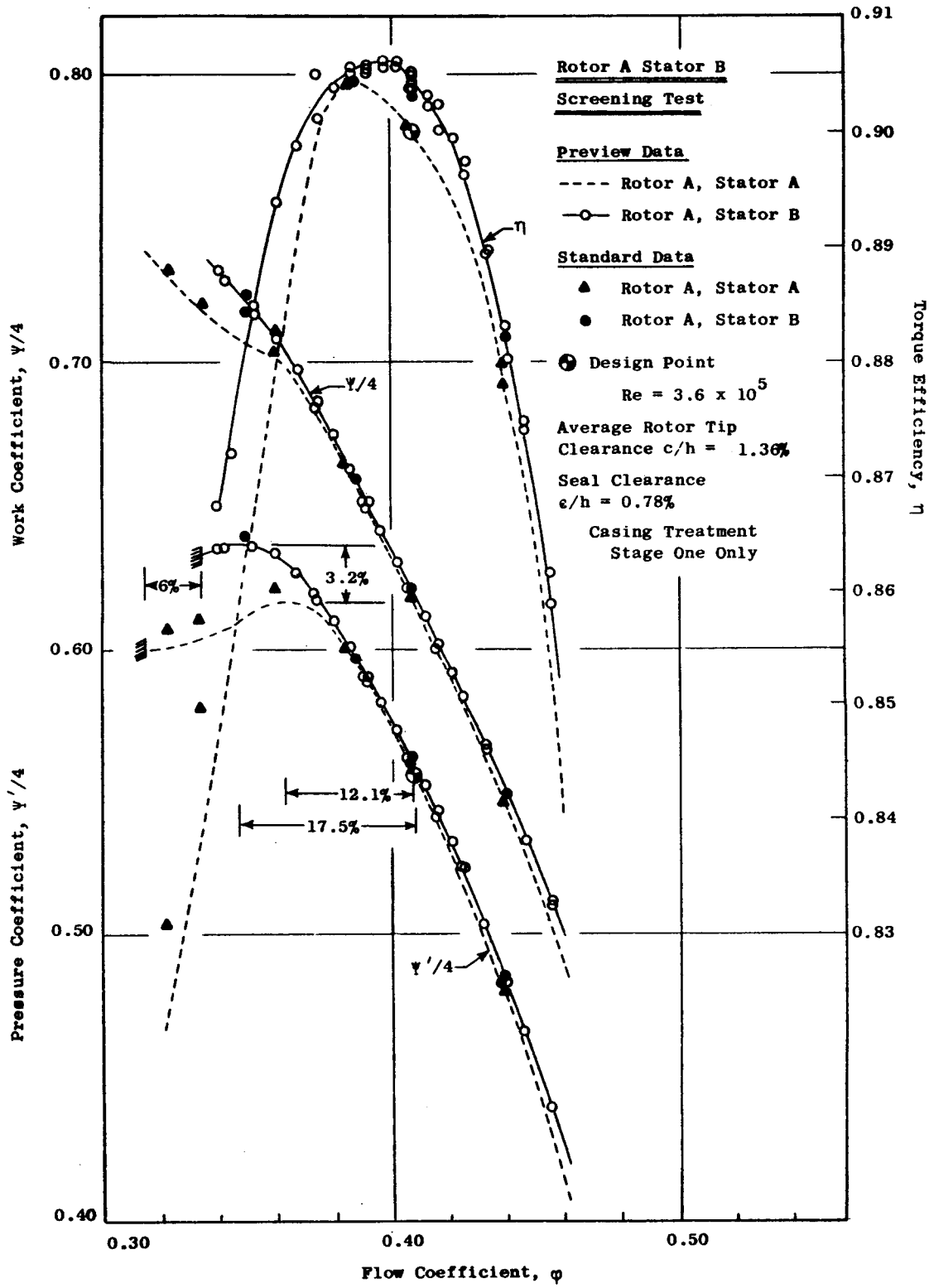

Figure 10. Comparison of the Performance of Stator B and Stator A, Both Are Four-Stage Configurations Running with Rotor A.

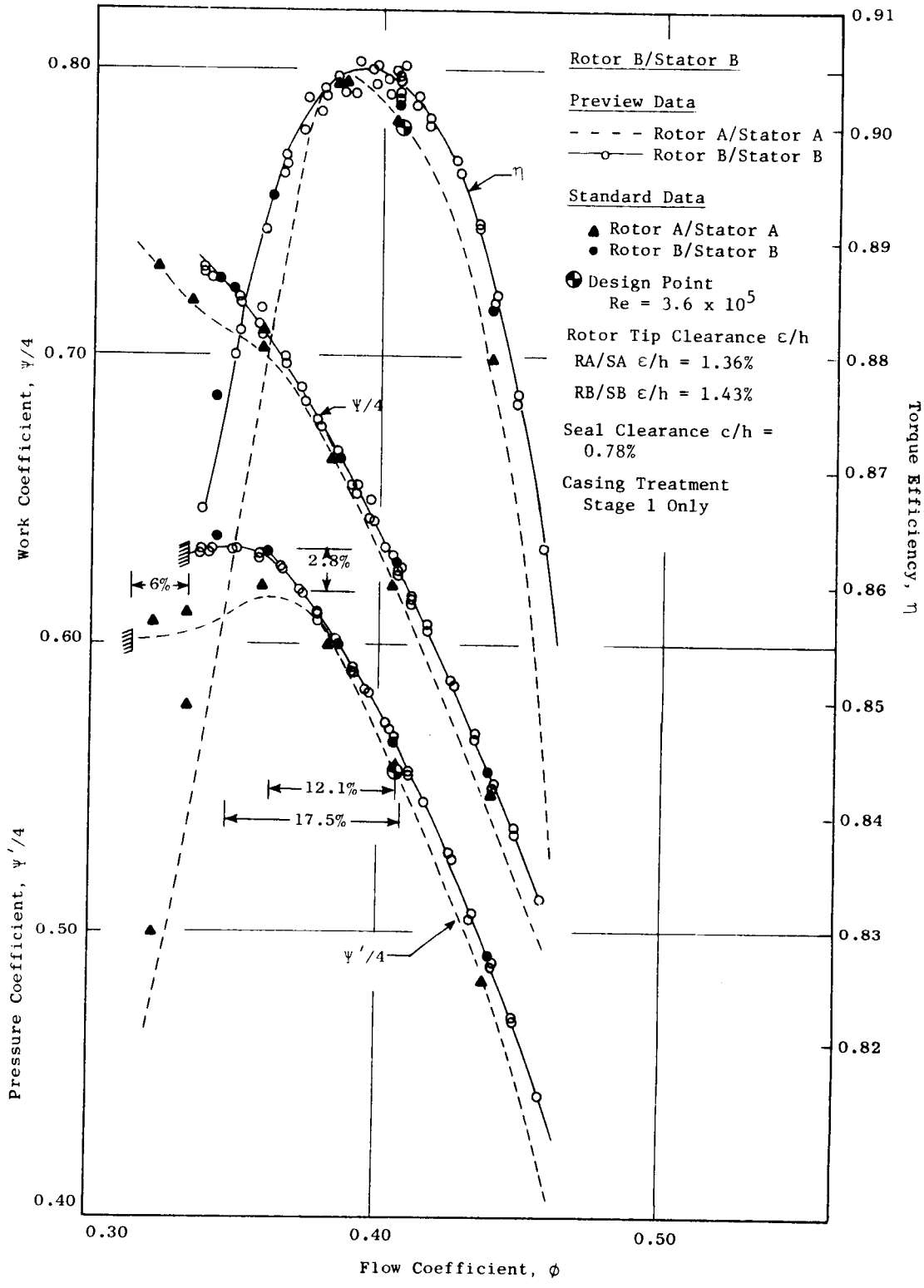

Figure 11. Comparison of the Performance of Rotor B/Stator B with Rotor A/Stator A, Both Are Four-Stage Configurations.

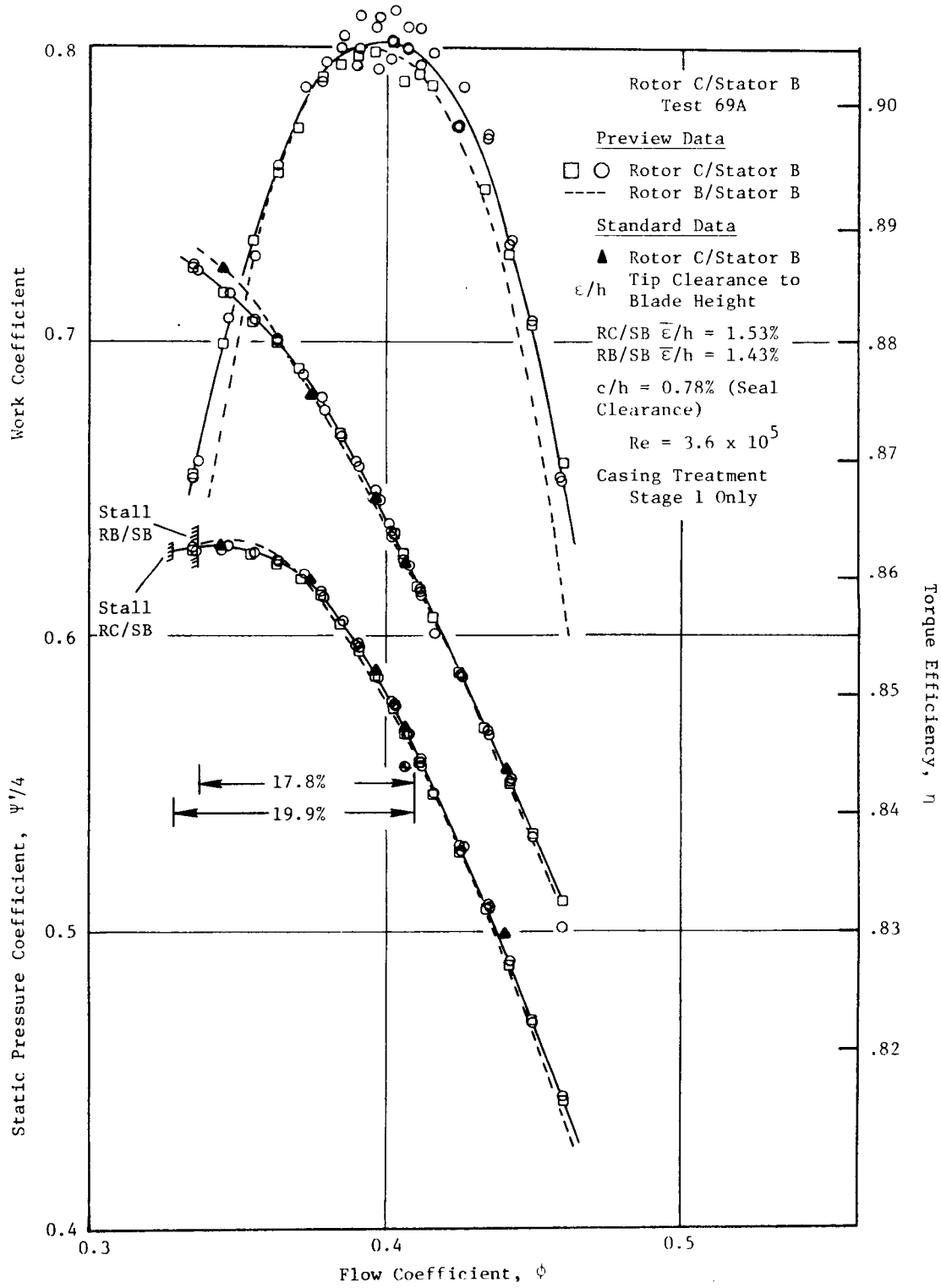

Figure 12. Comparison of the Performance of Rotor C and Rotor B, Both are Four-Stage Configurations Running with Stator B.

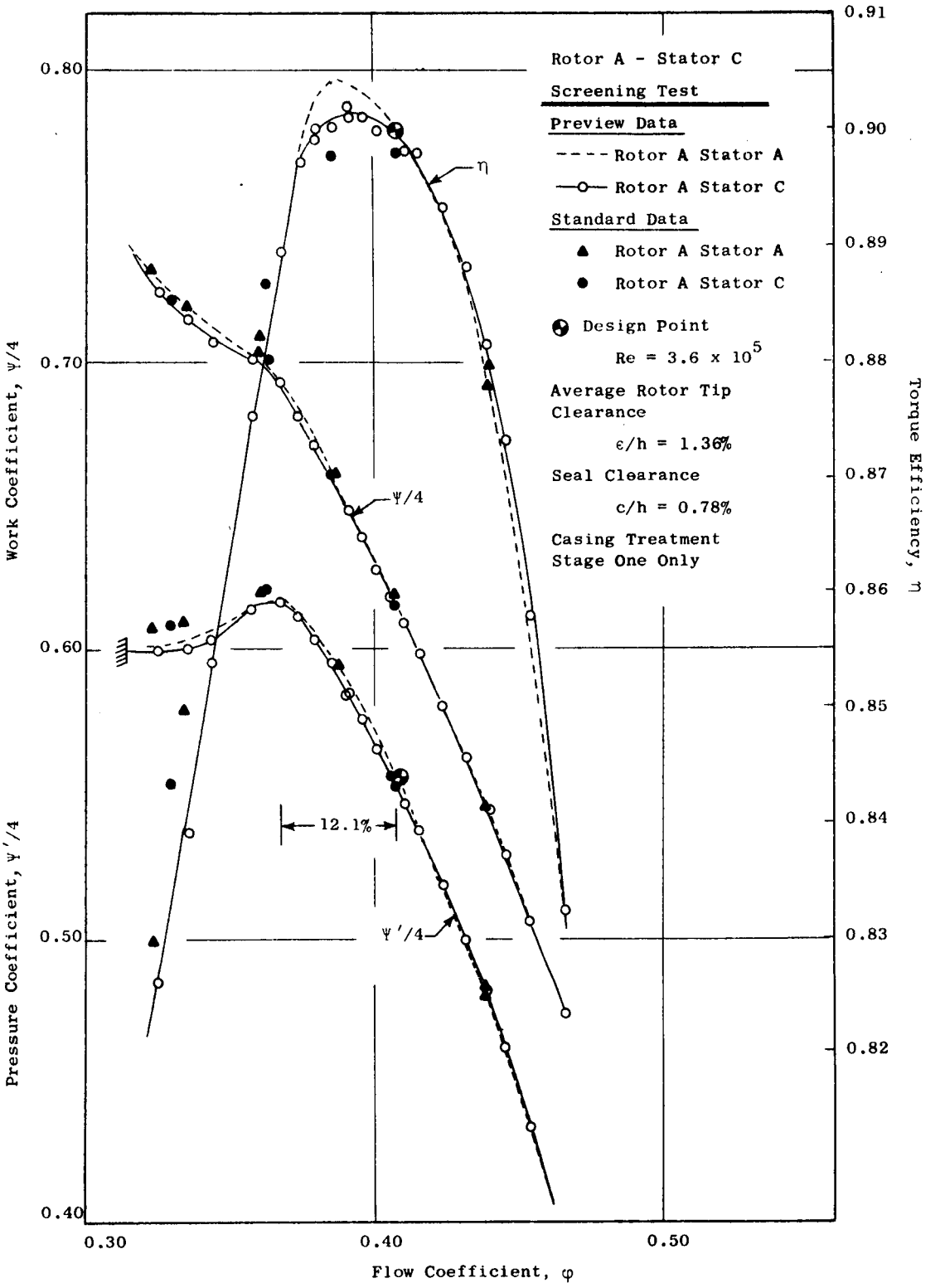

Figure 13. Comparison of the Performance of Stator C with Stator A, Both Are Four-Stage Configurations Running with Rotor A.

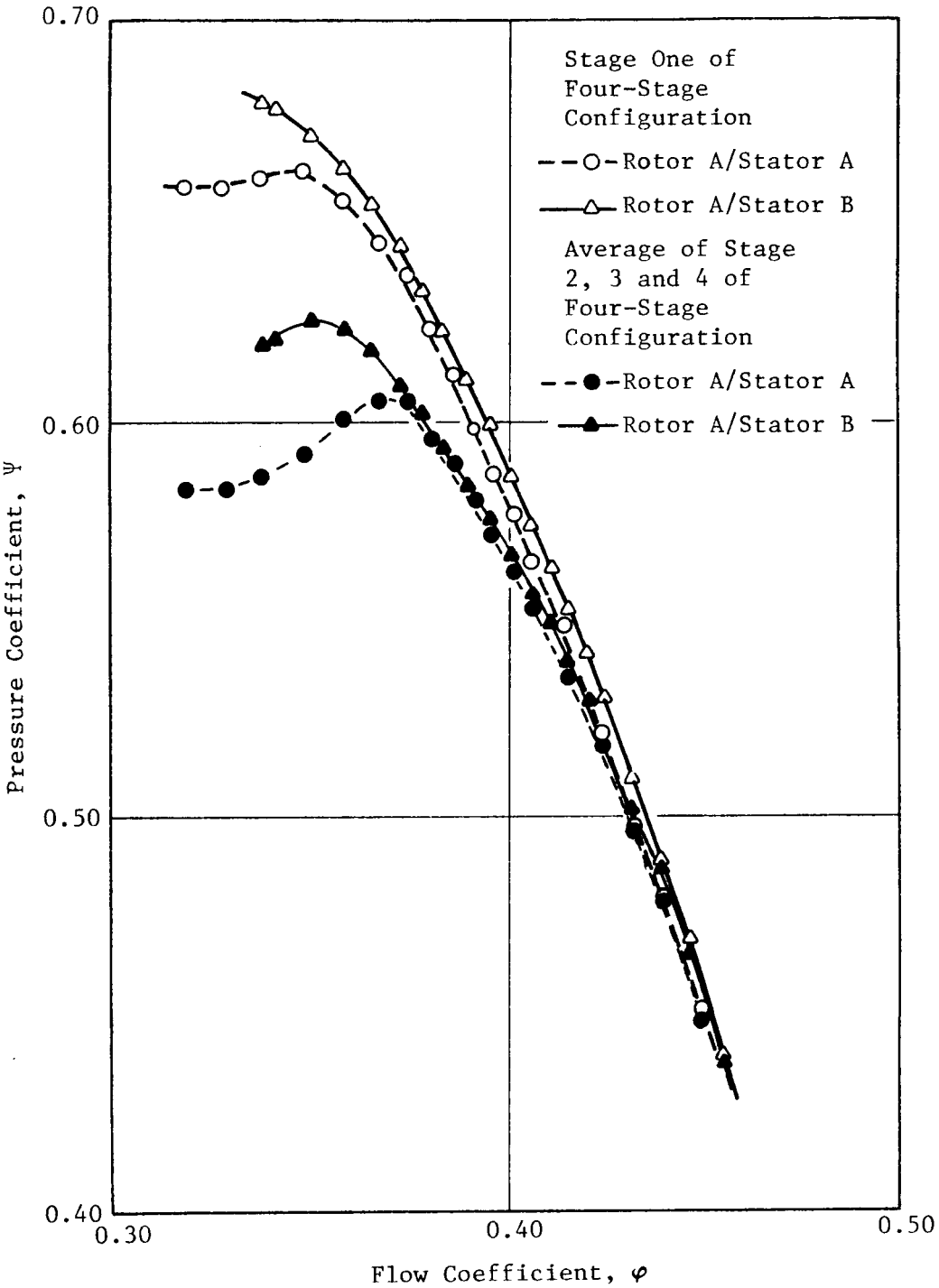

Figure 14. Comparison of the Performance of Stage 1 of the Four-Stage Configuration for Rotor A/Stator A and Rotor A/Stator B.

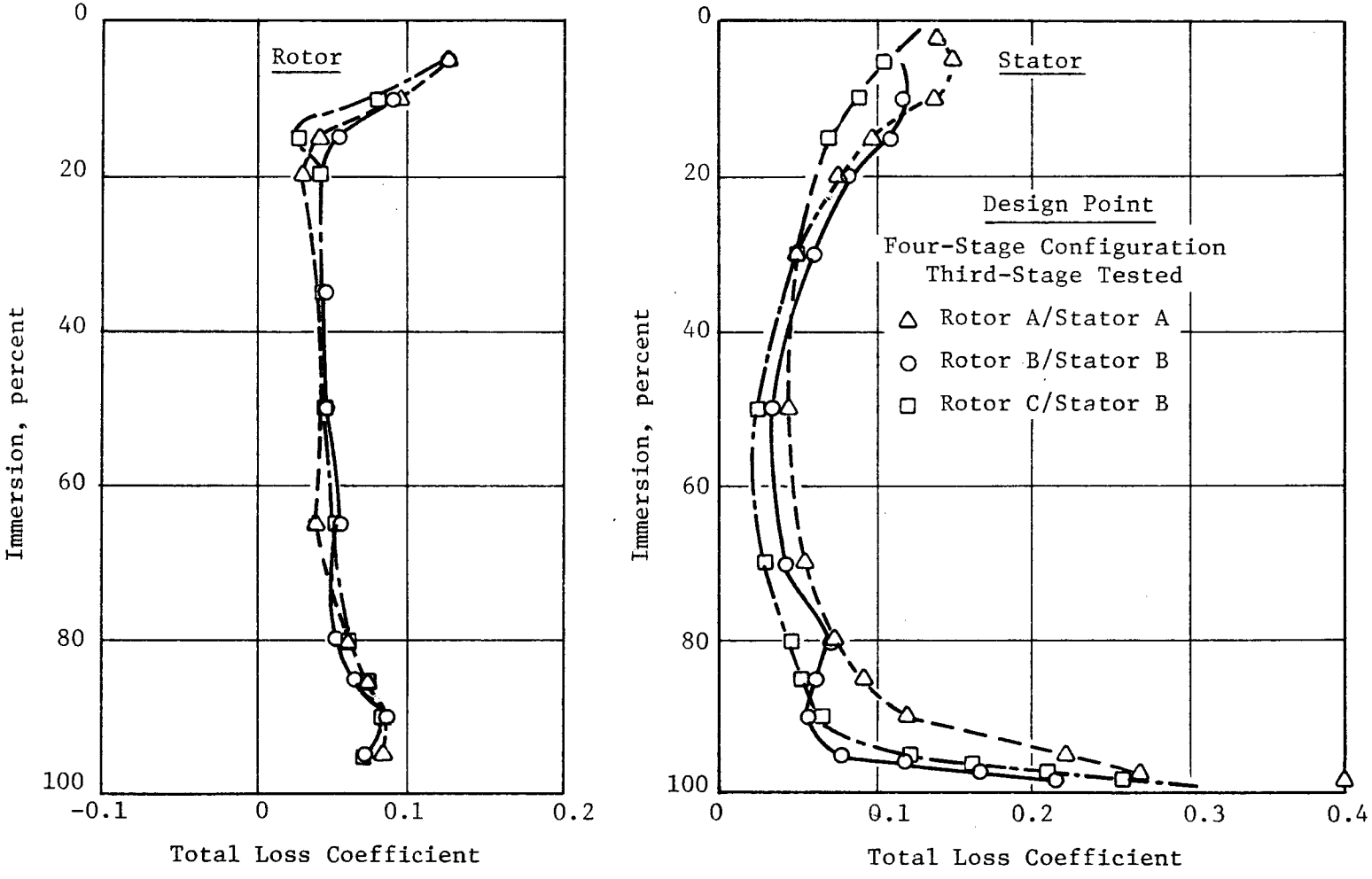

Figure 15. Comparison of the Radial Variation of Total Loss Coefficient, Four-Stage Configuration, Third Stage Tested.

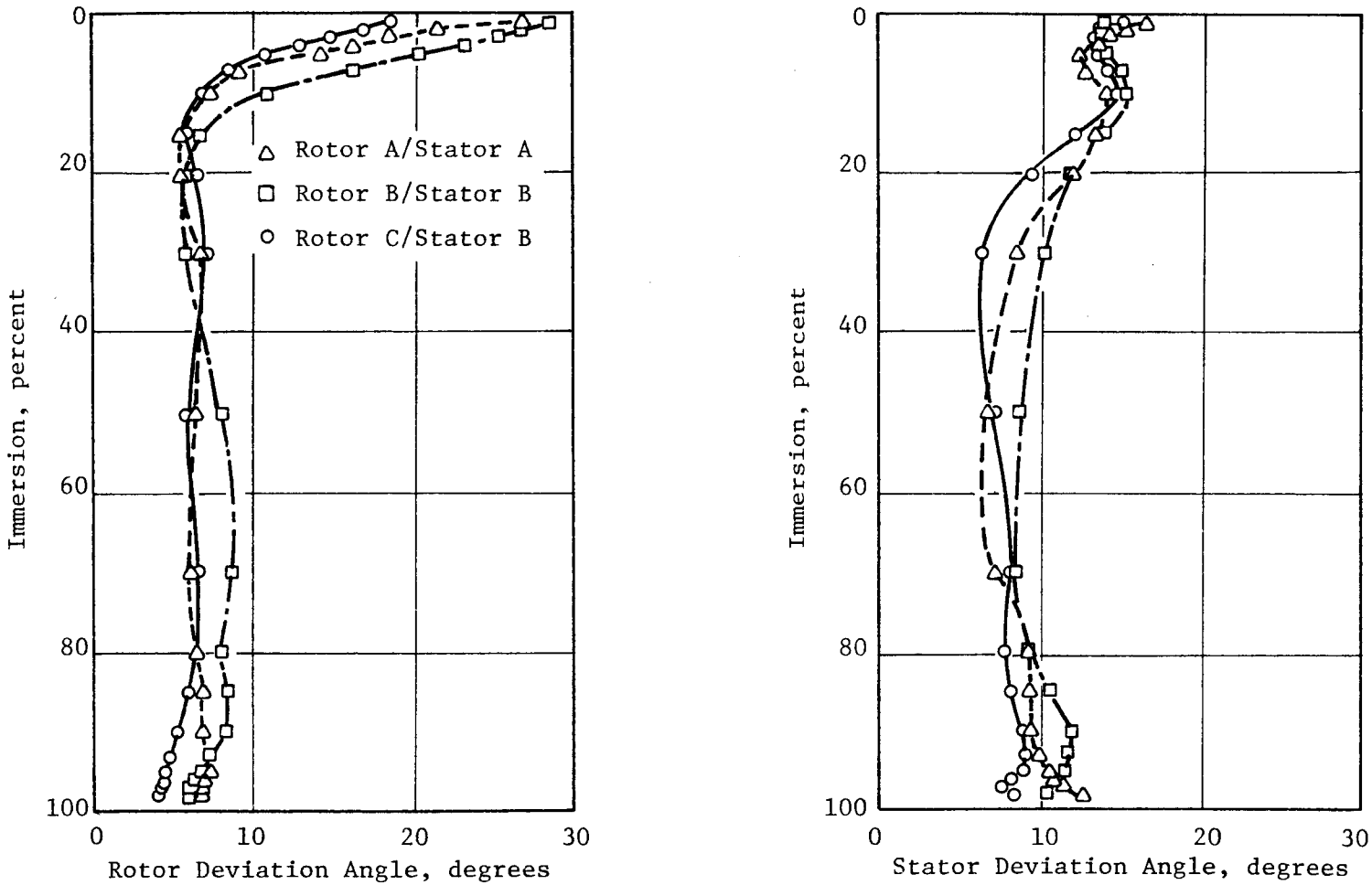

Figure 16. Comparison of the Radial Variation of Deviation Angle, Four-Stage Configuration, Third Stage Tested.

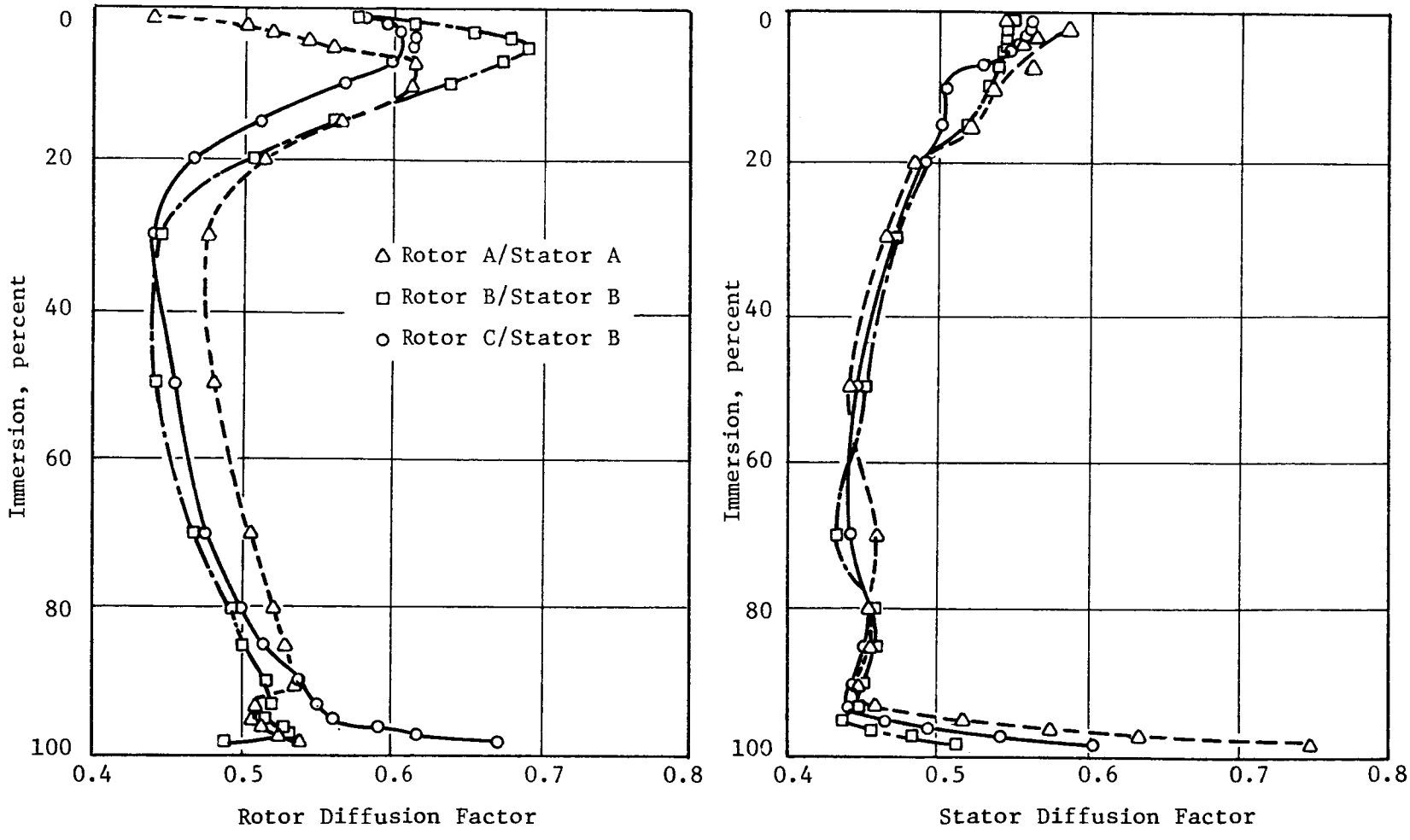

Figure 17. Comparison of the Radial Variation of Diffusion Factor, Four-Stage Configuration, Third Stage Tested.

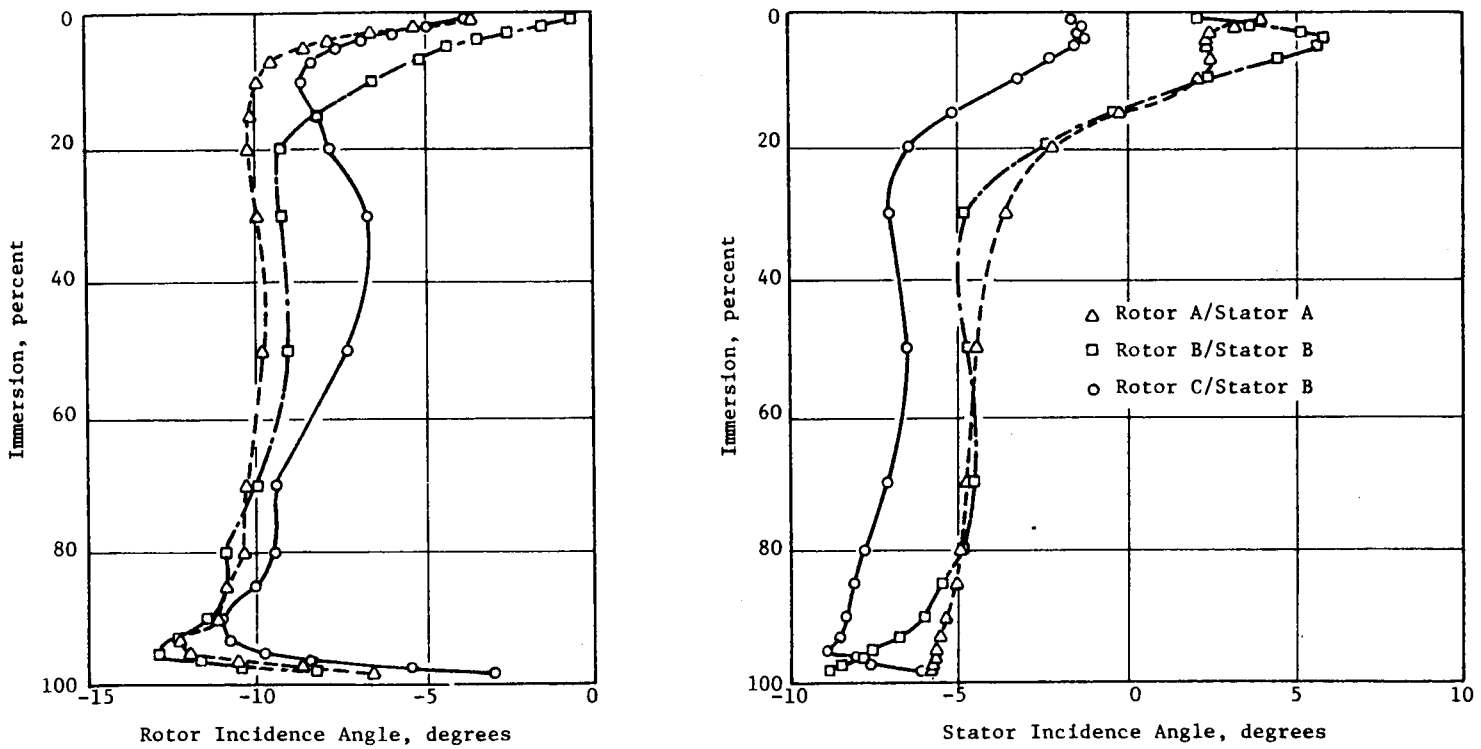

Figure 18. Comparison of the Radial Variation of Incidence Angle, Four-Stage Configuration, Third Stage Tested.

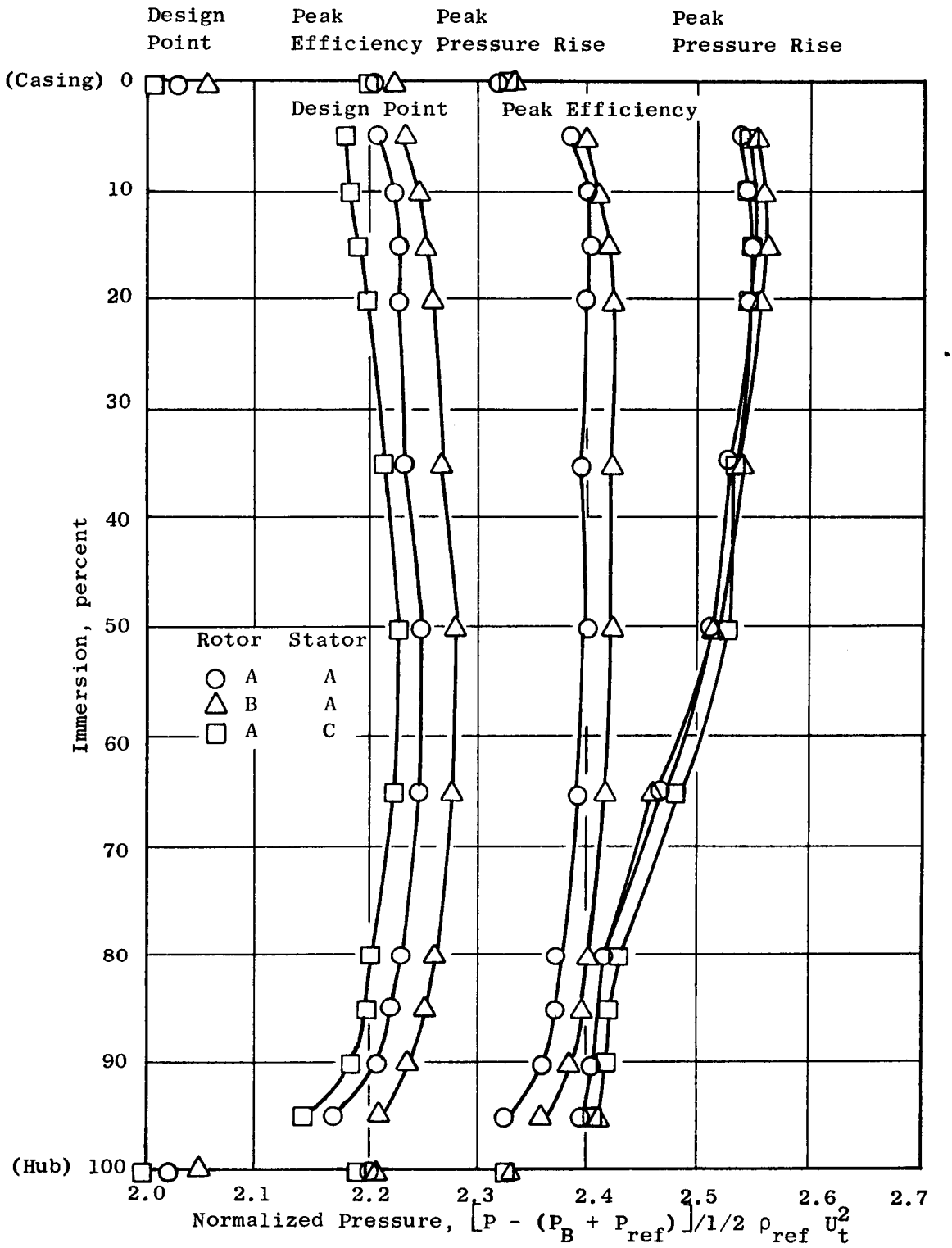

Figure 19. Radial Variations of Normalized Total Pressure for the Blade Shapes Used in the Test Program, Four-Stage Configuration.

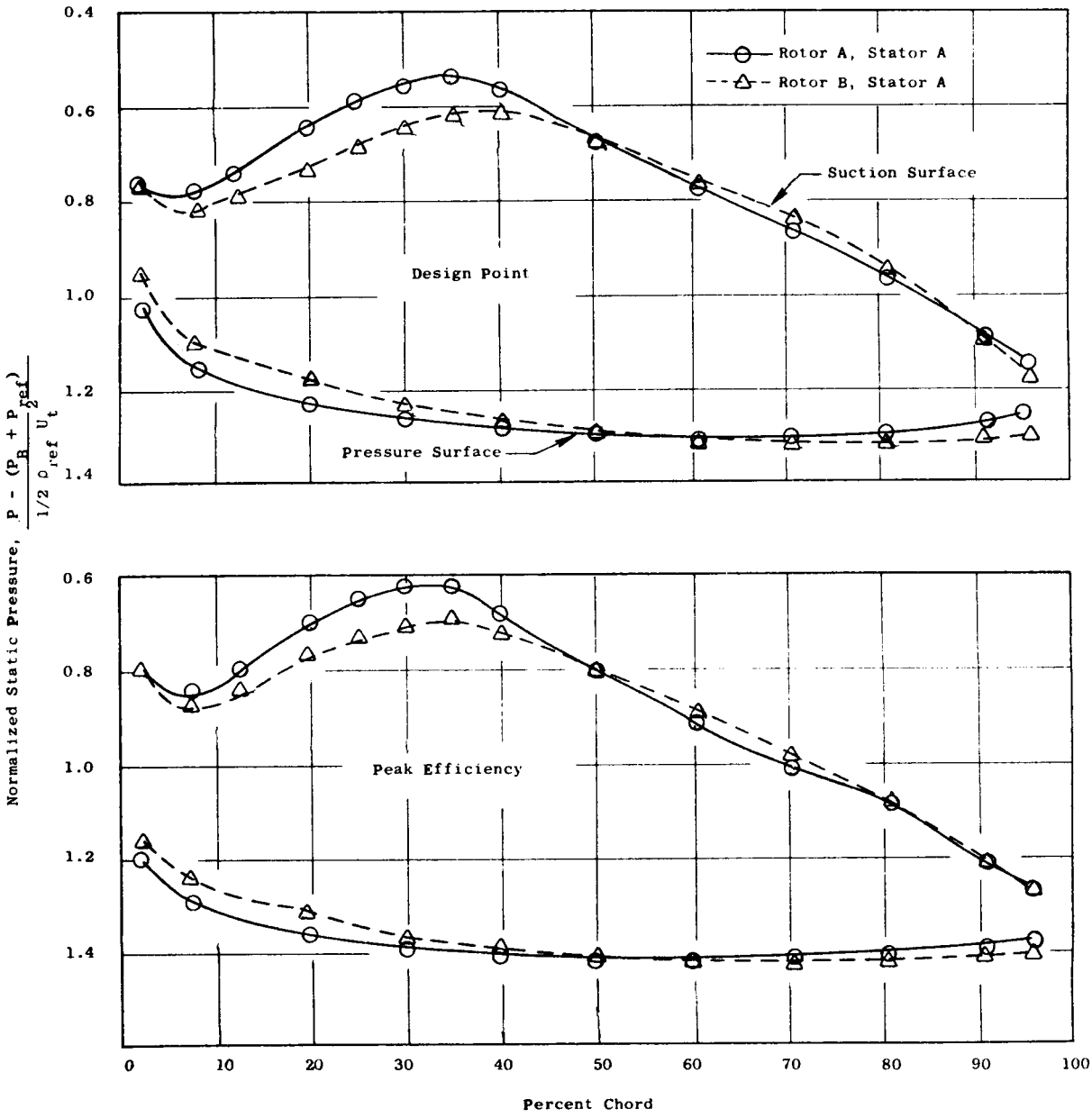

Figure 20. Comparison of Rotor B and Rotor A Surface Static Pressures Near the Tip of the Rotor Four-Stage Configuration, Third Stage Tested.

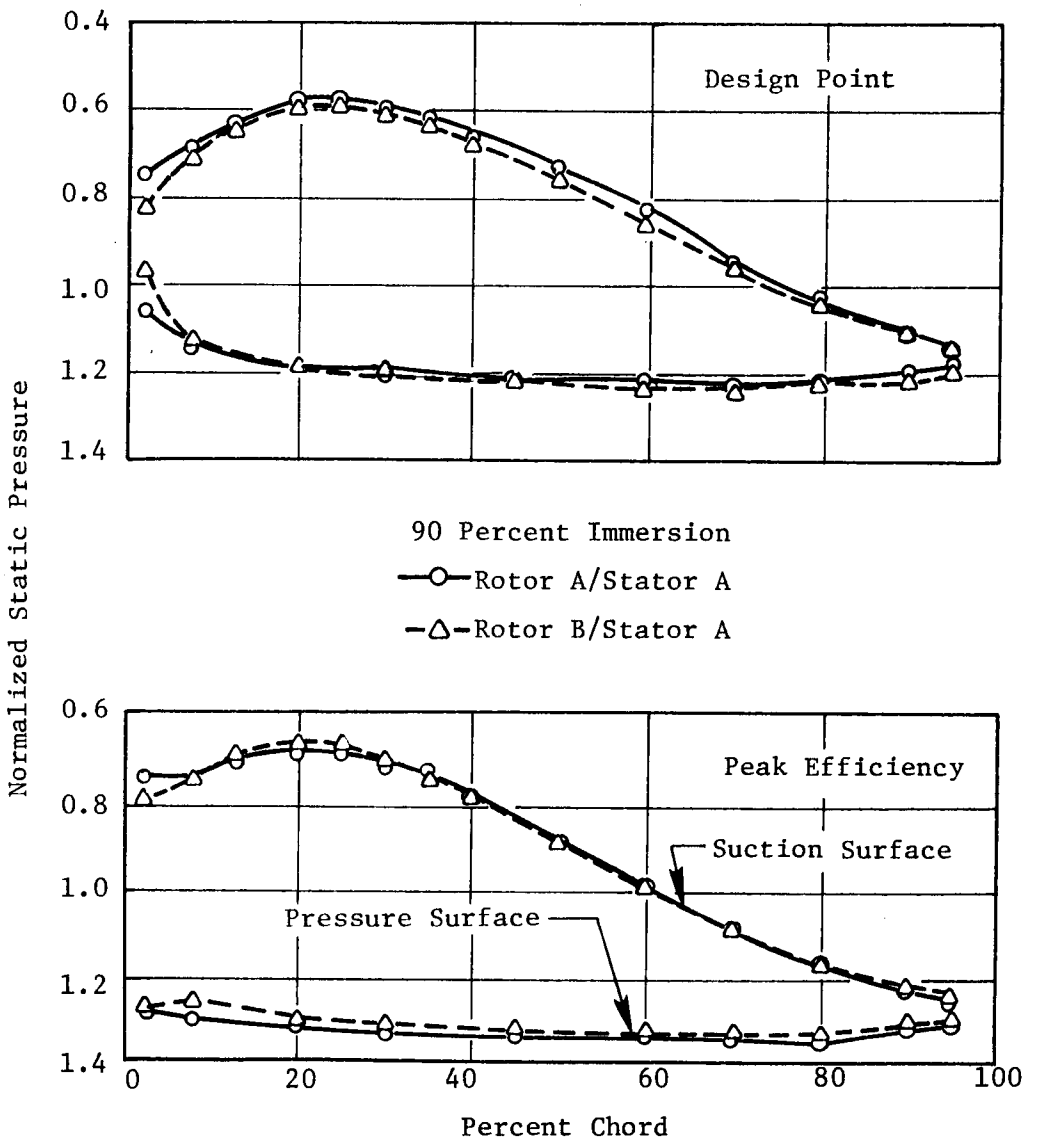

Figure 21. Comparison of Rotor B and Rotor A Surface Static Pressures Near the Hub of the Rotor, Four-Stage Configuration, Third Stage Tested.

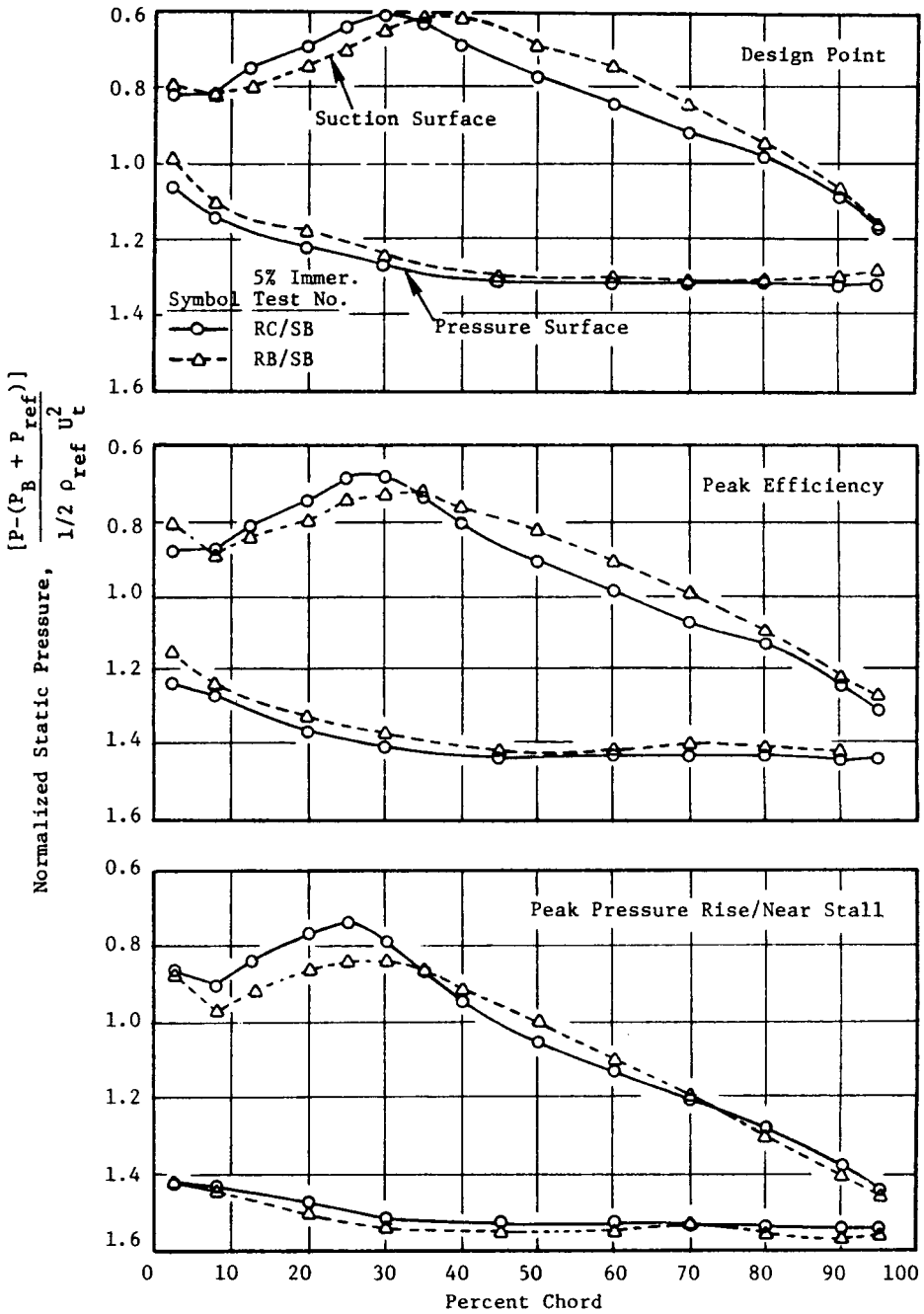

Figure 22. Comparison of Rotor C and Rotor B Surface Static Pressures Near the Tip of the Rotor, Four-Stage Configuration, Third Stage Tested.

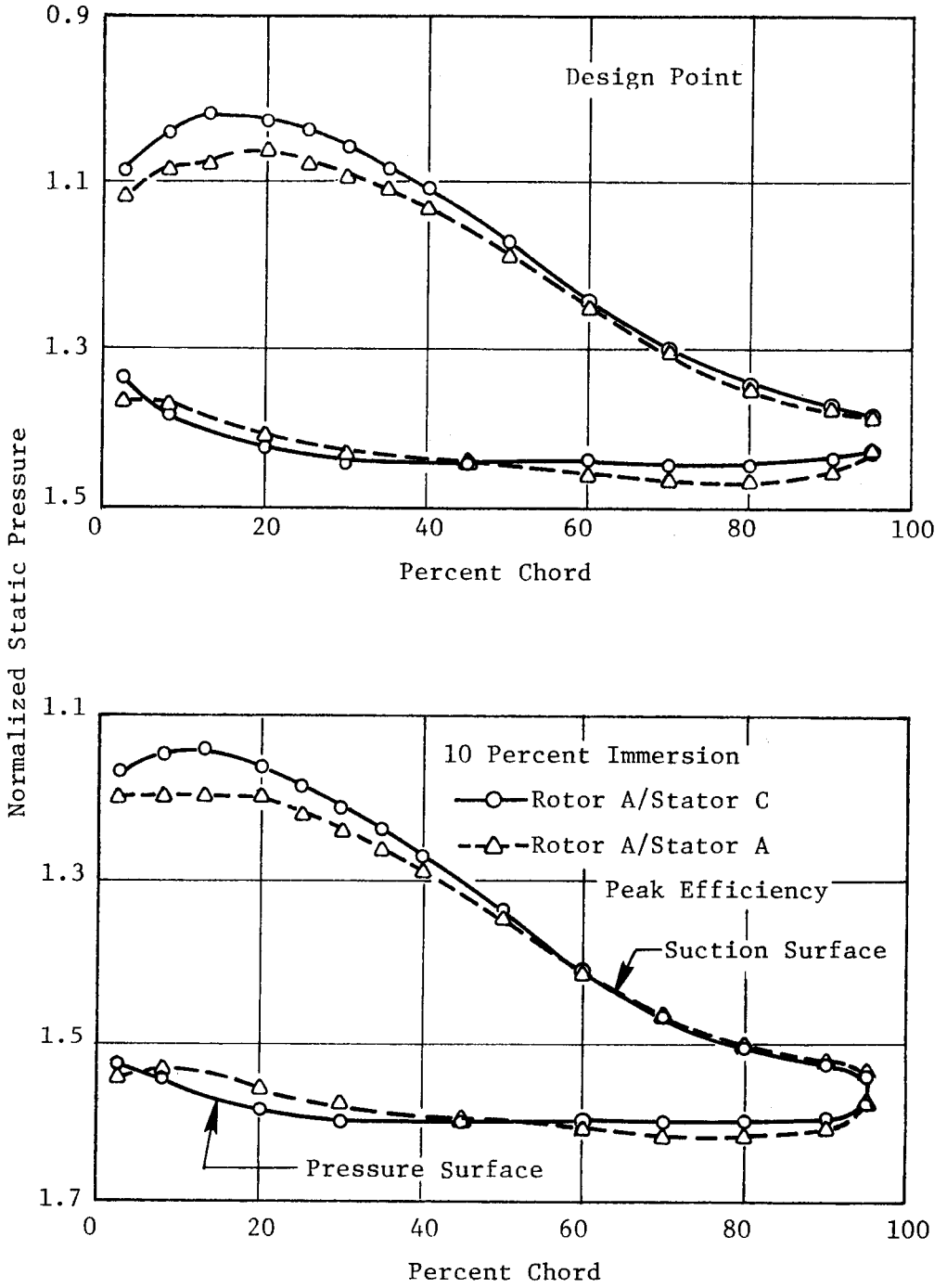

Figure 23. Comparison of Stator C and Stator A Surface Static Pressures at 10% Immersion, Four-Stage Configuration, Third Stage Tested.

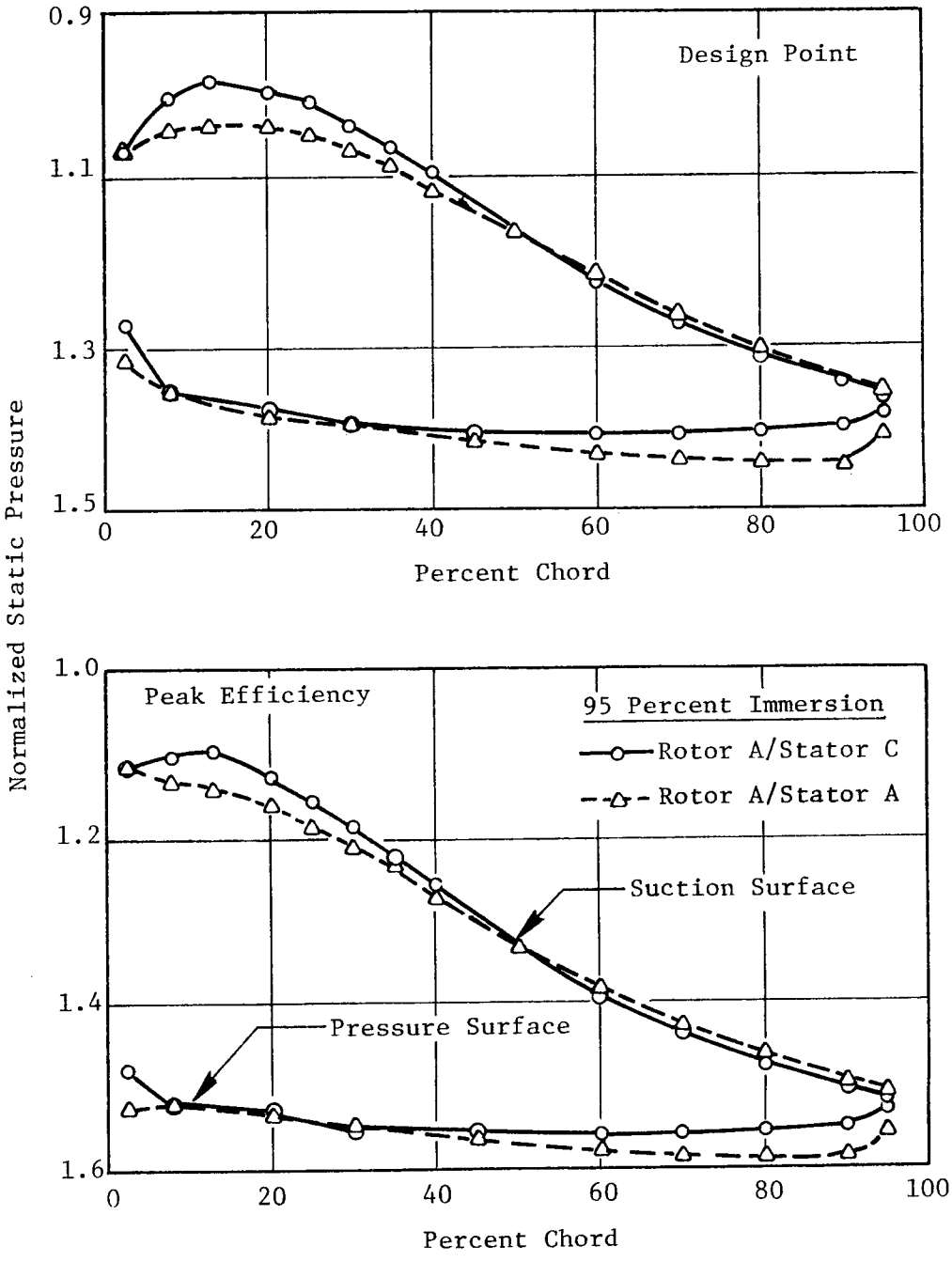

Figure 24. Comparison of Stator C and Stator A Surface Static Pressures at 95% Immersion, Four-Stage Configuration, Third Stage Tested.

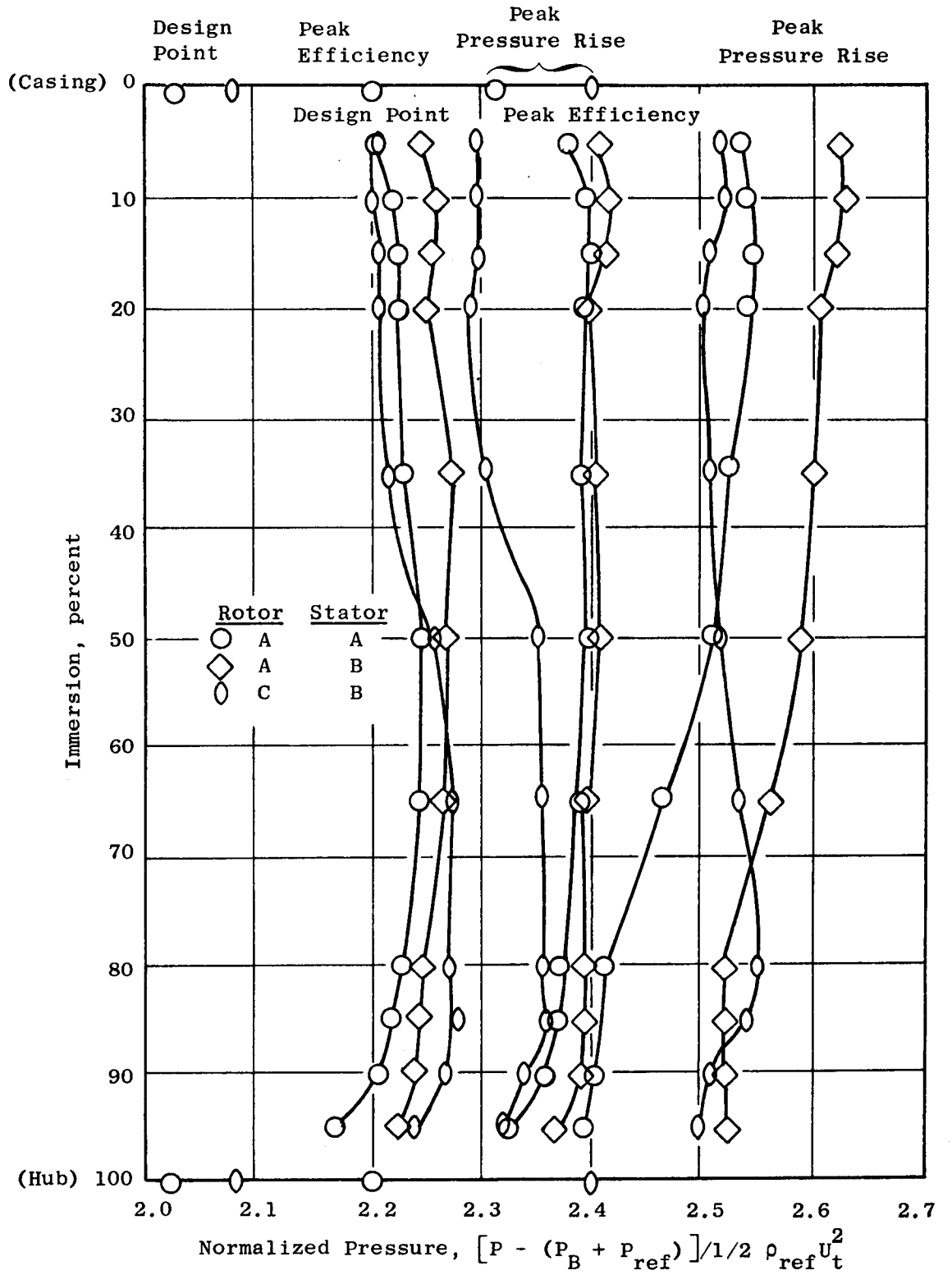

Figure 25. Radial Variation of Normalized Total Pressures at the Compressor Discharge for the Vector Diagram Types Used in the Test Program, Four-Stage Configuration.

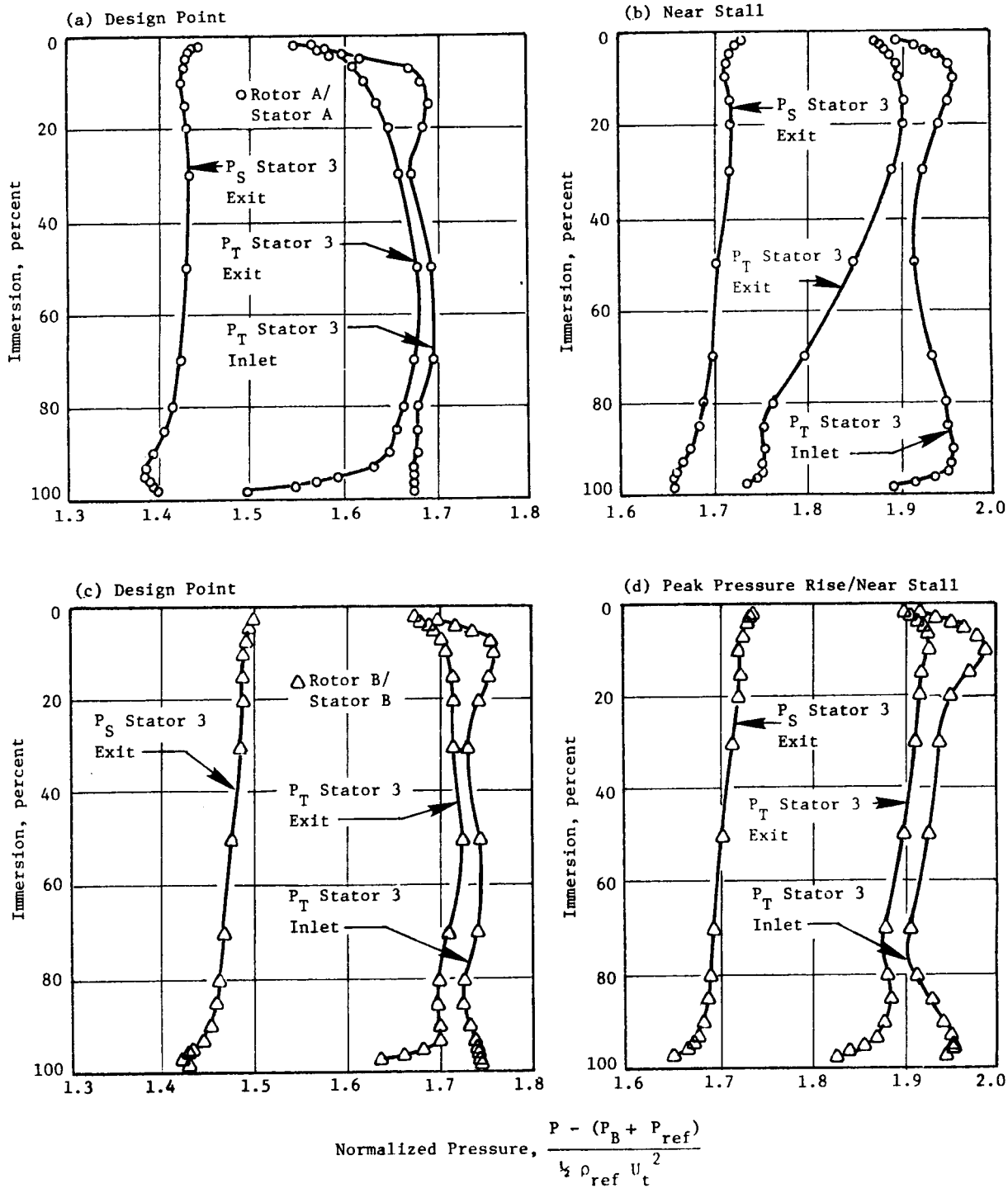

Figure 26. Comparison of the Radial Variation of Absolute Total Pressure for Rotor B/Stator B and Rotor A/Stator A, Four-Stage Configuration, Third Stage Tested.

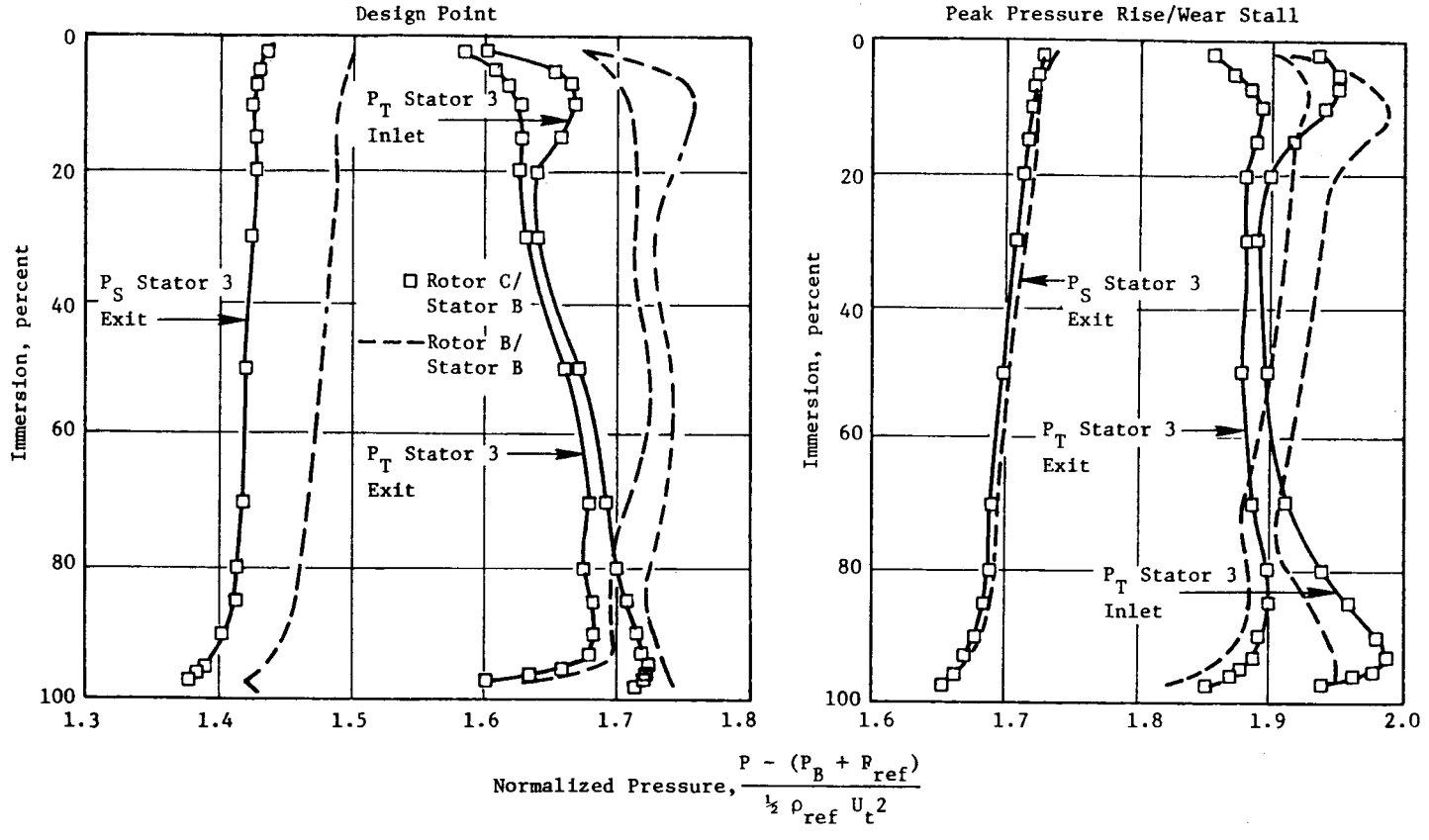

Figure 27. Comparison of the Radial Variation of Absolute Total Pressure for Rotor C/Stator B and Rotor B/Stator B, Four-Stage Configuration, Third Stage Tested.

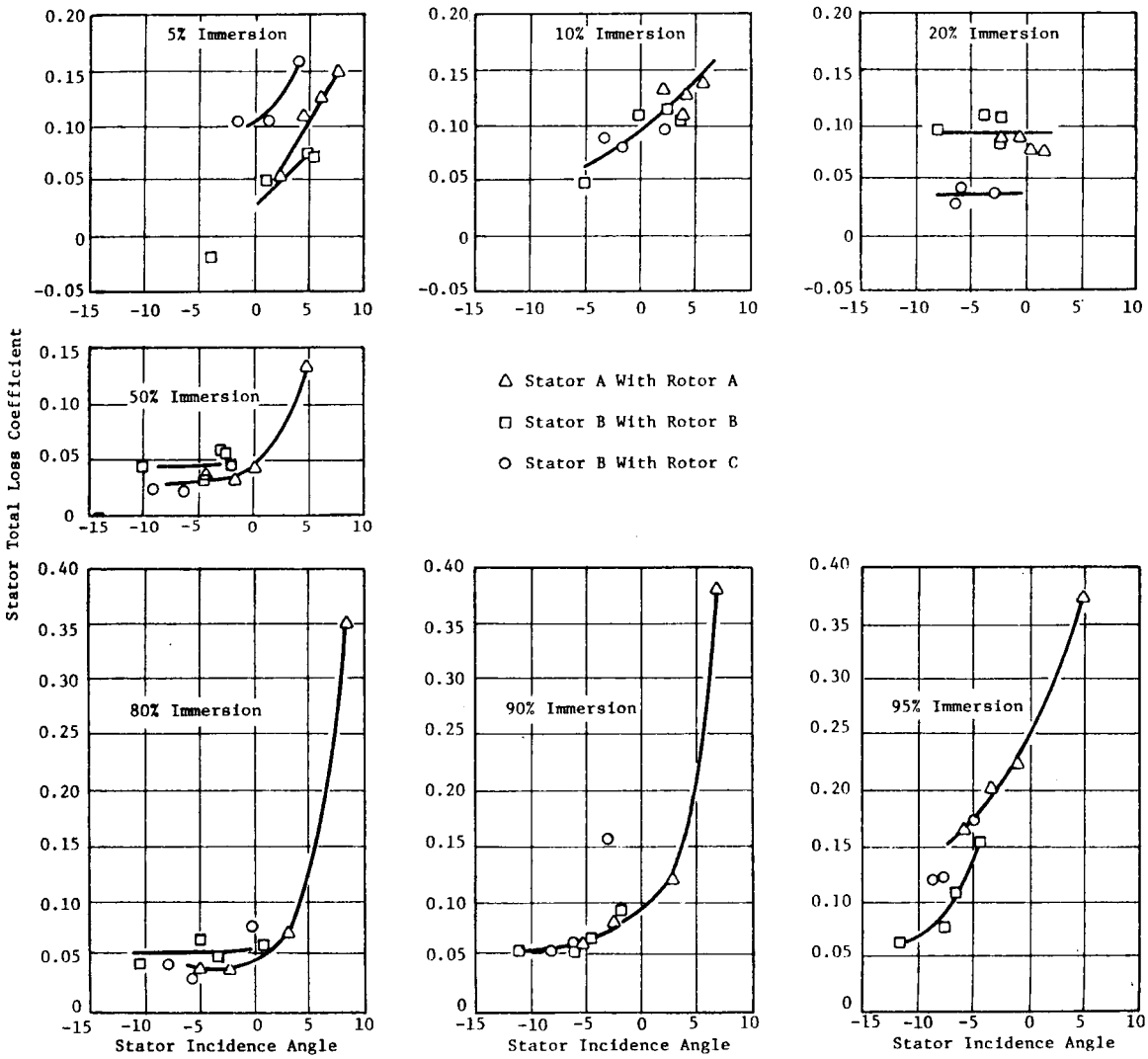

Figure 28. Stator Total Loss Coefficient Versus Incidence Angle, Four-Stage Configuration, Third Stage Tested.

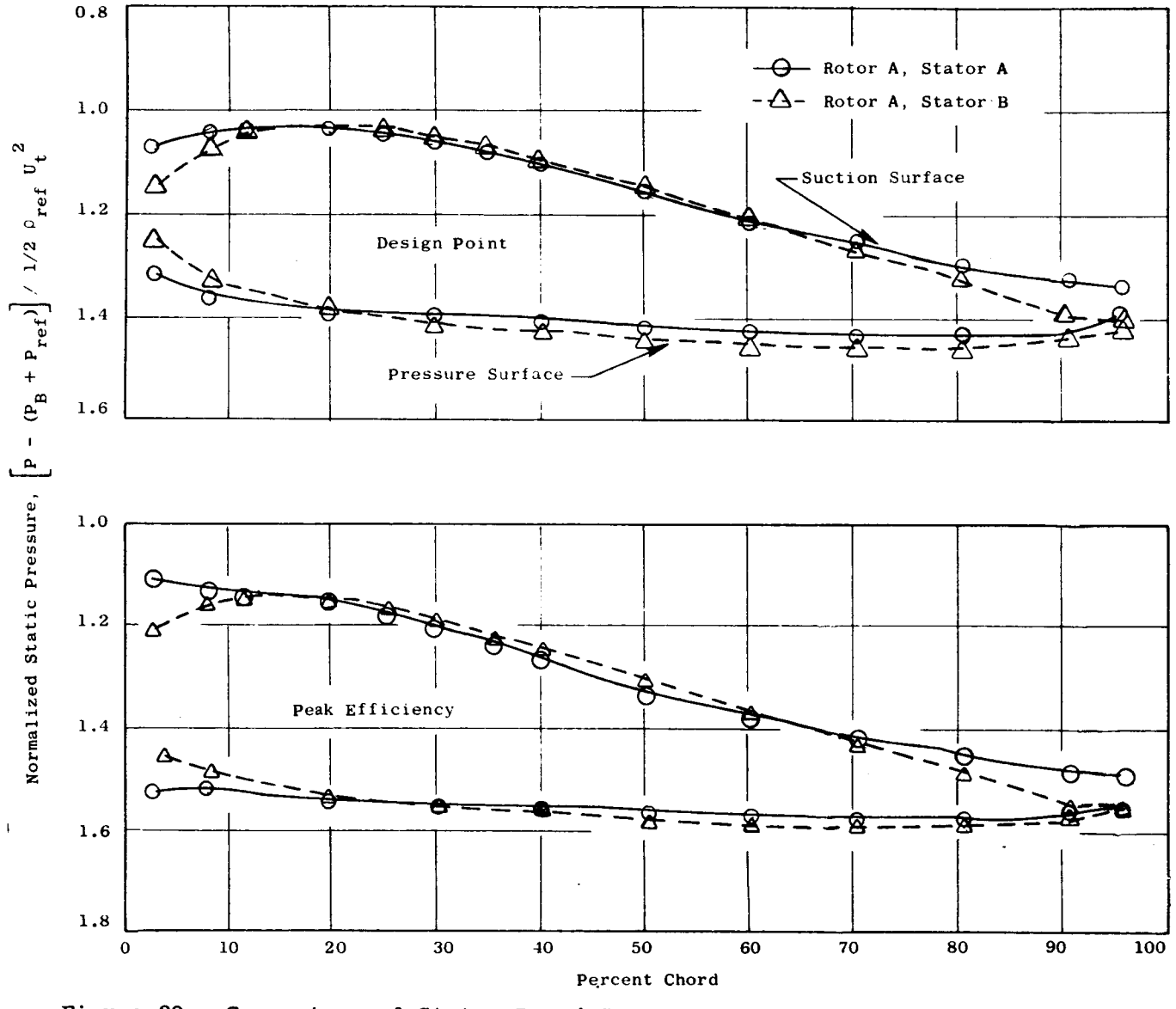

Figure 29. Comparison of Stator B and Stator A Surface Static Pressures at 95 Percent Immersion, Four-Stage Configuration, Third Stage Tested.

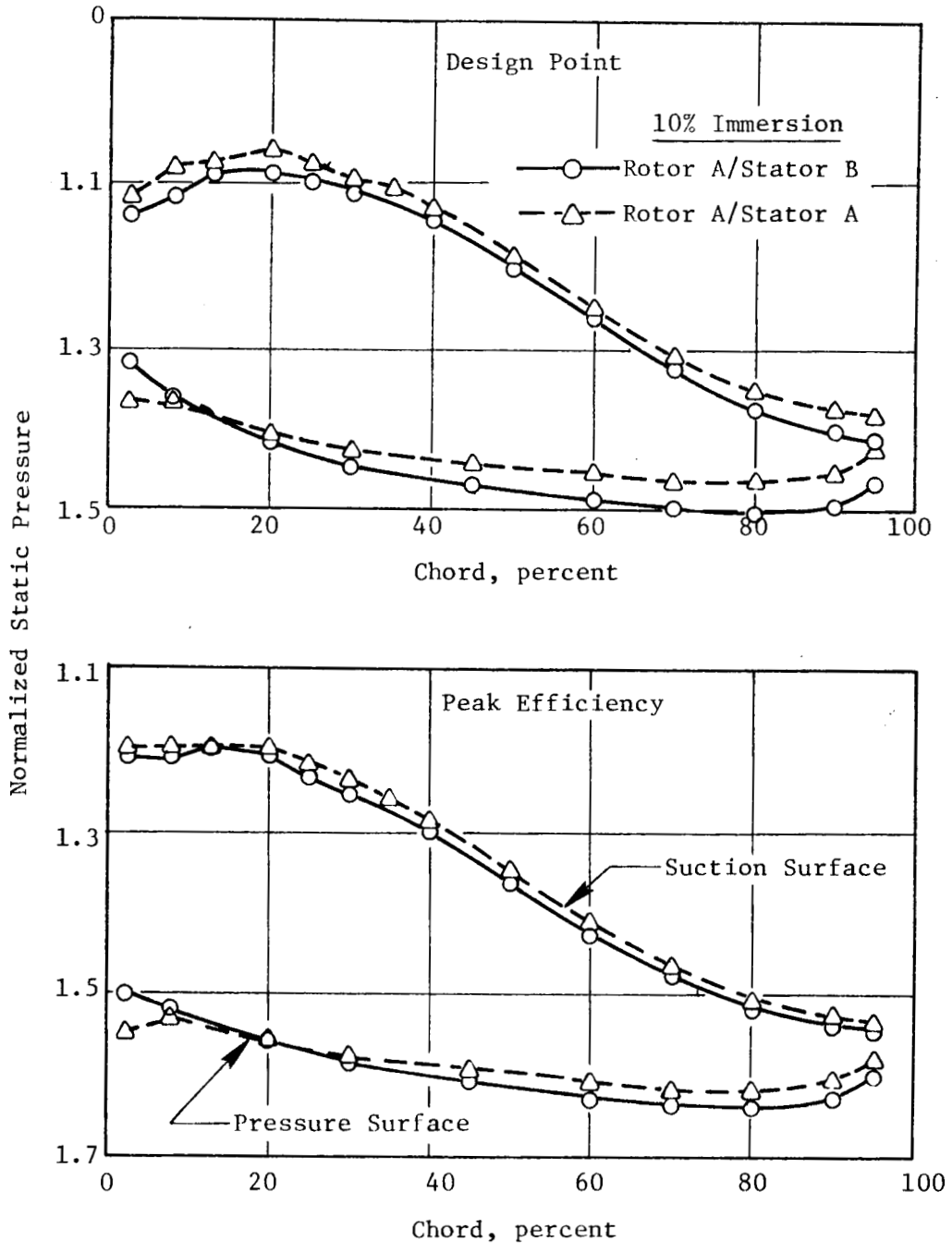

Figure 30. Comparison of Stator B and Stator A Surface Static Pressures at 10% Immersion, Four-Stage Configuration, Third Stage Tested.

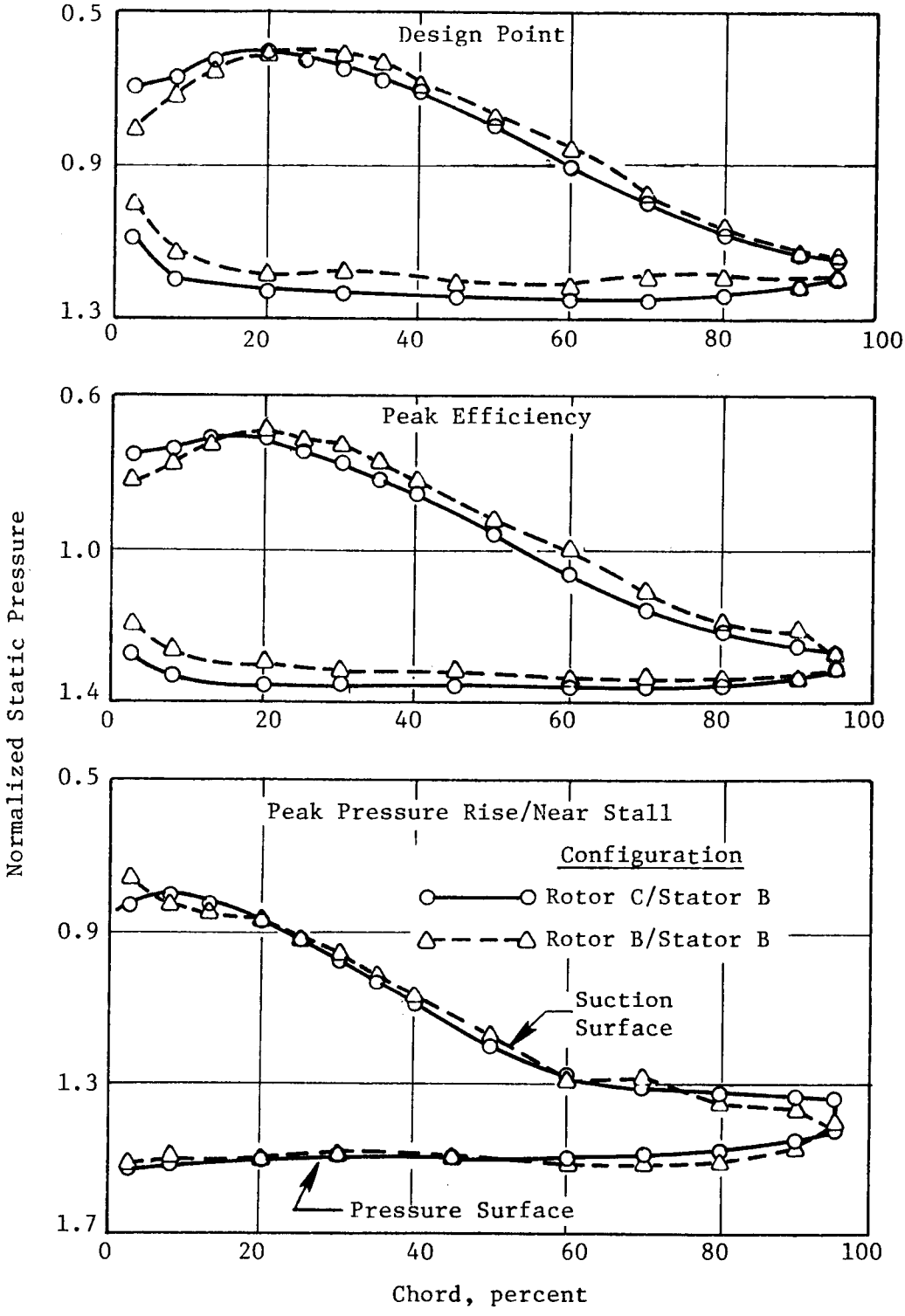

Figure 31. Comparison of Rotor C and Rotor B Surface Static Pressures Near the Hub of the Rotor, Four-Stage Configuration, Third Stage Tested.

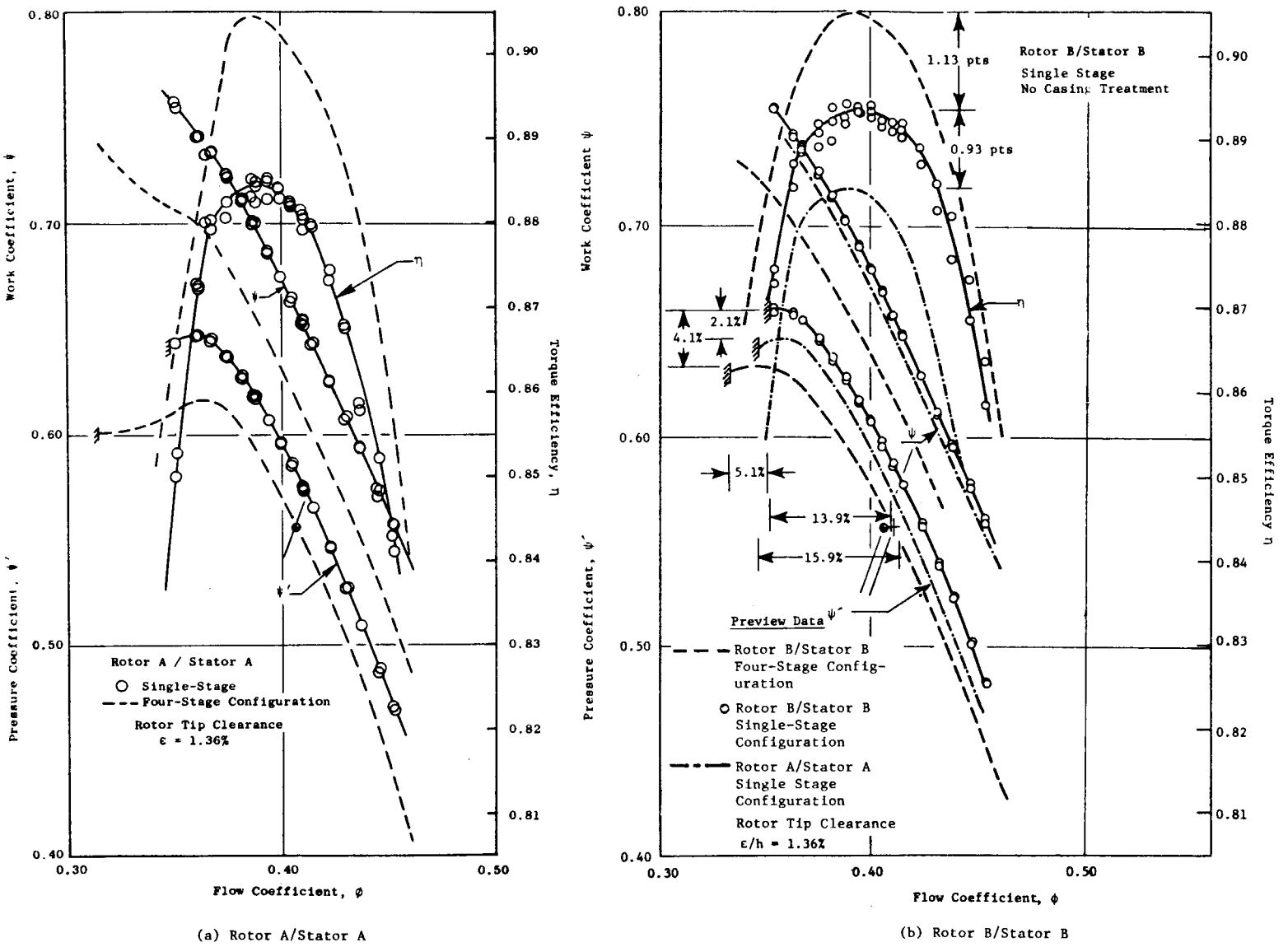

Figure 32. Overall Performance of the Single-Stage Configuration Compared to That of the Four-Stage Configuration.

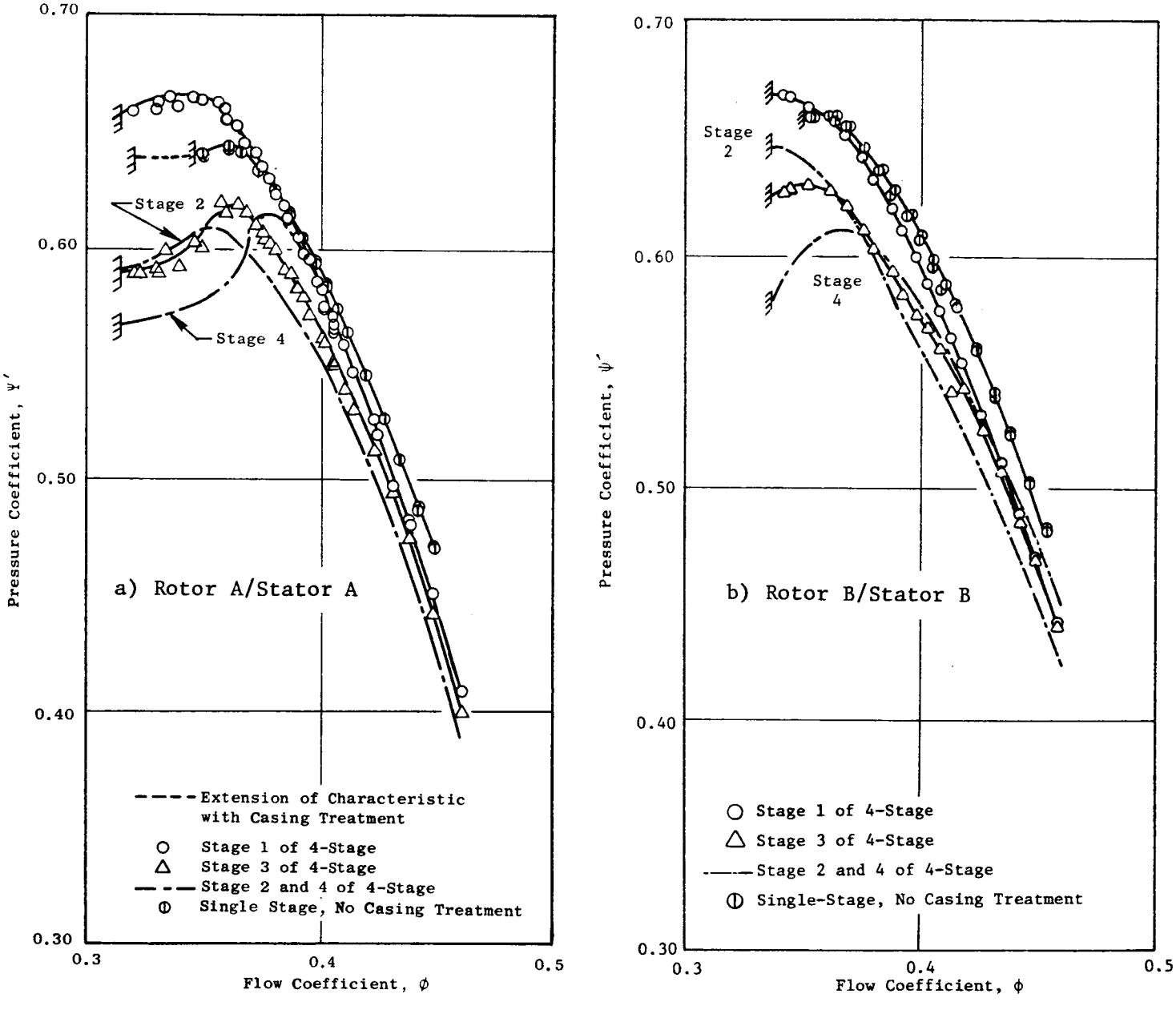

Figure 33. Comparison of the Individual Stage Characteristics for the Single-Stage and Four-Stage Configurations, Rotor A/Stator A, Rotor B/Stator B.

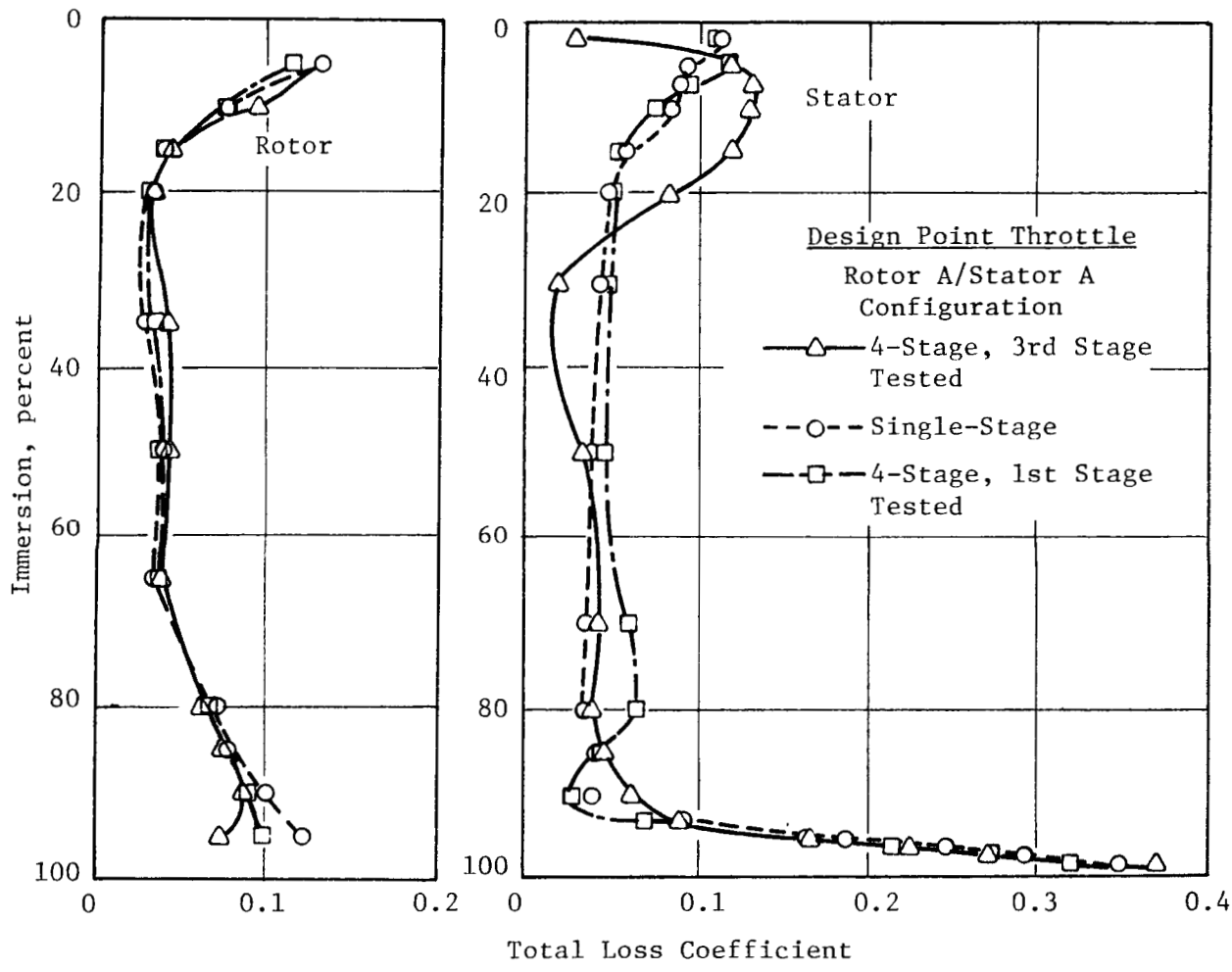

Figure 34. Comparison of the Radial Variation of Total Loss Coefficient for the Four-Stage Configuration and the Single-Stage Configuration.

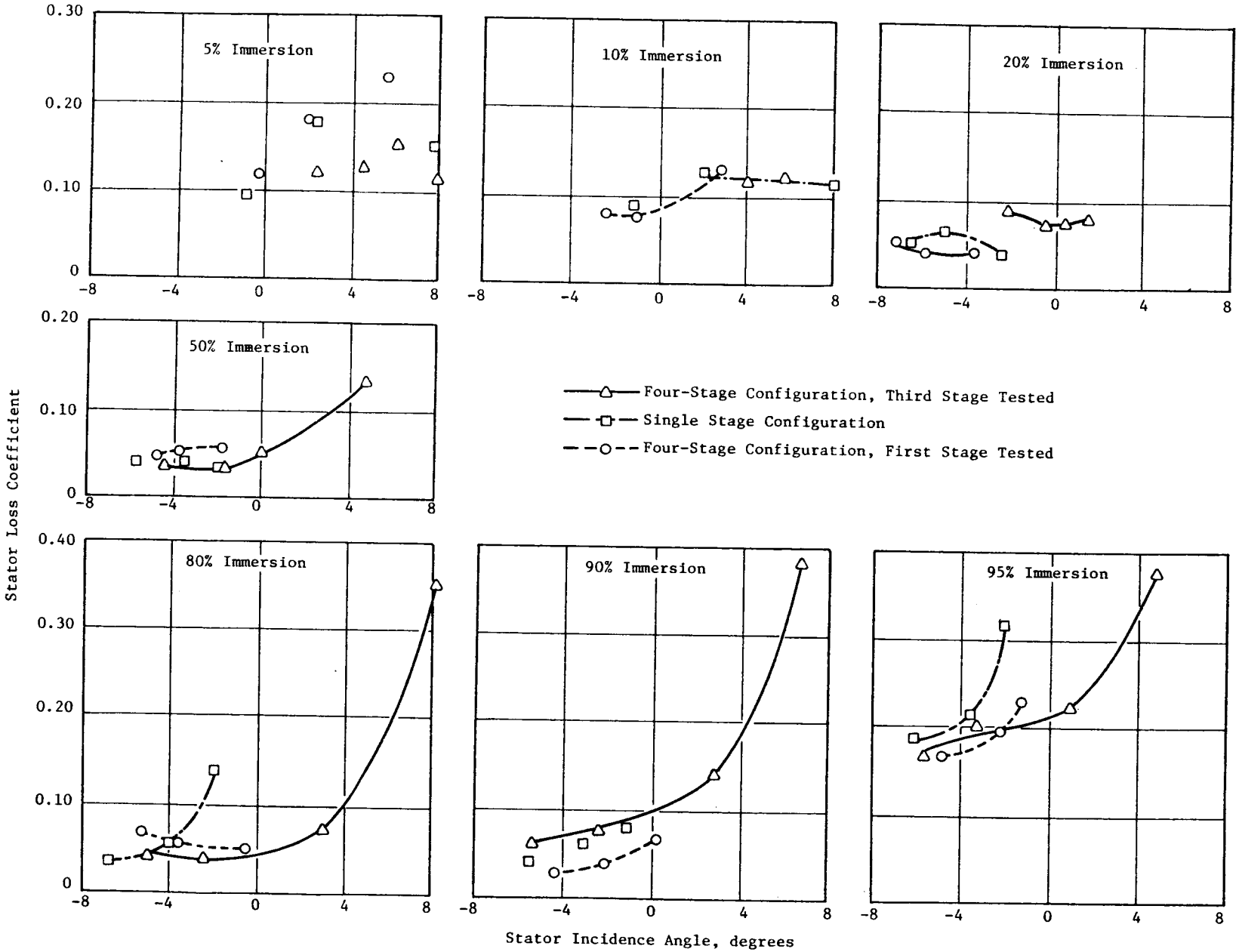

Figure 35. Stator Loss Coefficients Versus Incidence Angle for the Four-Stage and the Single-Stage Configurations.

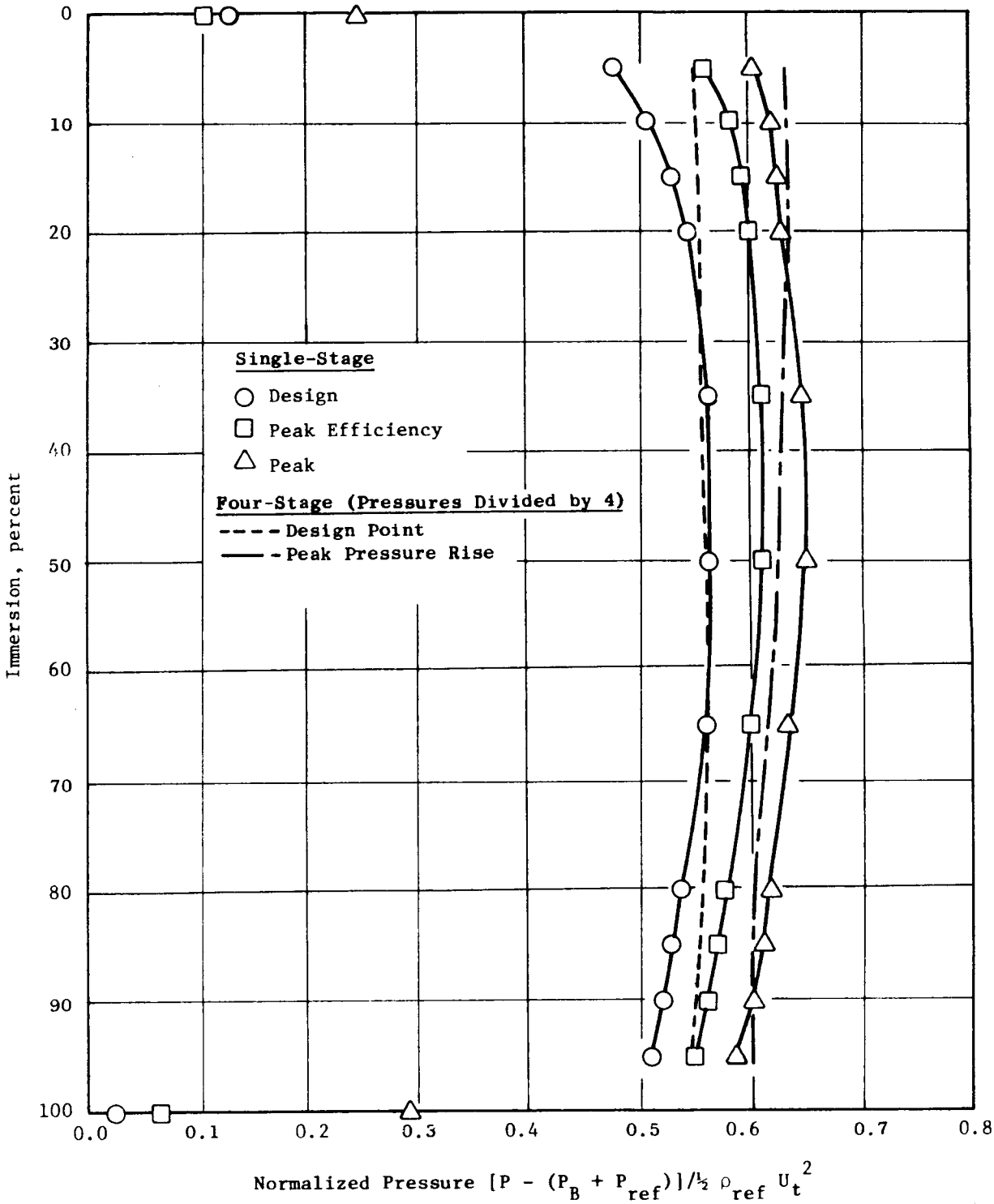

Figure 36. Radial Variation of Normalized Total Pressure at the Compressor Discharge for the Single-Stage and the Four-Stage Configurations.

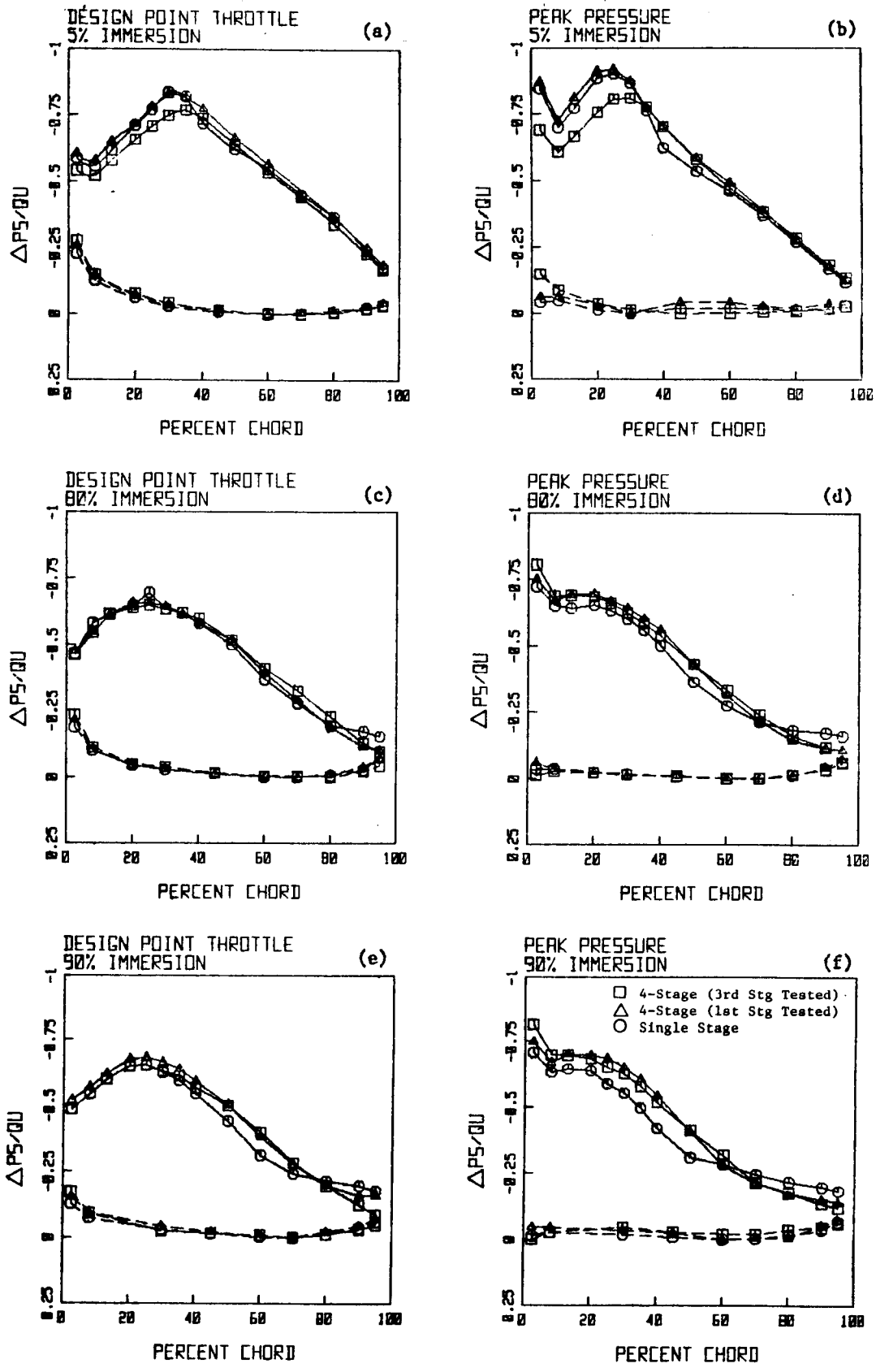

Figure 37. Comparison of Blade Surface Static Pressure Measurements for the Four-Stage Configuration (First and Third Stages Tested) and the Single-Stage Configuration for Rotor A/Stator A.

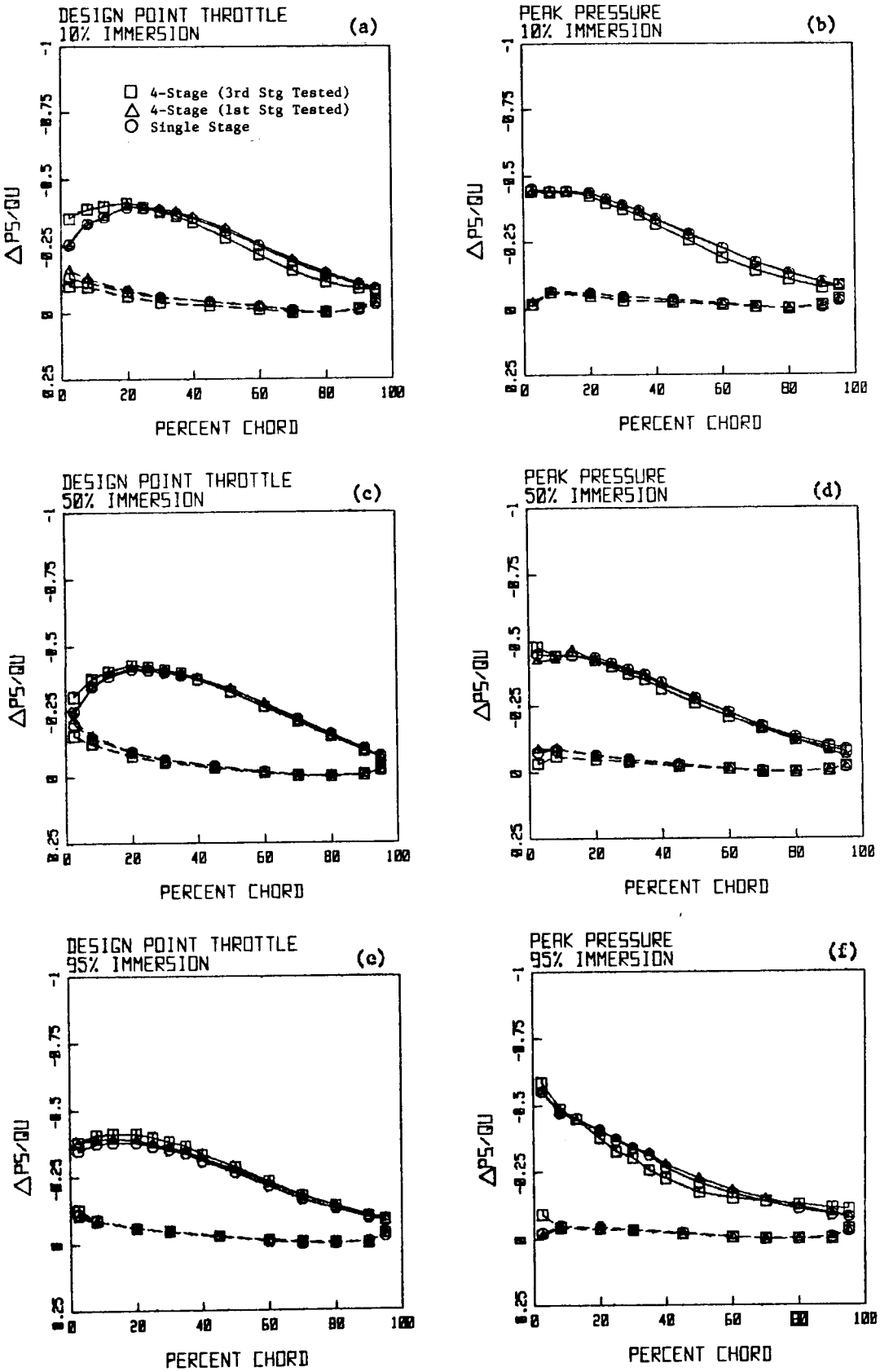

Figure 38. Comparison of Vane Surface Static Pressure Measurements for the Four-Stage Configuration (First and Third Stages Tested) and the Single-Stage Configuration for Rotor A/Stator A.

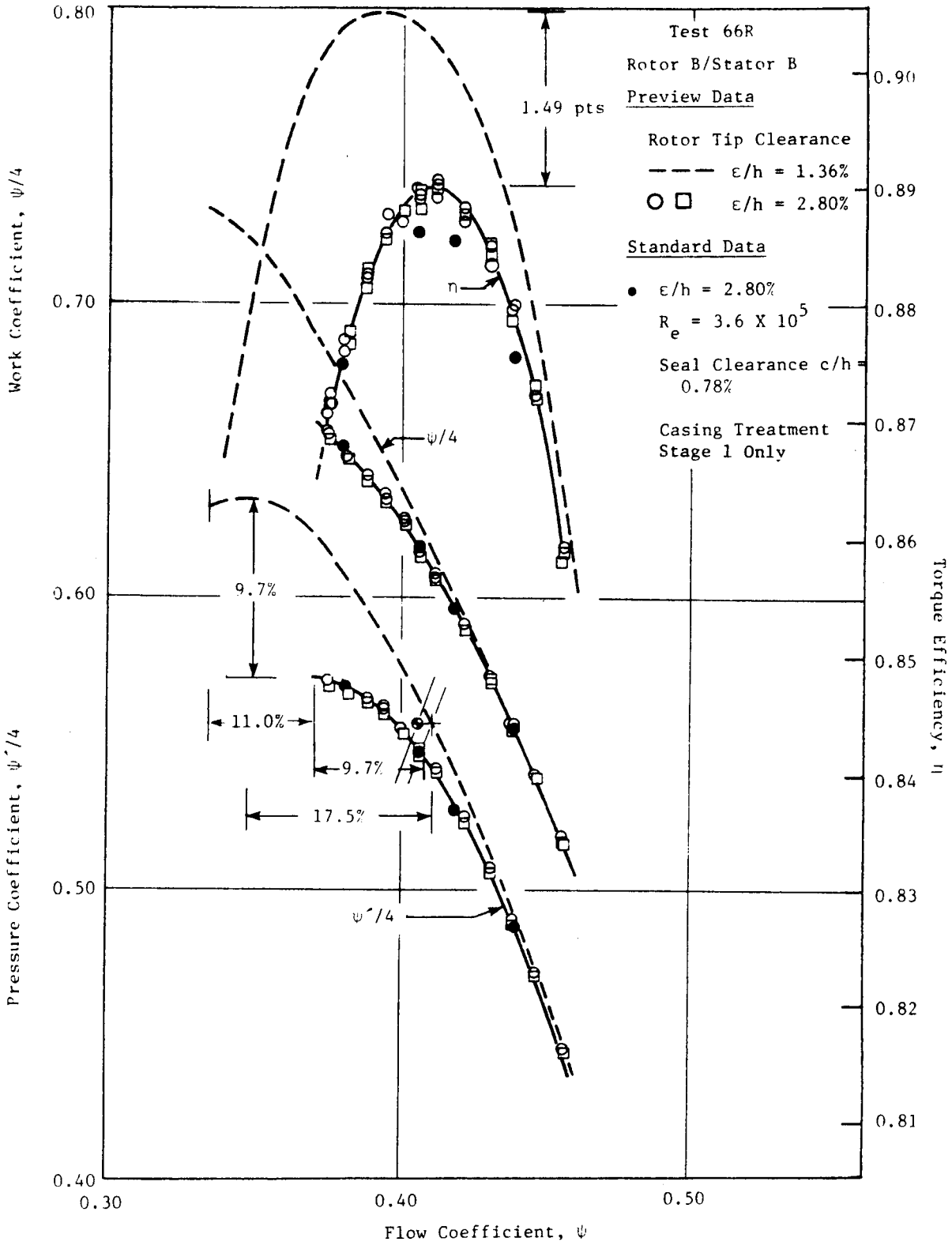

Figure 39. Comparison Showing the Effects of Increased Rotor Tip Clearance on Overall Compressor Performance, Rotor B/Stator B Four-Stage Configuration.

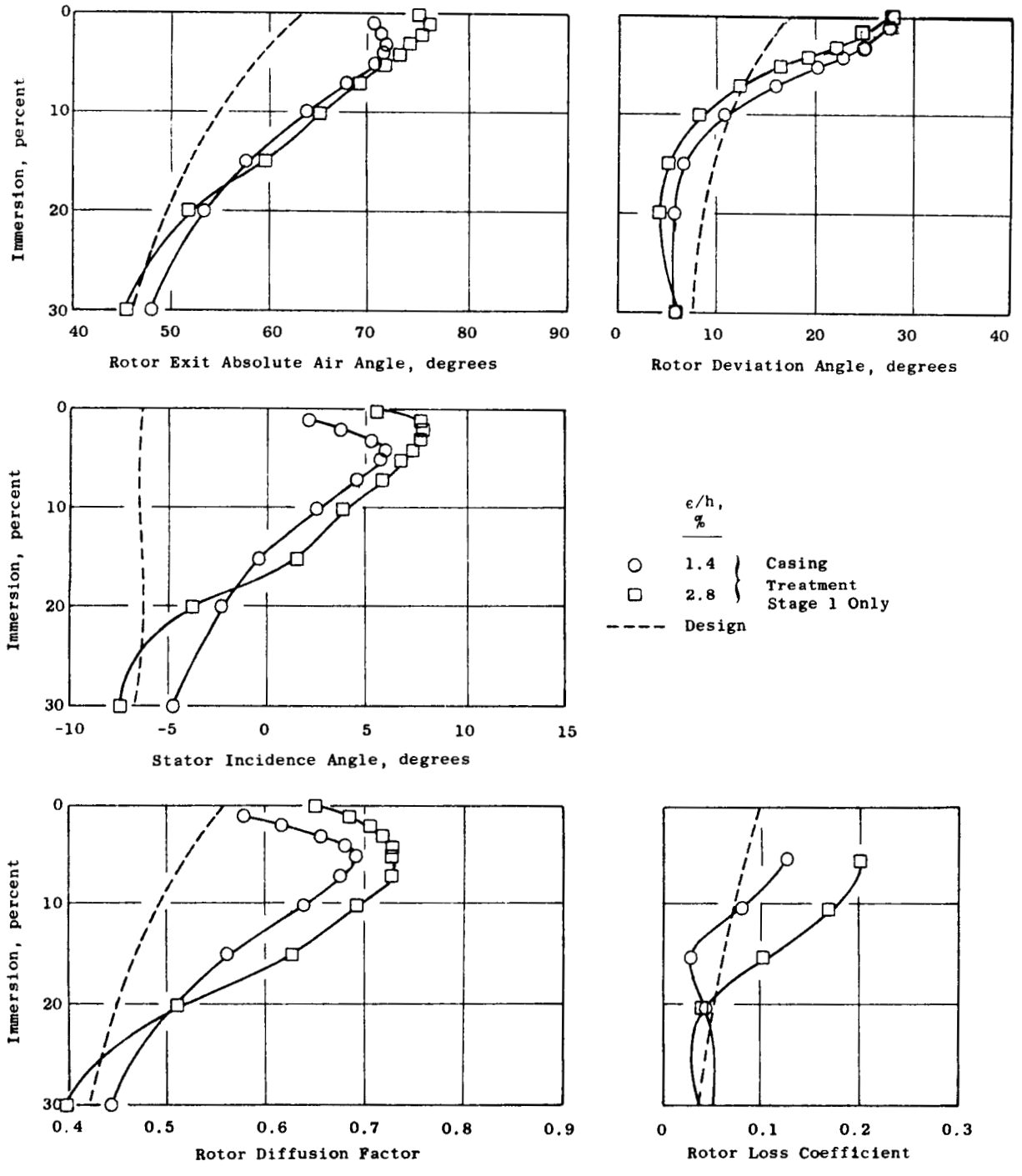

Figure 40. Comparison Showing the Effects of Increased Rotor Tip Clearance on Blade Element Performance, Rotor B/Stator B Four-Stage Configuration, Third Stage Tested.

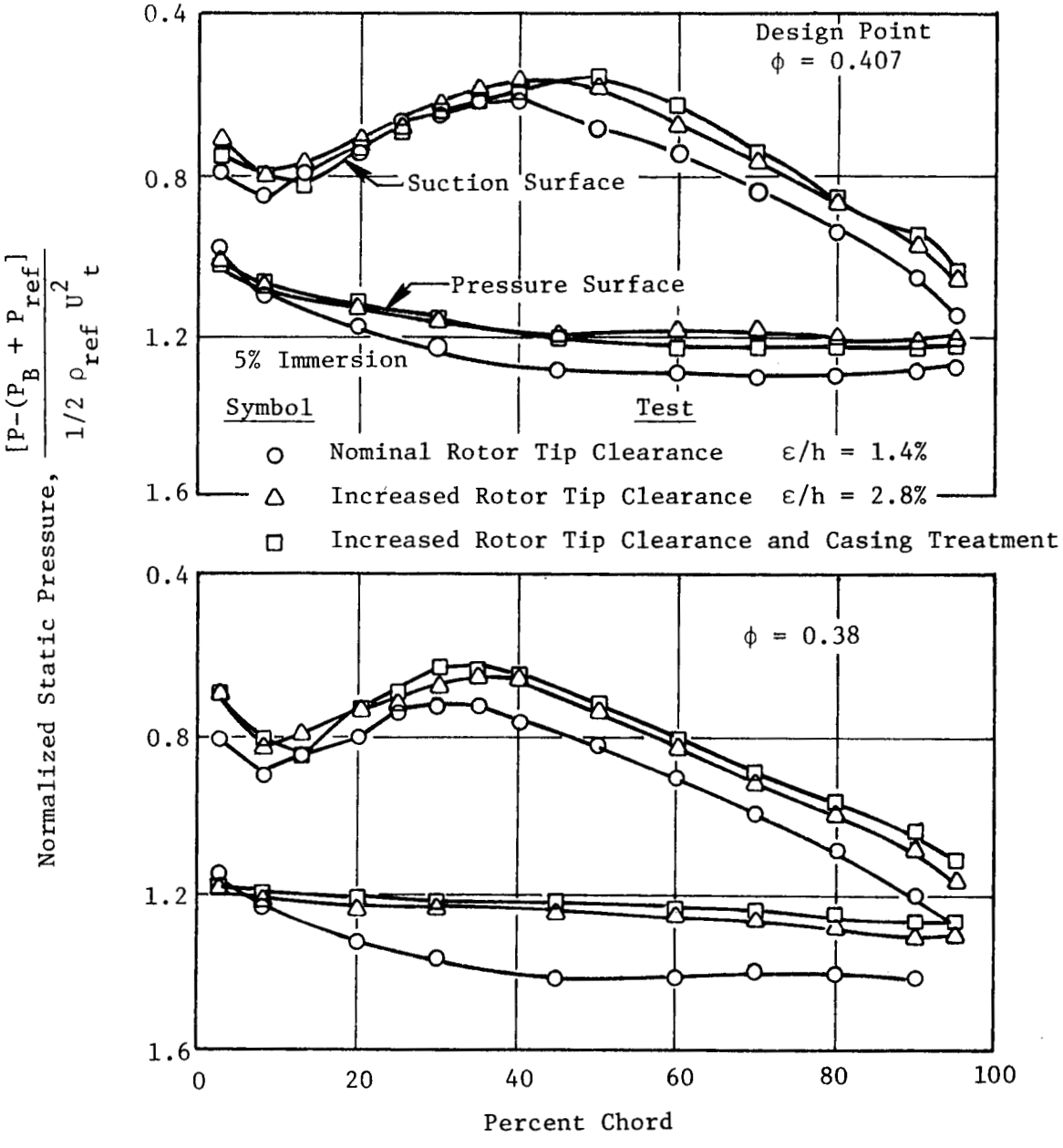

Figure 41. Effects of Increased Rotor Tip Clearance and Casing Treatment on Blade Surface Static Pressure Measurements Near the Tip of Rotor B, Four-Stage Configuration, Third Stage Tested.

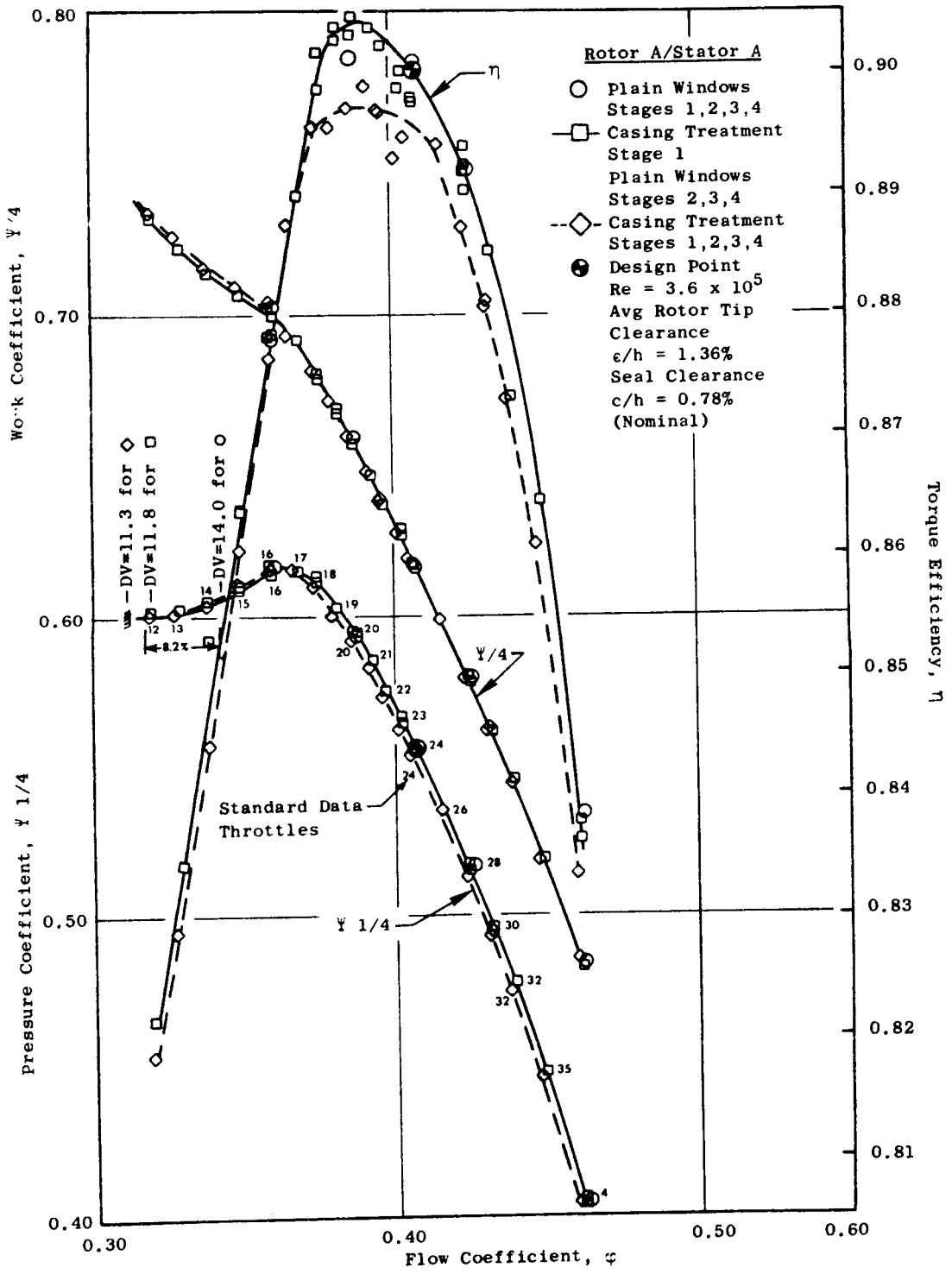

Figure 42. Effects of Circumferential Groove Casing Treatment on Compressor Performance.

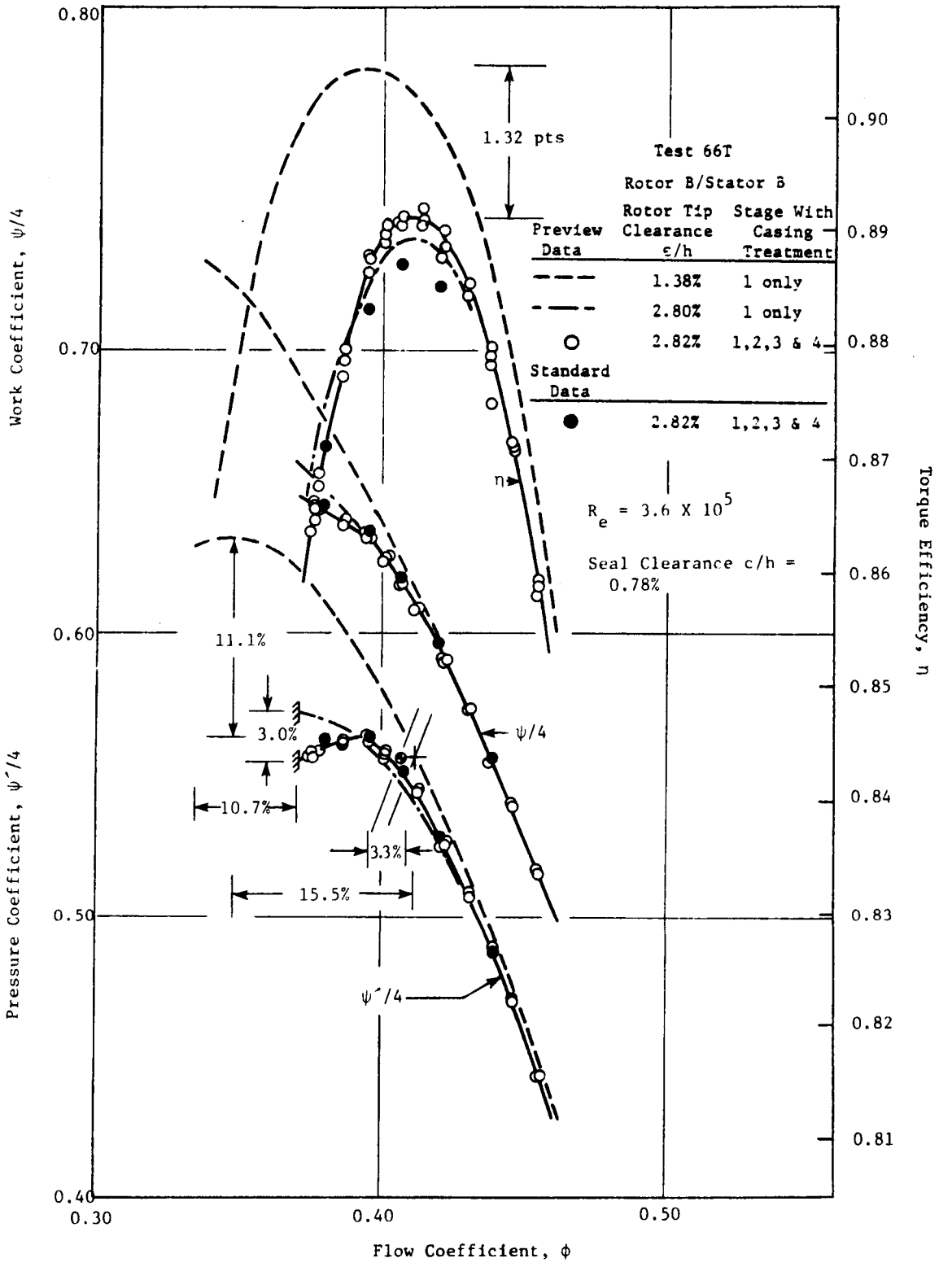

Figure 43. Comparison Showing the Effects of Increased Rotor Tip Clearance and Casing Treatment on Overall Compressor Performance, Rotor B/ Stator B Four-Stage Configuration.

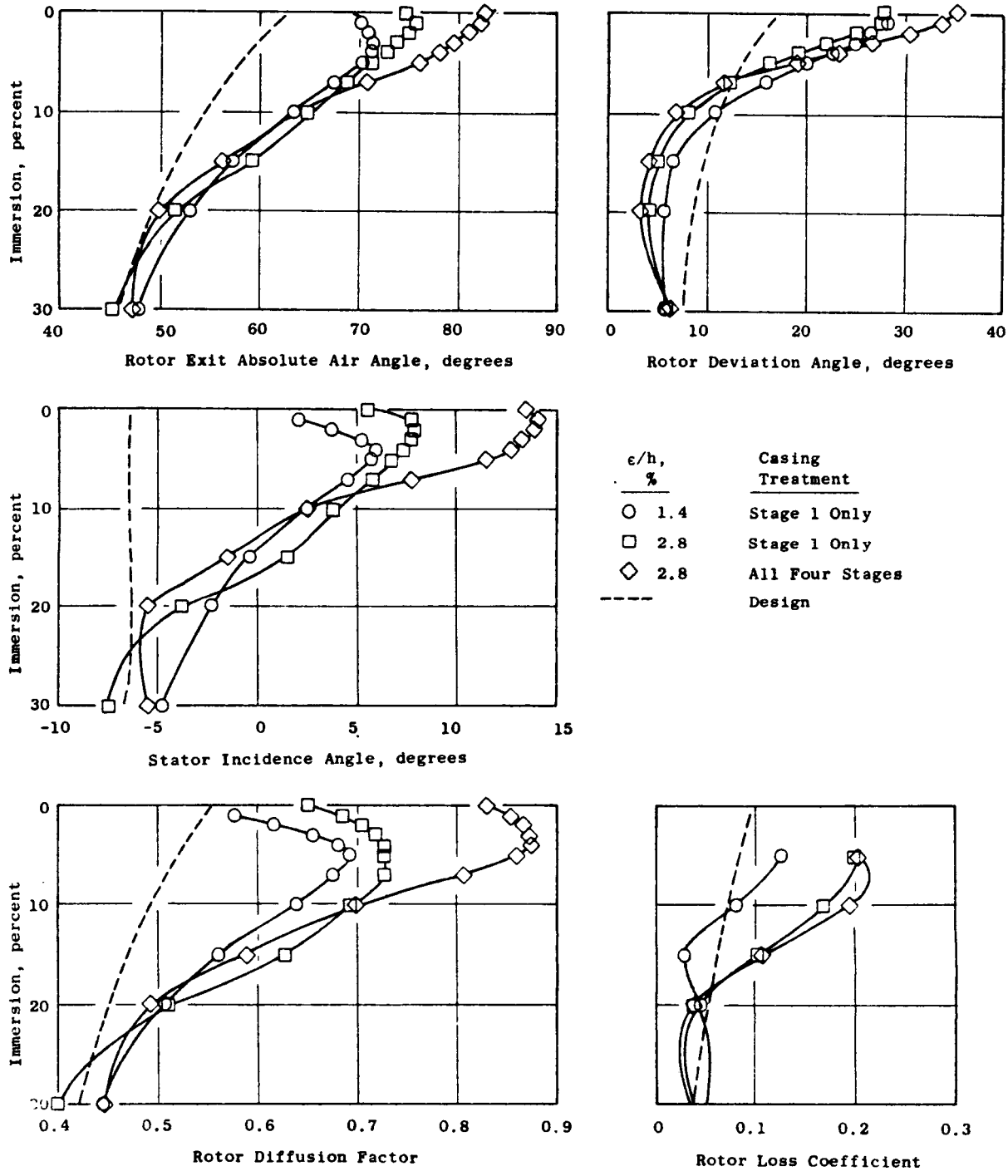

Figure 44. Comparison Showing the Effects of Increased Rotor Tip Clearance and Casing Treatment on Blade Element Performance, Rotor B/Stator B Four-Stage Configuration, Third Stage Tested.

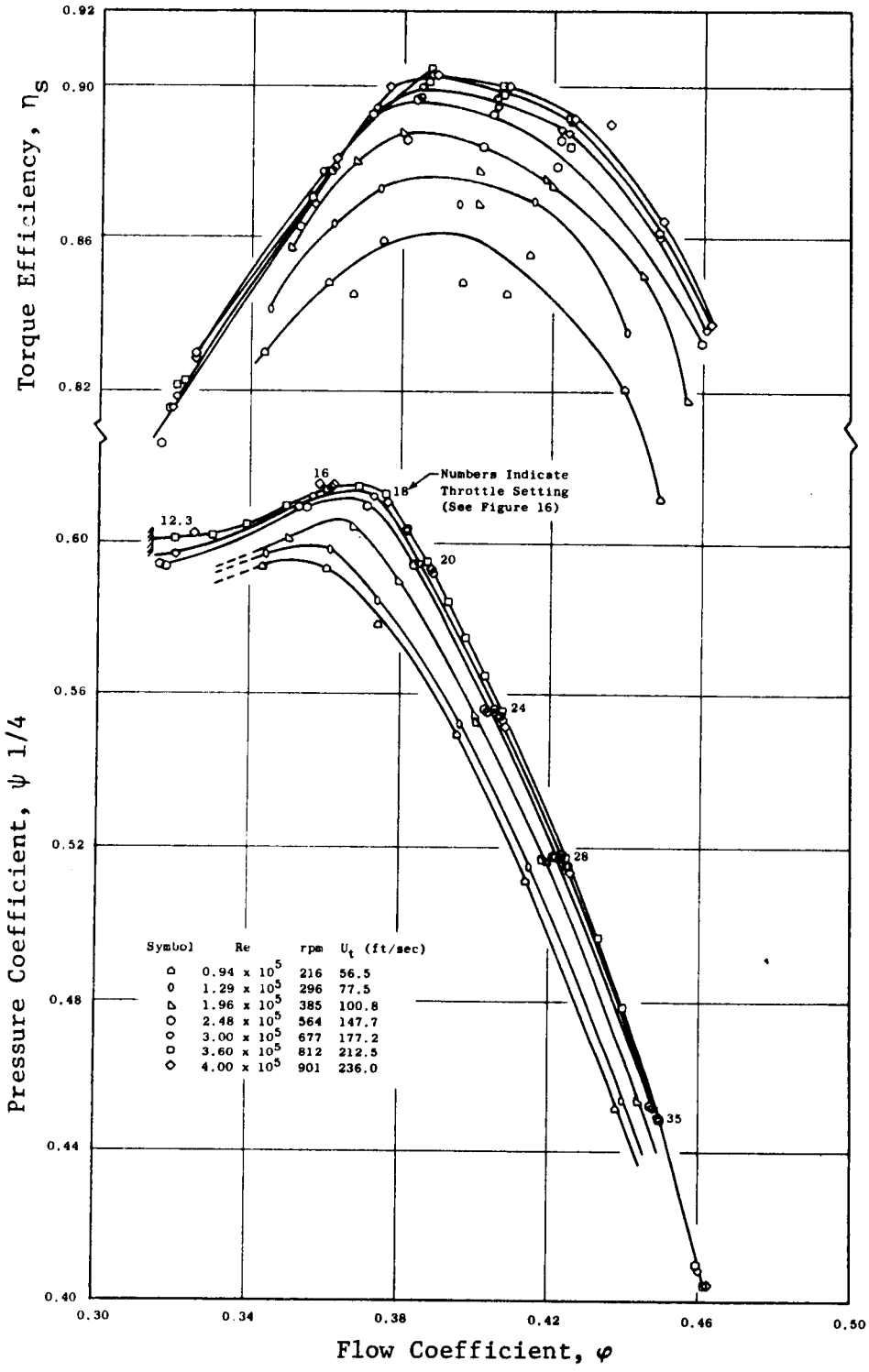

Figure 45. Effect of Reynolds Number on the Performance of Rotor A/Stator A, Four-Stage Configuration.

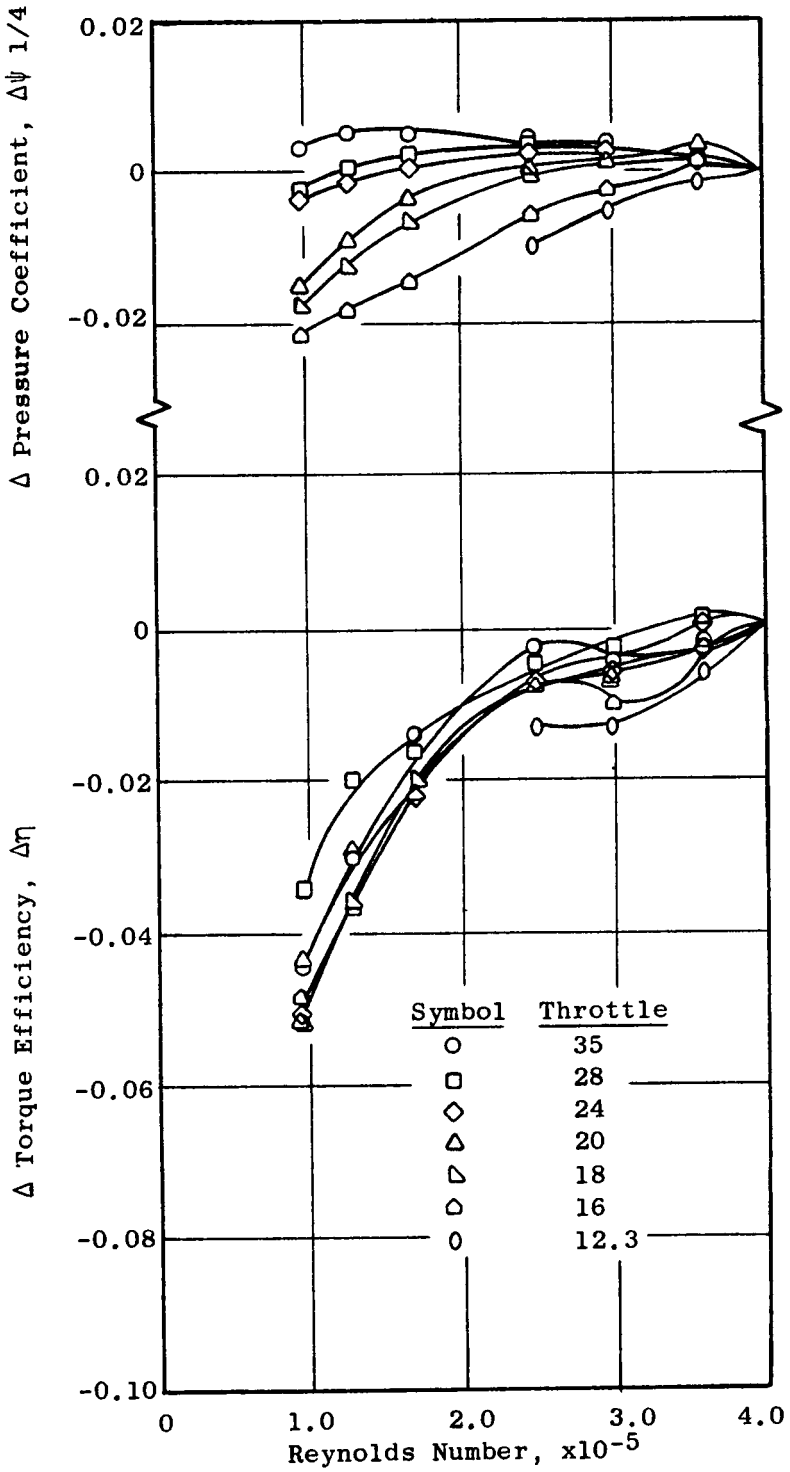

Figure 46. Effect of Reynolds Number on the Performance of Rotor A/Stator A, Four-Stage Configuration.

11.0 TABLES

Table 1. Overall Test Plan Outline for Complete Program.

I. Tests Using Stage A Blading (Reported in Ref. 1)	
A. Shakedown Test	5 data points
B. 4-Stage Configuration (Third Stage as Test Stage)	
1. Preview Data	15 data points
2. Stall Determination	As Appropriate
3. Casing Treatment Data	15 data points
4. Reynolds Number Data	30 data points
5. Standard Data	4 data points
6. Blade Element Data	4 data points
7. Blade Surface Pressure Data	2 data points
8. Detailed Wall Boundary Layer Data	2 data points
C. 1-Stage Configuration	
1. Preview Data	15 data points
2. Stall Determination	As Appropriate
3. Standard Data	4 data points
4. Blade Element Data	4 data points
5. Blade Surface Pressure Data	4 data points
6. Detailed Wall Boundary Layer Data	2 data points
D. 4-Stage Configuration (First Stage as Test Stage)	
1. Blade Element Data	4 data points
2. Blade Surface Pressure Data	4 data points
3. Detailed Wall Boundary Layer Data	2 data points
II. Screen Tests	
A. 4-Stage Configuration with Rotor B and Stator A	
1. Preview Data	15 data points
2. Stall Determination	As Appropriate
3. Standard Data	4 data points
4. Blade Surface Pressure Data	4 data points
B. 4-Stage Configuration with Stator B and Rotor A	
(Same Data as II.A.)	
C. 4-Stage Configuration with Stator C and Rotor A	
(Same Data as II.A.)	
D. 4-Stage Configuration with Rotor B and Stator B	
(Same Data as II.A.)	
III. Tests Using Rotor B and Stator B Designs	
A. 4-Stage Configuration, Third Stage as Test Stage	
1. Same Data as I.B., Except Delete I.B.3. and 4.	
2. Rotor Tip Clearance Data, Casing Treatment 4 Stages	
3. Rotor Tip Clearance Data, Casing Treatment Stage 1	
B. 1-Stage Configuration	
1. Same Data as I.C., Except Delete I.C.4. (Rotor Tip Clearance Data)	
IV. Tests Using Rotor C/Stator B Designs	
A. 4-Stage Configuration, Third Stage as Test Stage	
1. Same Data as I.B., Except Delete I.B.3. and 4.	

Table 2. Performance of the Various Blading Tested in the Core Compressor Exit Stage Study Program.

Four-Stage Configuration	Constant Throttle From Design Point			Peak Efficiency			Peak Pressure		Near Stall		Delta Efficiency Points		$1 - \frac{\phi_{St}}{\phi_{OL}}$	$\frac{\psi'_{PP}}{\psi'_{OL}} - 1$	$\frac{\phi/\sqrt{\psi'/4}_{OL}}{\phi/\sqrt{\psi'/4}_{ST}} - 1$
	η_{OL}	$\psi'/4_{OL}$	ϕ_{OL}	η_{PE}	$\psi'/4_{PE}$	ϕ_{PE}	$\psi'/4_{PP}$	ϕ_{PP}	$\psi'/4_{NS}$	ϕ_{NS}	$\Delta\eta_{OL}$	$\Delta\eta_{PE}$	Δ Flow %	$\Delta\psi'$ %	Throttle Area Stall Margin %
Baseline															
Rotor A/Stator A	.9003	.556	.407	.9045	.593	.388	.616	.364	.6005	.314	---	---	22.8	10.8	34.7
Rotor B/Stator A	.9027	.559	.4082	.9036	.5782	.398	.618	.363	.6085	.3375	0.24	-0.09	17.3	10.6	26.2
Stator B/Rotor A	.9044	.5593	.4081	.9060	.5792	.397	.636	.348	.632	.3335	0.41	0.15	17.9	13.7	25.6
Rotor B/Stator B	.9033	.5618	.4092	.9047	.588	.396	.6335	.349	.6305	.338	0.30	0.02	17.4	12.8	28.3
Rotor C/Stator B	.9051	.5629	.4095	.9060	.586	.398	.632	.344	.630	.329	0.48	0.15	19.7	12.3	31.7
Stator C/Rotor A	.8998	.5538	.4064	.9015	.585	.390	.617	.365	.600	.314	-0.05	-0.30	22.7	11.4	34.7
Single-Stage Configuration															
Rotor A/Stator A	.8802	.5713	.4124	.8845	.612	.392	.647	.361	.642	.349	-2.01	-2.00	15.4	13.3	25.3
Rotor B/Stator B	.8914	.5790	.4152	.8934	.616	.396	.660	.353	.660	.353	-1.19*	-1.13*	15.0	14.0	25.6
Other Four-Stage Configurations	*Measured relative to Rotor B/Stator B														
Rotor A/Stator A Casing Treatment All Four Stages	.8960	.553	.4055	.8970	.594	.390	.616	.365	.600	.313	-0.43	-0.75	22.8	11.4	34.9
Rotor B/Stator B Increased Tip Clearance ϵ/h = 2.8%	.8891	.5506	.4045	.8898	.5405	.412	.572	.372	.572	.372	-1.42*	-1.49*	8.03	3.9	10.8
Rotor B/Stator B Increased Tip Clearance and Casing Treatment All 4 stages	.8909	.5528	.4059	.8915	.544	.412	.563	.394	.555	.3708	-1.24*	-1.32*	8.65	1.8	9.7

12.0 REFERENCES

1. Wisler, D.C., Koch, C.C., and Smith, L.H., Jr., "Preliminary Design Study of Advanced Multistage Axial Flow Core Compressors," NASA CR-135133, February 1977.

2. Koch, C.C., and Smith, L.H., Jr., "Loss Sources and Magnitudes in Axial-Flow Compressors," Transitions of ASME, Journal of Engineering for Power, Vol. 98, Series A, No. 3, July 1976, p. 411.

3. Wisler, D.C, "Core Compressor Exit Stage Study, Volume I - Blading Design," NASA CR-135391, December 1977.

4. Wisler, D.C., "Core Compressor Exit Stage Study Volume II - Data and Performance Report for Rotor A/Stator A Baseline Configuration," NASA CR-159498, November 1980.

5. Wisler, D.C., "Core Compressor Exit Stage Study, Volume III - Data and Performance Report for Screening Test Configurations," NASA CR-159499, December 1980.

6. Wisler, D.C., "Core Compressor Exit Stage Study, Volume IV - Data and Performance Report for the Best Stage Configuration," NASA CR-165357, April 1981.

7. Wisler, D.C., "Core Compressor Exit Stage Study, Vol. V - Design and Performance Report for the Rotor C/Stator B Configuration," NASA CR-165358, May 1981.

8. Brent, J.A., and Clemons, D.R., "Single-Stage Experimental Evaluation of Tandem-Airfoil Rotor and Stator Blading for Compressors," Final Report NASA CR-134713, November 1974.

13.0 APPENDIX

Graphs of deviation angle, total loss coefficient, and diffusion factor plotted as a function of incidence angle are presented for the various configurations in which detailed data were obtained.

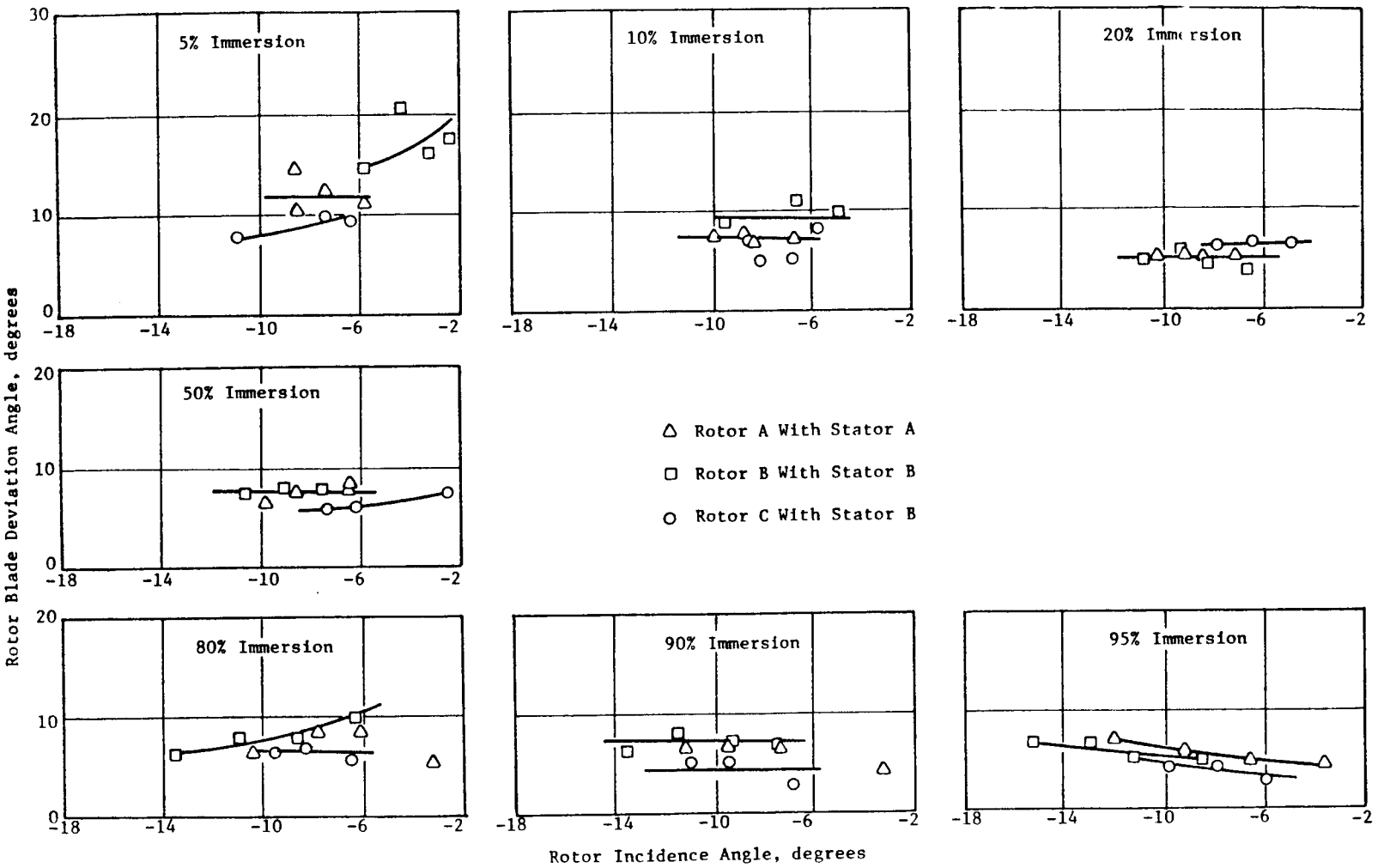

Figure A1. Rotor Deviation Angle Versus Incidence Angle, Four-Stage Configuration, Third Stage Tested.

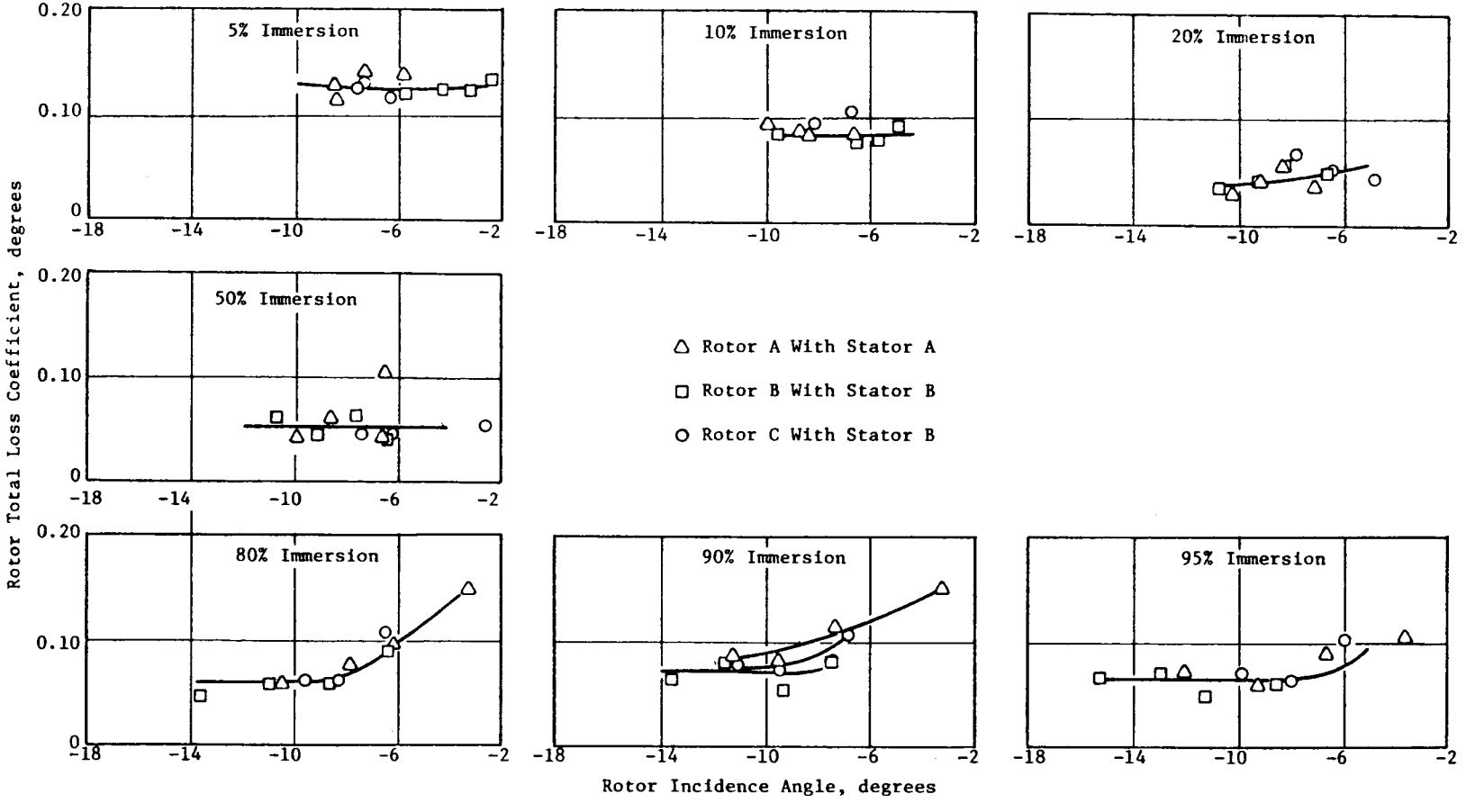

Figure A2. Rotor Total Loss Coefficient Versus Incidence Angle, Four-Stage Configuration, Third Stage Tested.

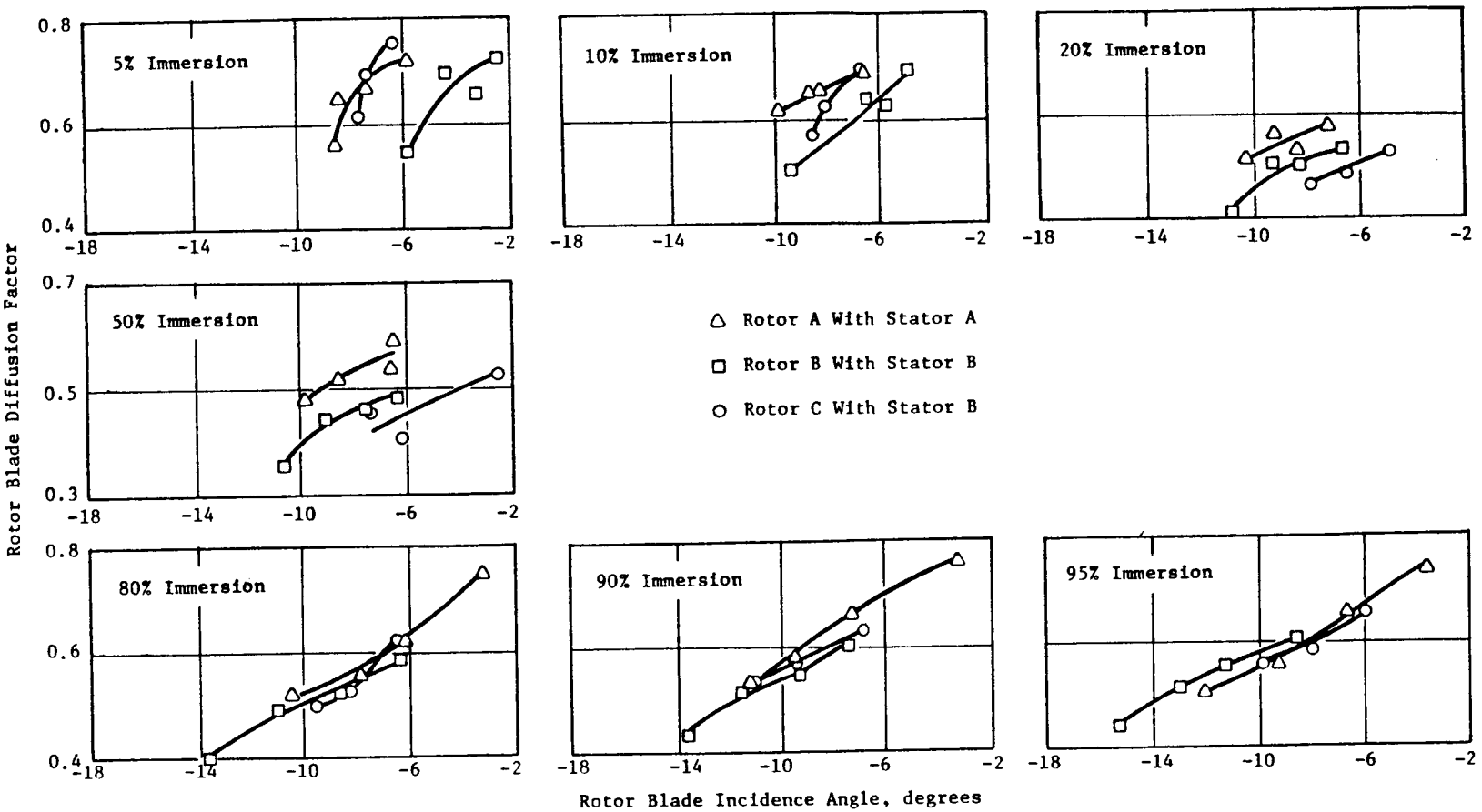

Figure A3. Rotor Diffusion Factor Versus Incidence Angle, Four-Stage Configuration, Third Stage Tested.

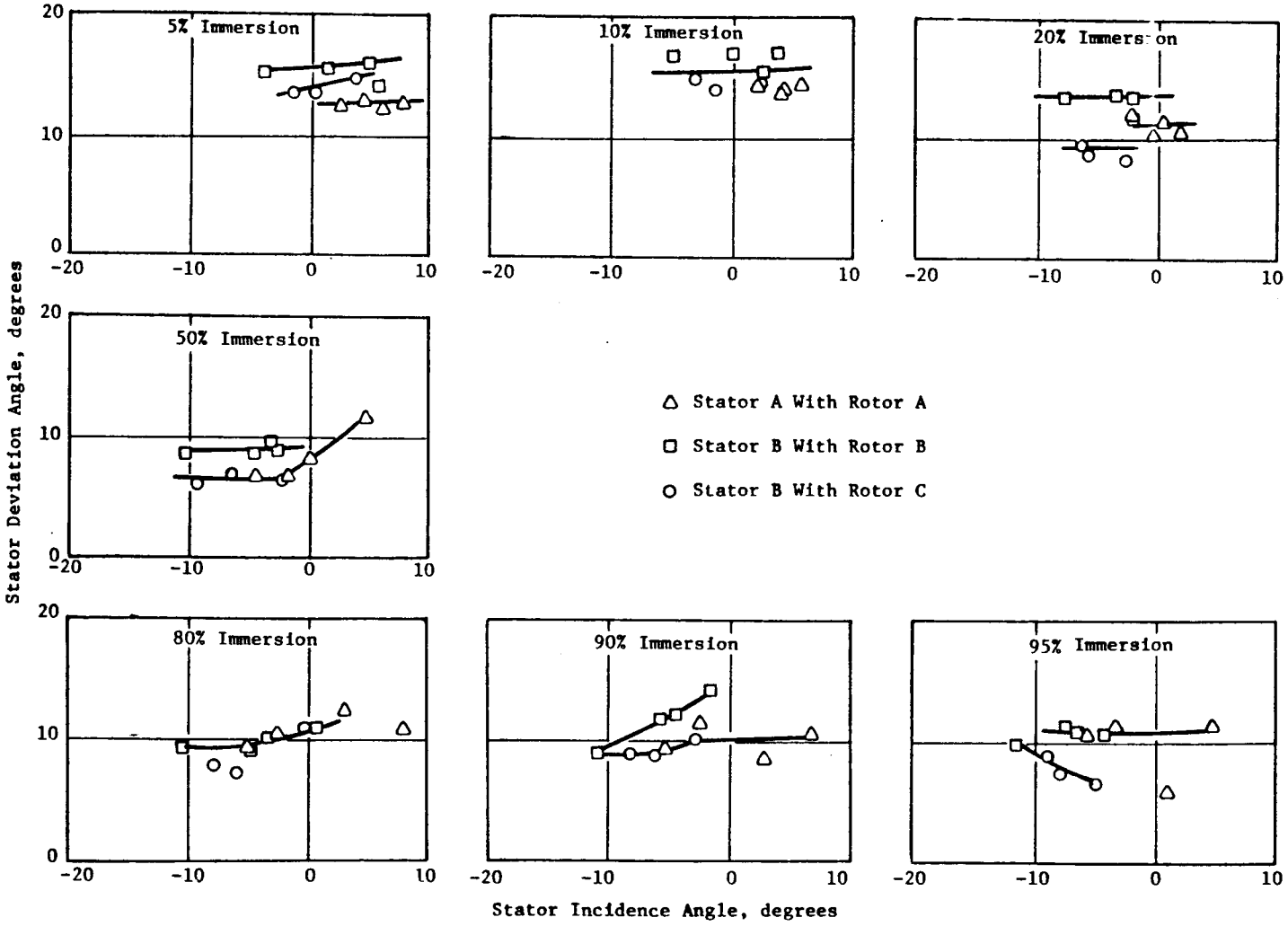

Figure A4. Stator Deviation Angle Versus Incidence Angle, Four-Stage Configuration, Third Stage Tested.

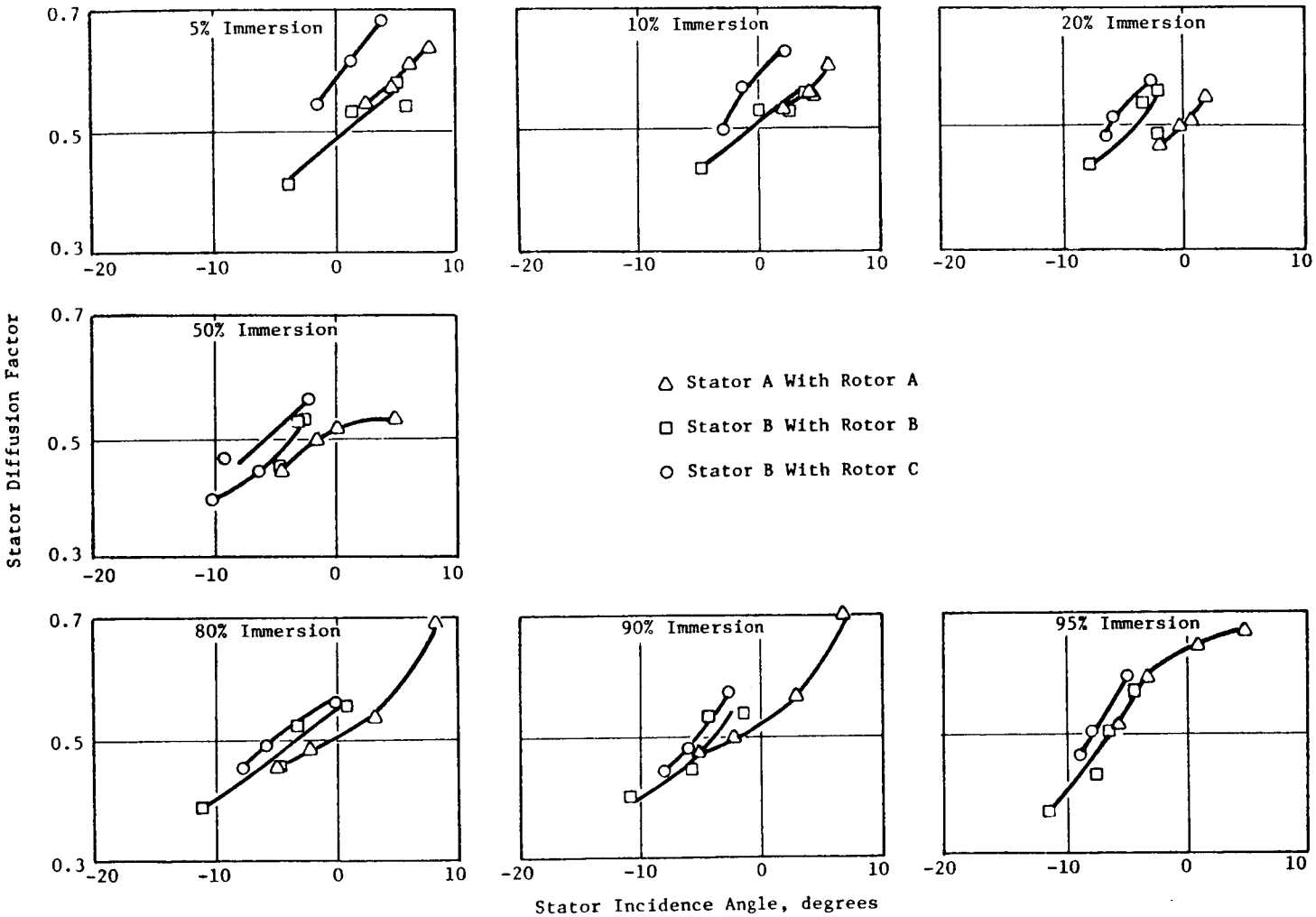

Figure A5. Stator Diffusion Factor Versus Incidence Angle, Four-Stage Configuration, Third Stage Tested.

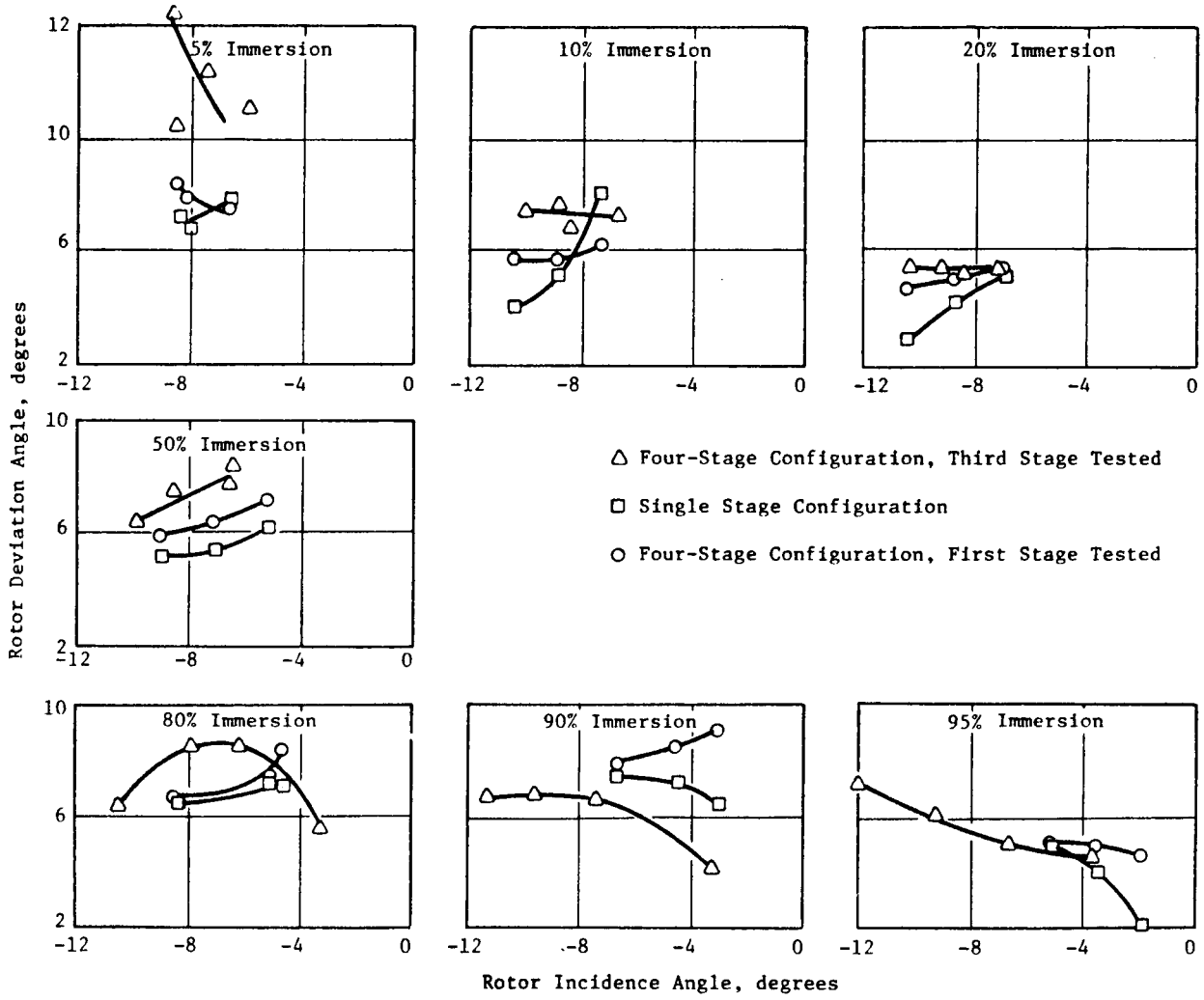

Figure A6. Rotor Deviation Angle Versus Incidence Angle for the Four-Stage and Single-Stage Configurations.

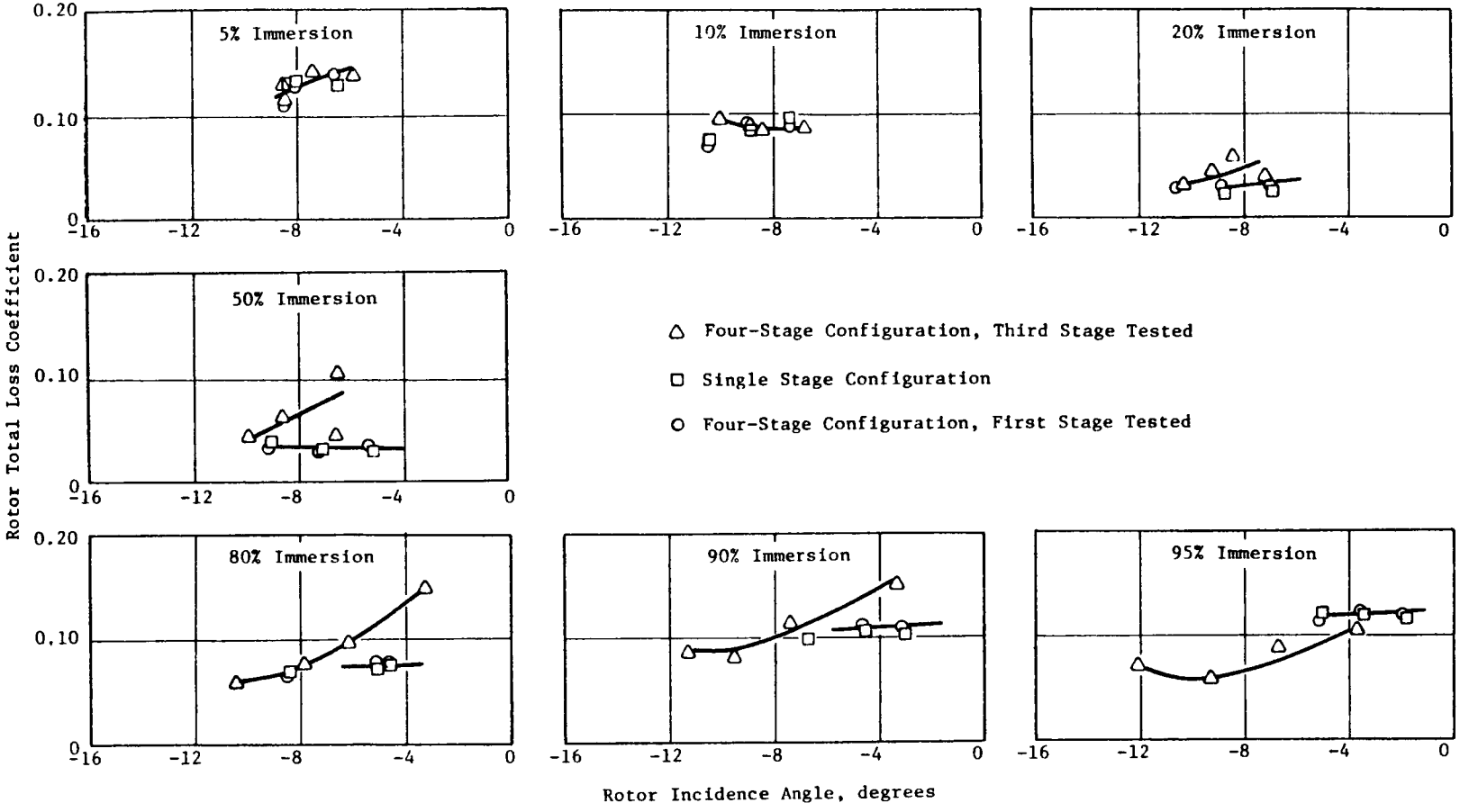

Figure A7. Rotor Loss Coefficients Versus Incidence Angle for the Four-Stage and Single-Stage Configurations.

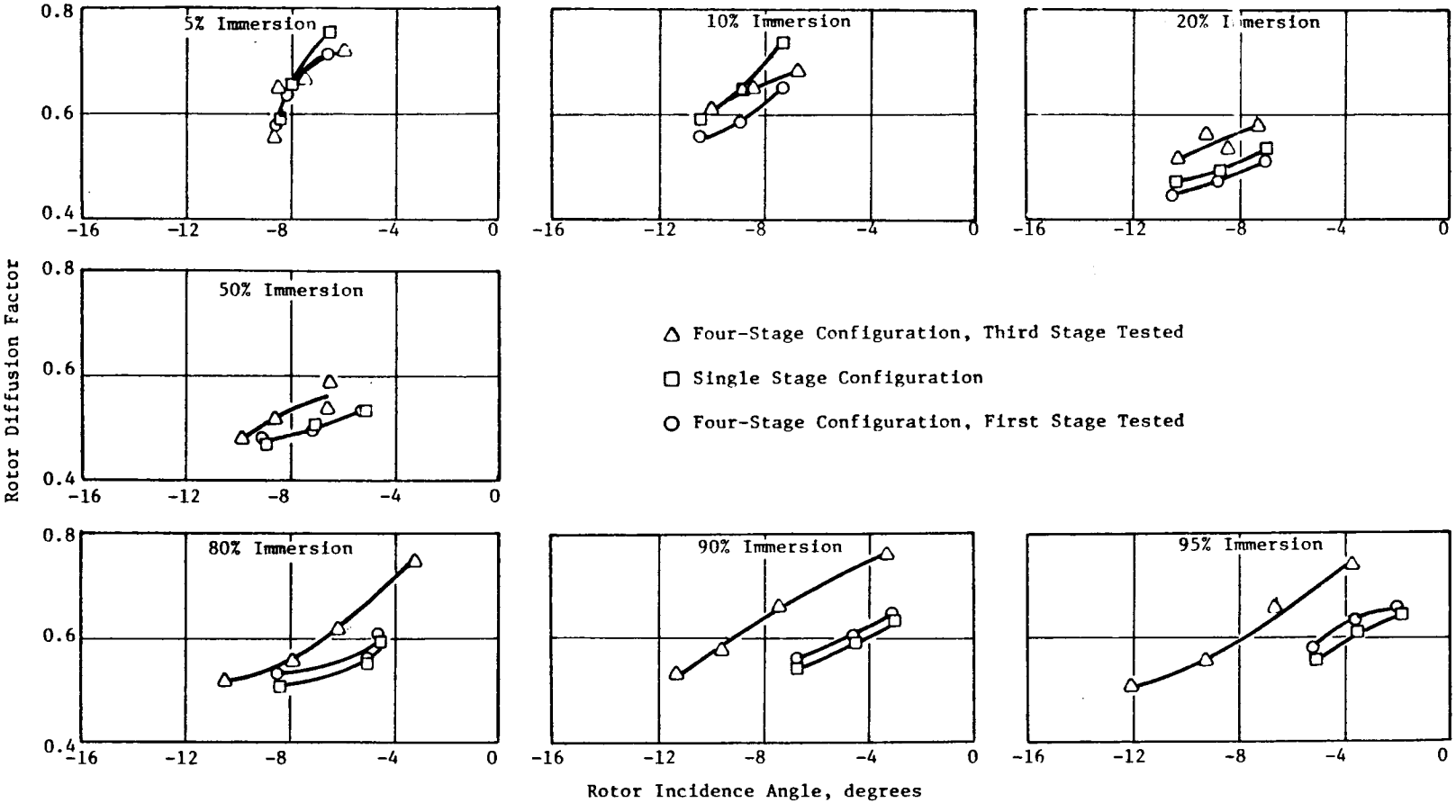

Figure A8. Rotor Diffusion Factor Versus Incidence Angle for the Four-Stage and Single-Stage Configurations.

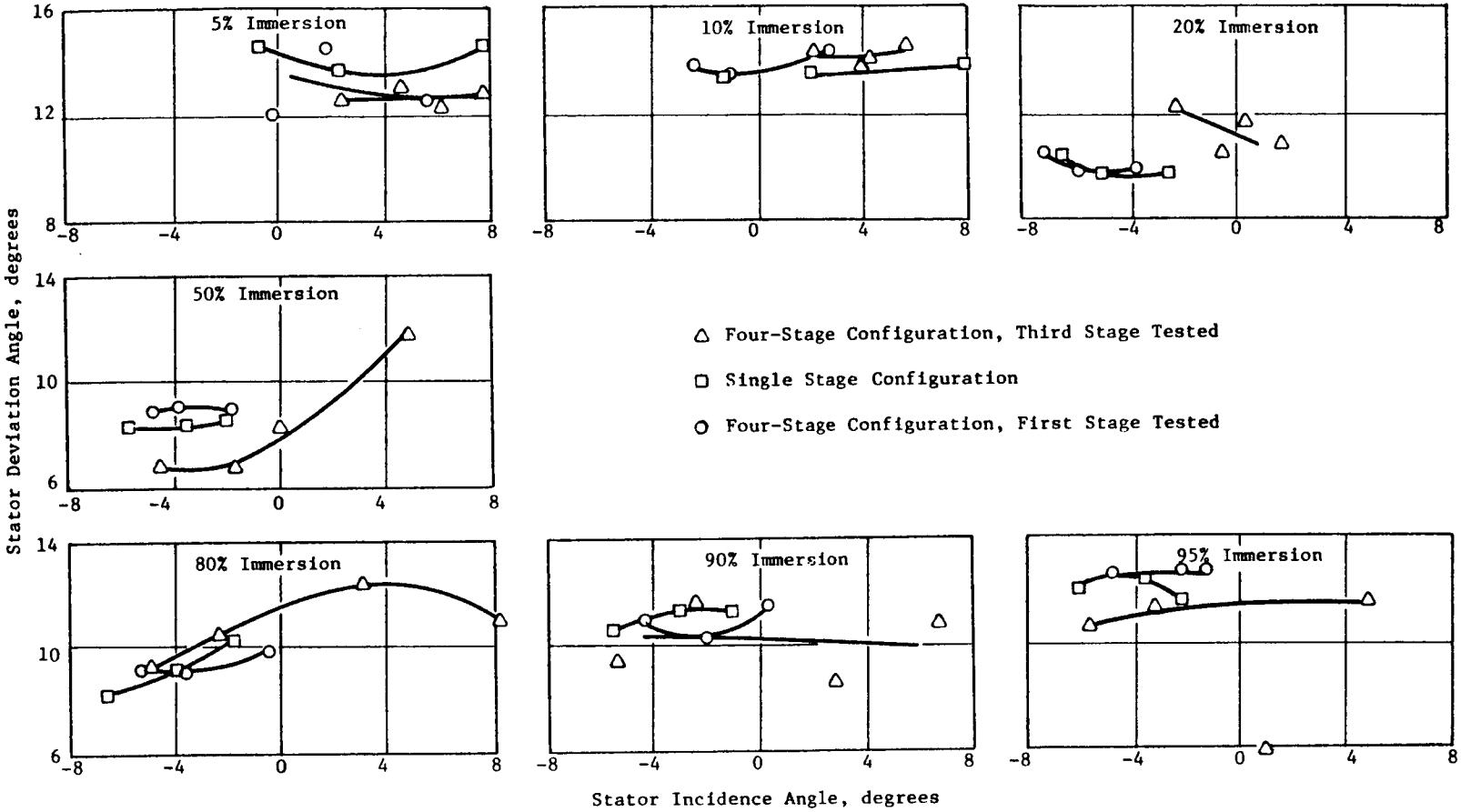

Figure A9. Stator Deviation Angle Versus Incidence Angle for the Four-Stage and Single-Stage Configurations.

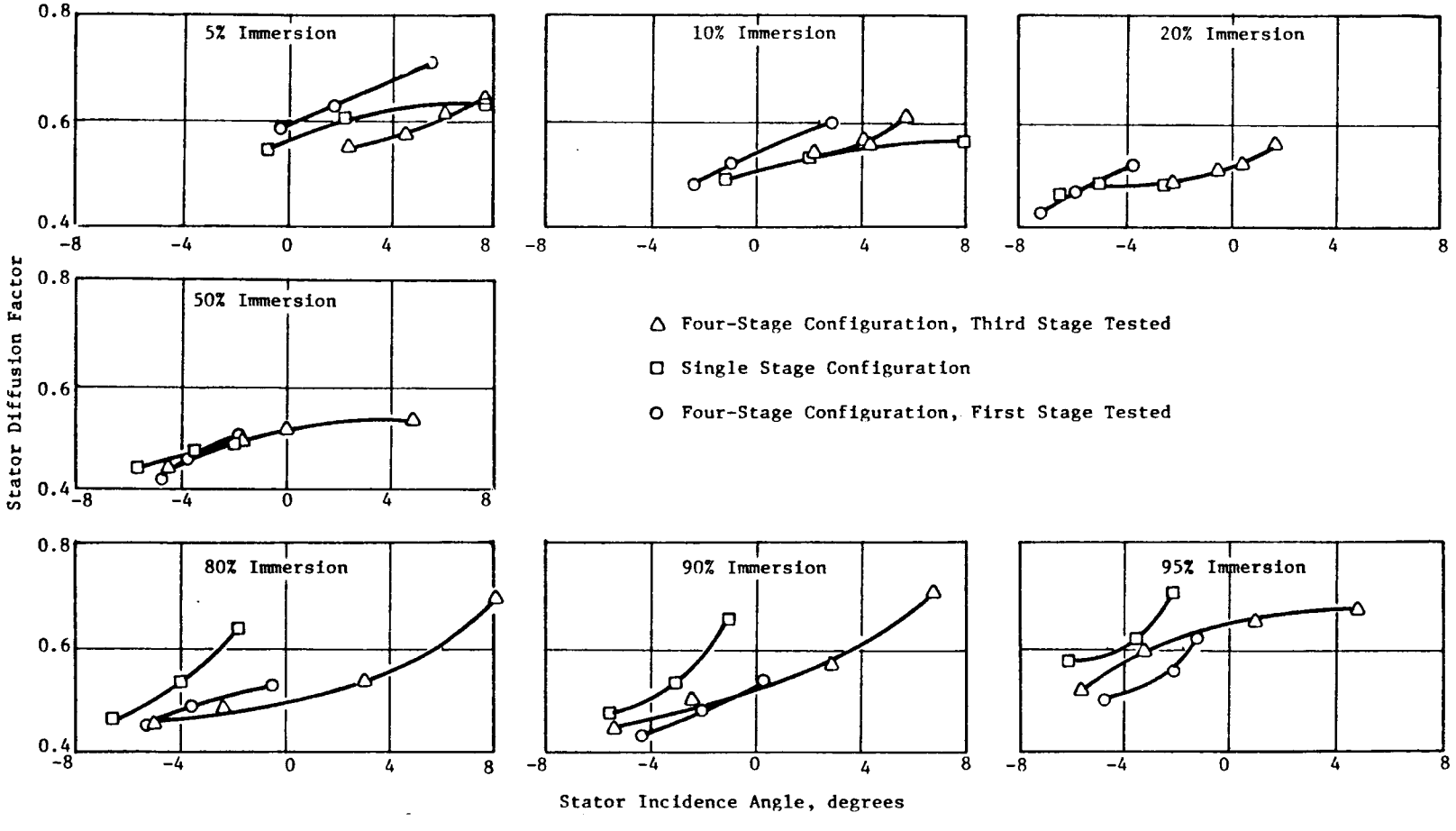

Figure A10. Stator Diffusion Factor Versus Incidence Angle for the Four-Stage and Single-Stage Configurations.

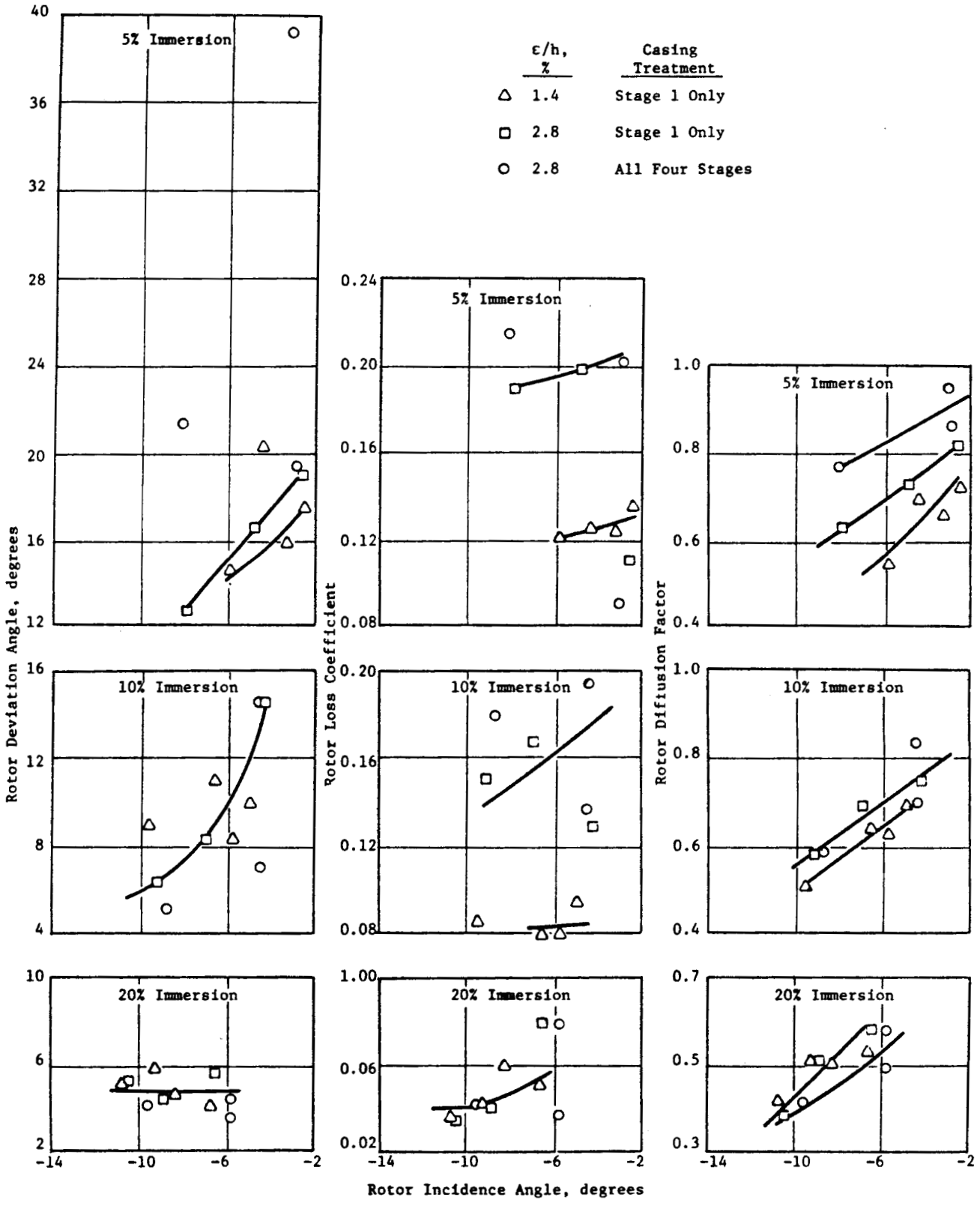

Figure All. Rotor Diffusion Factor, Loss Coefficient and Deviation Angle Versus Incidence Angle, Rotor B/Stator B Four-Stage Configuration, Third Stage Tested.

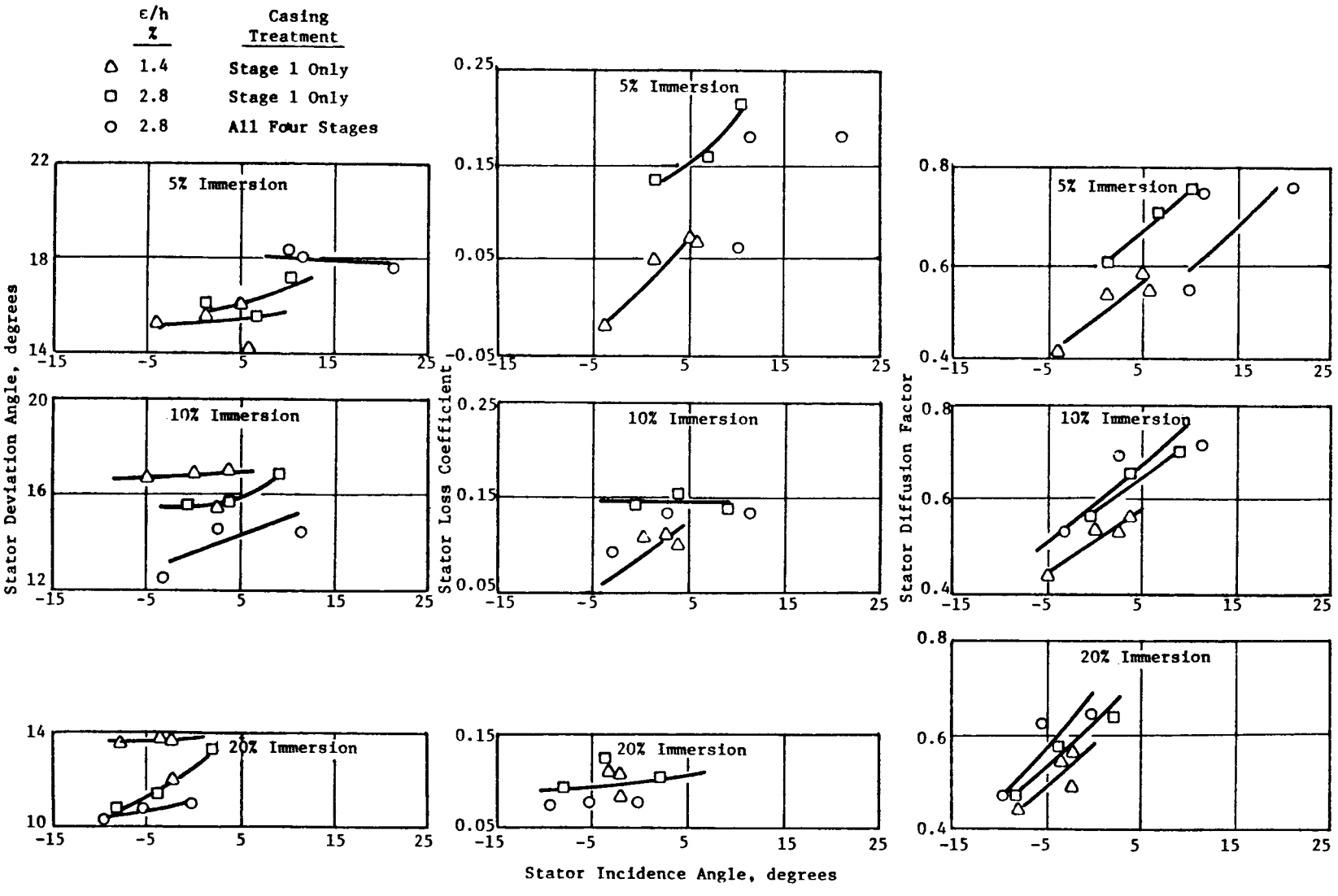

Figure A12. Stator Diffusion Factor, Loss Coefficient and Deviation Angle Versus Incidence Angle, Rotor B/Stator B Four-Stage Configuration, Third Stage Tested.

DISTRIBUTION LIST

CONTRACT NAS3-20070

1.	NASA-Lewis Research Center 21000 Brookpark Road Cleveland, OH 44135 Attention:		
	Report Control Office	M.S. 5-5	1
	Technical Utilization Office	M.S. 7-3	1
	Library	M.S. 60-3	2
	Fluid Mechanics & Acoustics Division	M.S. 5-3	1
	Fan and Compressor Branch	M.S. 5-9	5
	L. Reid	M.S. 5-9	1
	D.M. Sandercock	M.S. 5-9	1
	T.F. Gelder	M.S. 5-9	1
	C.L. Ball	M.S. 5-9	1
	W.A. Rostafinski	M.S. 5-9	1
	N.T. Musial	M.S. 500-318	1
	R.D. Hager	M.S. 301-4	1
	L.E. Macioce	M.S. 301-4	1
	D.L. Nored	M.S. 301-2	1
	W.R. Britsch	M.S. 301-2	1
	J.F. Dugan	M.S. 301-2	1
	J.E. McAulay	M.S. 301-4	1
2.	NASA Scientific and Technical Information Facility 6571 Elkridge Landing Road Linthicum Heights, MD 21090 Attn: Accessioning Department		25
3.	NASA Headquarters Washington, D.C. Attn: RTP-6/G. Banerian		1
4.	U.S. Army Applied Technology Laboratories (AVRADCOM) Director Applied Technology Laboratory Fort Eustis, VA 23604 Attn: DAVDL-EU-TA, John White		1
5.	NASA-Langley Research Center Hampton, VA 23665		
	Attn: S.J. Morris	M.S. 249B	1
	L. Hasel	M.S. 407	1

6.	Headquarters Wright-Patterson AFB, OH 45433		
	Attn: E.E. Bailey, AFWAL/NASA-PO		1
	R.P. Carmichael ASD/XRHI		1
	S. Kobelak, AFWAL/POTX		1
	A.J. Wennerstrom, AFWAL/POTX		1
	M.A. Stibich, AFWAL/POTX		1
7.	Naval Air Systems Command NASAIR/52022 Technical Support Branch Washington, D.C. 20362		
	Attn: R.A. Retta		1
8.	U.S. Navy Ship/Engineering Center Code 6141 Washington, D.C. 20362		
	Attn: G.L. Graves		1
9.	Naval Air Propulsion Center Trenton, NJ 08628		
	Attn: V. Labosky	PE-7	1
	J. Pichtelberger	PE-7	1
	P. Piscopo	PE-42	1
10.	Pratt & Whitney Aircraft Government Products Division P.O. Box 2691 West Palm Beach, FL 33402		
	Attn: W.R. Alley		1
	J. Brent		1
	R.E. Davis		1
	J.A. Fligg		1
	B.A. Jones		1
	R.W. Rockenbach		1
	H.D. Stetson		1
11.	Pratt & Whitney Aircraft 400 Main Street East Hartford, CT 06108		
	Attn: T.J. Gillespie	E2H	1
	N.T. Monsarrat	E2H	1
	R.E. Pallatine	E2H	1
	A.W. Stubner	E2H	1
	H.D. Weingold	E2H	1
	W.M. Foley (UTRC)		1
	Library (Comm. Prod. Div.)		1
	Library (UTRC)		1
	D.J. Hopwood	E2H	1

12.	Detroit Diesel Allison Division, GMC		1
	Department 8894, Plant 8		
	P.O. Box 894		
	Indianapolis, IN 46206		
	Attn: R.F. Alverson	U-28	1
	J.L. Bettner	U-28	1
	R.L. Jay	W-16	1
	R.E. Riffel	W-16	1
	P. Tramm	U-27	1
	Library	S-5	1
13.	Northern Research and Engineering		
	39 Olympia Avenue		
	Woburn, MA 01801		
	Attn: K. Ginwala		1
14.	General Electric Company		
	Aircraft Engine Business Group		
	Cincinnati, OH 45215		
	Attn: J.F. Klapproth	K-221	1
	C.C. Koch	H-4	1
	J.W. McBride	O-13	1
	Marlen Miller	K-69	1
	D.E. Parker	H-4	1
	D. Prince	H-4	1
	L.H. Smith	H-4	1
	Technical Information Center	N-32	1
	J.S. Keith	H-4	1
	D.C. Wisler	H-4	1
15.	General Electric Company		
	1000 Western Avenue		
	Lynn, MA 01910		
	Attn: A. Bryans	M.Z. 24048	1
	F.F. Ehrich	M.Z. 24505	1
	L.H. King	M.Z. 240GF	1
	R.E. Neitzel	M.Z. 24502	1
16.	Curtiss-Wright Corporation		
	Wright Aeronautical		
	Wood-Ridge, NJ 07075		
	Attn: R. Cole		1
	S. Lombardo		1
17.	AiResearch Manufacturing Company		
	P.O. Box 5217		
	Phoenix, AZ 85010		
	Attn: J. Dodge		1
	J.R. Erwin		1
	G.L. Perrone		1
	D. Seyler		1
	J. Switzer		1

18. AiResearch Manufacturing Company
2525 West 190th Street
Torrance, CA 90509

Attn: R. Carmody		1
R. Jackson		1
L.W. Pearson		1
Library		1

19. Union Carbide Corporation
Nuclear Division
Oak Ridge Gaseous Diffusion Plant
P.O. Box P, K1401, MS-385
Oak Ridge, TN 37830

Attn: G.B. Boroughs		1

20. AVCO Corporation
Lycoming Division
550 South Main Street
Stratford, CT 06497

Attn: Richard Ainsworth		1
Library		1

21. Teledyne, CAE
1330 Laskey Road
Toledo, OH 43612

Attn: Eli H. Benstein		1
Howard C. Walch		1

22. Solar
2200 Pacific Highway
San Diego, CA 92138

Attn: P.A. Pitt	A-5	1
J. Watkins	C-5	1

23. Goodyear Atomic Corporation
Box 628
Piketon, OH 45661

Attn: C.O. Langebrake		1

24. Hamilton Standard Division of
United Technologies Corporation
Windsor Locks, CT 06096

Attn: Mr. Carl Rohrback, Chief,		
Aerodynamics & Hydrodynamics	M.S. 1A-3-6	1

25. Westinghouse Electric Corporation
Combustion Turbine System Division
P.O. Box 251 (Lab 101)
Concordville, PA 19331

Attn: S.M. DeCorso		1

26. Williams International
P.O. Box 200
Walled Lake, MI 48088
Attn: R.A. Horn, Jr. — 1
R.C. Pampreen — 1
Mail Drop H-10

27. Chrysler Corporation
Research Office
Department 9510
P.O. Box 1118
Detroit, MI 48288
Attn: Chief Engineer — 1

28. Elliott Company
Jeannette, PA 15644
Attn: John W. Schlirf
Vice President of Engineering — 1

29. Caterpillar Tractor Company
Research Dept., Technical Center, Bldg. F
Peoria, IL 61629
Attn: J. Wiggins — 1

30. BMAD
Boeing Aerospace Co.
P.O. Box 3999
Seattle, WA 98124
Attn: W.C. Swan — M.S. 40-51 — 1
A.D. Welliver — M.S. 41-52 — 1

31. Douglas Aircraft Company
3855 Lakewood Blvd.
Long Beach, CA 90801
Attn: Dr. Albert C. Munson-3557 — 1

32. Lockheed Missile and Space Company
P.O. Box 504
Sunnyvale, CA 94088
Attn: Technical Information Center
Dept. 52-50, Bldg. 106 — 1

33. California Institute of Technology
Pasadena, CA 91125
Attn: Professor Duncan Rannie — 205-45 — 1
Dr. Frank Marble — 205-45 — 1

26.	Williams International P.O. Box 200 Walled Lake, MI 48088 Attn: R.A. Horn, Jr. R.C. Pampreen Mail Drop H-10		1 1
27.	Chrysler Corporation Research Office Department 9510 P.O. Box 1118 Detroit, MI 48288 Attn: Chief Engineer		1
28.	Elliott Company Jeannette, PA 15644 Attn: John W. Schlirf Vice President of Engineering		1
29.	Caterpillar Tractor Company Research Dept., Technical Center, Bldg. F Peoria, IL 61629 Attn: J. Wiggins		1
30.	BMAD Boeing Aerospace Co. P.O. Box 3999 Seattle, WA 98124 Attn: W.C. Swan A.D. Welliver	M.S. 40-51 M.S. 41-52	1 1
31.	Douglas Aircraft Company 3855 Lakewood Blvd. Long Beach, CA 90801 Attn: Dr. Albert C. Munson-3557		1
32.	Lockheed Missile and Space Company P.O. Box 504 Sunnyvale, CA 94088 Attn: Technical Information Center Dept. 52-50, Bldg. 106		1
33.	California Institute of Technology Pasadena, CA 91125 Attn: Professor Duncan Rannie Dr. Frank Marble	205-45 205-45	1 1

34. Iowa State University of Science
and Technology
Ames, IA 50010
Attn: Professor G.K. Serovy 1
Dept. of Mechanical Engineering

35. Massachusetts Institute of Technology
Cambridge, MA 02139
Attn: Dr. J.L. Kerrebrock 1
Dr. J. McCune 1
T.H. Okiishi 1

36. University of Notre Dame
Notre Dame, IN 46556
Attn: Engineering Library 1

37. Penn State University
Department of Aerospace Engineering
233 Hammond Building
University Park, PA 16802
Attn: Prof. B. Lakshminarayana 1

38. Texas A & M University
Department of Mechanical Engineering
College Station, TX 77843
Attn: Dr. Meherwan P. Boyce 1

39. University of Tennessee Space Institute
Tullahoma, TN 37388
Attn: Dr. M. Kurosaka 1
Dr. J. Caruthers 1

40. University of Delaware
Newark, DE 19711
Attn: Prof. Barry Seidel 1
Dept. of Mech. & Aero. Engrg.

Is your mailing address, as it appears on this Distribution List, complete and correct? If not, please notify the NASA Project Manager as listed in Item 15 of the Government standard title page.